Technische Universität München
Fakultät für Physik

Master's thesis in Nuclear, Particle and Astrophysics

Determination of the Chiral Anomaly and Studies on the Pion Polarizability in Pion-Nickel Reactions from COMPASS at CERN

Julian Anton Seyfried

Friday 14th July, 2017

Contents

Abstract In 2009 and 2012 the COMPASS experiment at CERN, a fixed target experiment with a two-staged spectrometer, recorded data produced via the Primakoff effect. The data gives access to various types of analysis. $\pi^-\pi^0$ events have been selected to extract the chiral anomaly $F_{3\pi}$. The selected data has been corrected for acceptance and the background from $\pi^-\pi^0\pi^0$ events has been estimated. The cross section of $\pi^-\gamma \to \pi^-\pi^0$ has been obtained in its dependence of $m_{\pi^-\pi^0}$ and the scattering angle, where the normalization has been obtained from the observation of kaon decays into $\pi^-\pi^0$. The obtained invariant mass distribution has been compared to a theoretical model, that allows the extraction of the chiral anomaly. Including very preliminary upper limits for the systematic uncertainty, which is subject of further investigation, the fitted value is $F_{3\pi} = (12.9 \pm 2.8)\,\mathrm{GeV}^{-3}$. The statistical error is shown to be better than $0.1\,\mathrm{GeV}^{-3}$, indicating the measurements's potential once the systematic uncertainty is fully understood.

In addition the extraction of the pion polarizability from data recorded in 2012 has been tackled. The Monte Carlo simulation has been refined and the understanding of the 2012 data has been improved.

Chapter 1

Introduction

The strong interaction is one of the four fundamental interactions in nature that are, in our current understanding, responsible for all physics processes. Quantum Chromodynamics (QCD) is the fundamental theory describing the strong interaction of quarks via gluon exchange. While the theory has proven to be applicable in form of a perturbation series in the high-energy regime, in the low-energy region QCD is not calculable via a perturbative expansion in the strong coupling parameter α_s, which effectively increases towards smaller interaction energy to the point where convergence of the series is not to be expected. But processes of low energies e.g. $\pi\pi$ scattering can be calculated using Chiral Pertubation Theory (χPT), which is the effective field-theory expansion of QCD for low momenta [1].

Part of the physics programme of the COMPASS experiment at CERN is dedicated to study low-energy phenomenum of QCD, such as hadron structure and hadron spectroscopy, with high intensity muon and hadron beams using various types of scattering processes [2]. Three data-taking periods of the COMPASS experiment have been dedicated to the measurement of Primakoff processes, in which a pion (or also muon) scatters off quasi-real photons of a strong electromagnetic field surrounding target nuclei with sufficiently large atomic number as sketched in Fig. 1.1.

The Primakoff process is also relevant for other experiments and is believed to be a possible window to physics beyond the standard model. For example, the CAST experiment at CERN searches for solar axions via the Primakoff effect. The axion is a hypthetical particle that could explain the smallness of CP violation in QCD. Axions are also a possible candidate for dark matter particles. If solar axions exist, they should create real photons via the Primakoff process in a strong magnetic field. These photons can then be measured [3].

At the Jefferson Laboratory the ongoing PrimEx experiment is dedicated to determine the π^0 lifetime via the Primakoff effect using a photon beam [4].
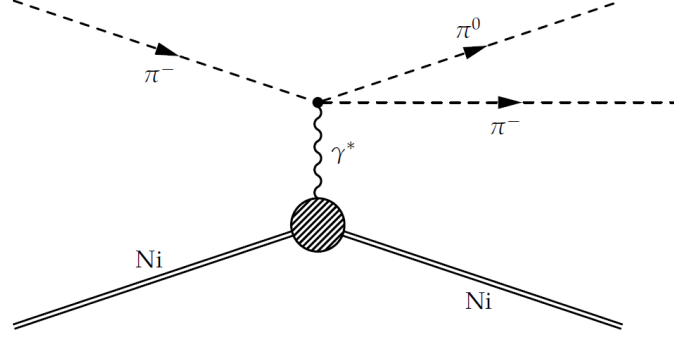
Figure 1.1: Sketch of the Primakoff process $\pi^- \to \pi^- \pi^0$. The virtual photon γ^* is stemming from the electromagnetic field created by the Ni nucleus.

The main goal of the Primakoff measurements at COMPASS is the determination of the charged pion polarizability, the fundamental structure parameters characterizing the behaviour of the pion in an external electromagnetic field [5]. In 2012 the COMPASS collaboration published the most precise measurement of this quantity so far, using data recorded in 2009. The result is in tension with previous experiments but is rather in agreement with the χPT prediction [6, 7].

In 2012 a roughly four times larger data sample was recorded, which is thought to help to increase the precision even further. For this analysis the accuracy of the Monte Carlo simulation plays, a crucial role as the polarizability is extracted by comparing real data to a Monte Carlo simulation of a point-like particle, which can be checked experimentally using the beam of pointlike muons.

Part of this thesis is focused on further improvements of the Monte Carlo simulation for data taken in 2012 to prepare a precise extraction of the pion polarizability.

Using the same data set other processes can be measured with high precision like the chiral anomaly $F_{3\pi}$, accessible in the process sketched in Fig. 1.1. Using χPT $F_{3\pi}$ is calculated to be $(9.78 \pm 0.05)\,\mathrm{GeV}^{-3}$. This value differs from the result obtained by the Serpuhkov experiment, that has been performed in the 1980s [8]. Reanalyzing the data by applying radiation corrections led to $F_{3\pi}$. $F_{3\pi} = (10.7 \pm 1.2)\,\mathrm{GeV}^{-3}$ is now compatible with the χPT prediction [9]. Still this result as well as a result obtained from $\pi^- e^-$ reactions $(F_{3\pi} = (9.6 \pm 1.1)\,\mathrm{GeV}^{-3})$ [10] have a 10% uncertainty. The analysis of the COMPASS data of 2009 and 2012 aims to extract $F_{3\pi}$ with an unprecedented precision. This thesis will provide a first analysis of the 2009 and 2012 data regarding this channel and will provide a first result for $F_{3\pi}$.

This thesis is structured as follows: Chapter 2 focuses on the theoretical concepts.

In chapter 3 the COMPASS experiment is explained. In chapter 4 the analysis chain is explained. Chapter 5 is focused on the pion polarizability. In chapter 6 data selection for the chiral anomaly analysis is explained. The analysis is descibed in chapter 7. Finally chapter 8 gives a summary of the thesis.

Chapter 2

Theoretical bases

2.1 Scattering processes

Scattering processes provide access to the underlying interaction mediating the process. They are a standard tool in particle physics to test theories.

The cross section or quantities derived thereof e.g. asymmetries or ratios, are the interface between theoretical and experimental physics. The total cross section σ is proportional to the probability of a certain process to happen while the differential cross section provides information how the events are distributed in a given variable [11]. Via an experimentally obtained cross section, free parameters of a theory can be determined or via the existence or non-existence of a process theories can be falsified or proved incomplete.

Important Lorentz-invariant quantities of a scattering process, when the recoiling target particle is not observed, are the four-momentum squared modulus $t = Q^2$ of

$$Q = P_{\text{beam}} - \sum_{i=\text{out}} P_i, \tag{2.1}$$

where P_{beam} is the Lorentz vector of the beam and P_i the Lorentz vectors of the outgoing particles, as well as the invariant mass squared

$$s = \left(\sum_{i=\text{out}} P_i \right)^2. \tag{2.2}$$

2.1.1 Gottfried-Jackson-Frame

Angular distributions of physics processes are often studied in the rest frame of
the particle of interest. A possible choice for the reference frame is the so-called
Gottfried-Jackson frame.

In the case of the $\pi^-\pi^0$ final state, the Gottfried-Jackson frame is the rest frame of
$\pi^-\pi^0$ Lorentz vector. The z axis of the Gottfried-Jackson frame is defined by the
direction of the beam. The x and y axis are defined by the momentum transfer
and the direction of target in the $\pi^-\pi^0$ rest frame. A sketch of the Gottfried-
Jackson-Frame is shown in figure 2.1. The angle of a particle with the z-axis is
called Gottfried-Jackson-Angle θ_{GJ} while the angle of the projection of the particle
direction on the $x-y-$plane is called Treiman-Young-Angle ϕ_{TJ}.
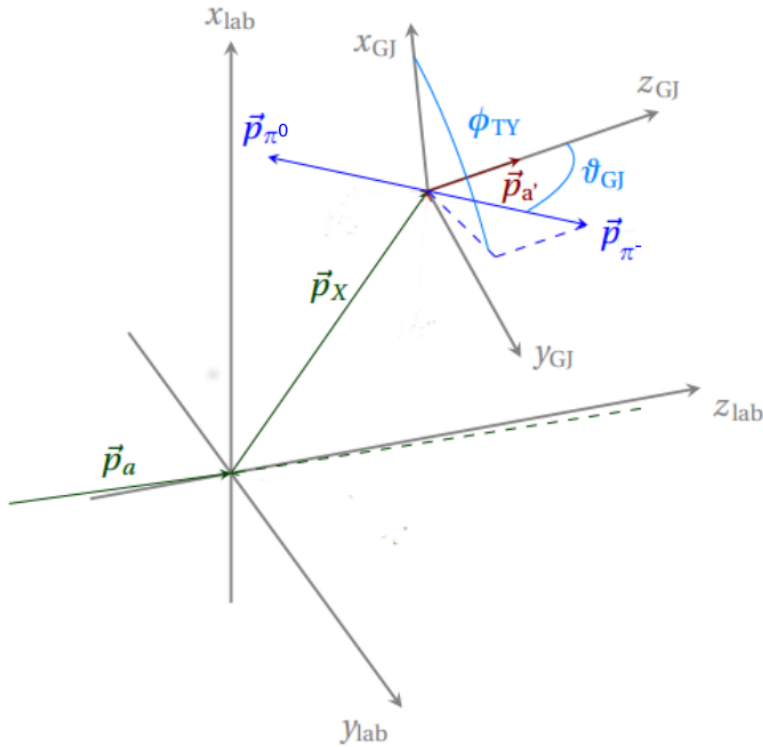

Figure 2.1: Sketch of the Gottfried-Jackson-Frame [12].

θ_{GJ} is directly linked to the energies of the outgoing particles as the particle flying
backwards with respect to the beam direction in the Gottfried-Jackson-Frame has a
lower momentum when boosted to the lab system than the particle flying forward.

If the θ_{GJ} is chosen as shown in figure 2.2(a) an angle close to zero results in an high energetic charged pion while for $\theta_{\mathrm{GJ}} = \pm 90°$ the energy/momentum is distributed equally among the two outgoing particles in the lab system. This behaviour is shown in figure 2.2 (b).
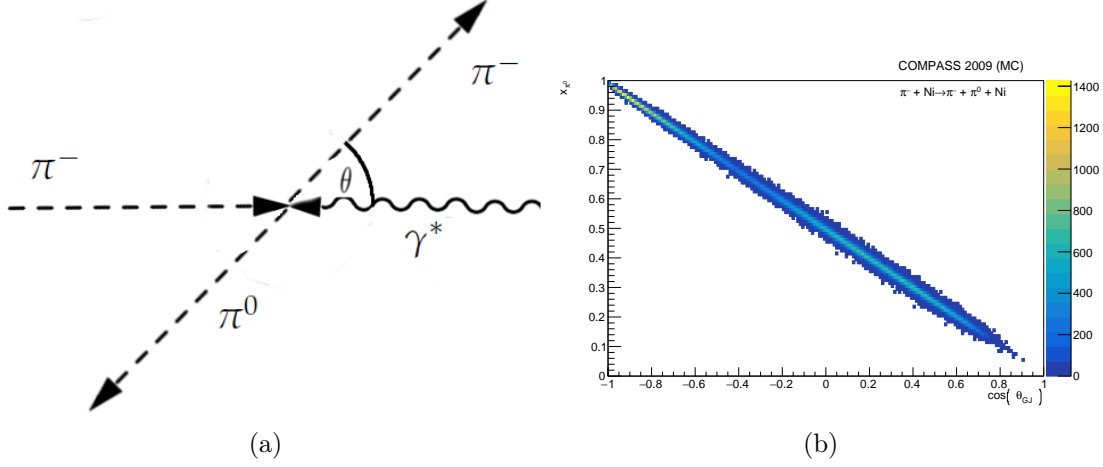

(a)   (b)

Figure 2.2: (a) 2D projection of the Gottfried-Jackson-Frame illustrating the used convention for θ_{GJ} for the Primakoff process with a $\pi^-\pi^0$ final state. (b) Relation between $\cos(\theta_{\mathrm{GJ}})$ and energy fraction carried by the π^0 for $m_{\pi^-\pi^0}$ between $1.5\,\mathrm{GeV}/c^2$ and $1.7\,\mathrm{GeV}/c^2$.

2.2 Primakoff Reaction

The neutral pion production by photon-photon-collision, with the photon stemming from a Coulomb field of a nucleus, has been proposed first by Henry Primakoff to determine the π^0 lifetime by measuring the corresponding cross section. [13]

In the style of this idea, the scattering of ultra-relativistic particles off the photons of a Coulomb field are called Primakoff reactions. An example is shown in figure 1.1.

The cross section for these processes can be factorized in a term describing the pion-photon scattering $\mathrm{d}\sigma_{\pi\gamma \to X}/\mathrm{d}\Phi_n$ of a process creating the final state X and a term describing the density of the quasi-real photons stemming from the Coulomb field. Here Φ_n is the general n-body phasespace. The factorization is called Weizsäcker-Williams approximation or the equivalent-photon approximation (EPA) [14]:

$$\frac{\mathrm{d}\sigma}{\mathrm{d}s\,\mathrm{d}Q^2\,\mathrm{d}\Phi_n} = \frac{Z^2\alpha}{\pi(s - m_\pi^2)}F^2(Q^2)\frac{Q^2 - Q^2_{\min}}{Q^4} \cdot \frac{\mathrm{d}\sigma_{\pi\gamma \to X}}{\mathrm{d}\Phi_n}, \qquad (2.3)$$

where Z denotes the charge of the nucleus and $F^2(Q^2)$ its electromagnetic form factor. The kinematically allowed region starts at $Q^2_{\min}$ as given below, reaches its maximum at $Q^2 = 2 \cdot Q^2_{\min}$ and then strongly drops asymptotically as Q^{-2}. This leads to the so-called Primakoff peak at low momentum transfer which can be used to distinguish the Primakoff reaction from background events as shown in figure 2.3.
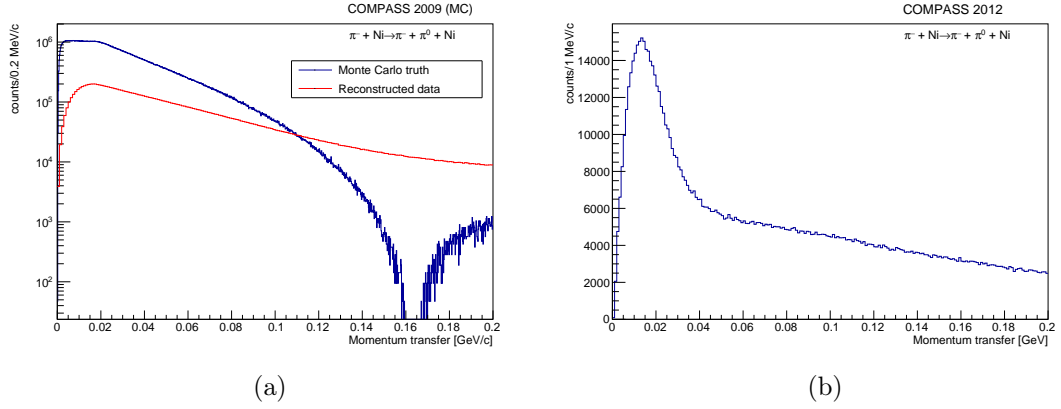

Figure 2.3: Figure (a) shows the Monte Carlo truth distribution of the 4-momentum-transfer as well as the reconstructed one. The 4-momentum-transfer for the Primakoff process peaks at very low values. Due to interaction with matter and the limited resolution of detectors, these small values cannot be resolved and the reconstructed momentum transfer is smeared. The minimum of the blue curve at $0.16\,\mathrm{GeV/c}$ is due to the elastic form factor of a nickel nucleus given in Eq. (2.5). The prominent peak at low momentum transfer in figure (b) is stemming from Primakoff reactions while the spectrum at higher q is dominated by background events as shown in section 7.1

The minimum momentum transfer is given as follows:

$$Q^2_{\min} = \frac{(s - m_\pi^2)^2}{4\,|\boldsymbol{p}^2_{\mathrm{beam}}|}. \tag{2.4}$$

The nucleus may be approximately described in the sharp-radius approximation, thus the form factor is given by

$$F^2(Q^2) = \left(\frac{3}{(qr)^3}(\sin(qr) - qr\cos(qr))\right)^2 \tag{2.5}$$

where r denotes the charge-radius of the nucleus and $q = \sqrt{Q^2}$. It features minima

for $qr = 4.5, 7.7, ...$ The nuclear radius can be approximated using

$$r \approx r_0 A^{\frac{1}{3}}, \tag{2.6}$$

where $r_0 = 1.2\,\text{fm}$ and A denotes the mass number.

Primakoff events can be separated from background by requiring a low 4-momentum transfer as shown in Fig. 2.3 (b).

The energy transfered to the target particle can be estimated for elastic scattering as

$$\Delta E = Q^2/(2M_{\text{Ni}}) < 13\,\text{keV}. \tag{2.7}$$

This is negligible compared to the total energy and the energy resolution. Therefore energy conservation can be formulated:

$$E_{\text{beam}} = \sum_{\text{Particles,out}} E_{\text{p}}. \tag{2.8}$$

2.3 Pion polarizability

The polarizability is a quantity that describes the response of a composite system to the presence of an electromagnetic field and can be separated into the electric and magnetic polarizability α and β linking the induced dipole moments to the respective field strengths [15].

The pion, as a compound system of two valence quarks, sea quarks and gluons, is necessarily polarizable at some scale, as the electrically charged components are not bound infinitely rigid.

The polarizabilities α_π and β_π of the pion are closely linked to the internal structure of pions which is described by QCD. As this quantity is very sensitive to predictions of different theoretical models of QCD, a precise determination is of great interest for testing these models [5].

2.3.1 Theoretical approach

QCD is the theory of strong interaction, the force that mediates the interaction between quarks via gluons.

The theory has been evaluated at high-energy with great success using perturbative expansion in powers of the strong coupling parameter α_s. However in the low-energy regime this approach is not applicable due to the running coupling parameter which is linked to the self-interaction of gluons. This results in the well known effect that no free quarks can be observed, which is called confinement [1].

Thus the polarizability, which is a low-energy phenomena, is currently not calculable directly from QCD.

As single quarks are found only confined into hadrons, it is consequential to create an effective theory in terms of the formed hadron instead of single quarks. Given the vast number of hadrons, this approach may still look not too promising. But restricting the theory to low particle momenta, e.g. $E < M_\rho = 775.26\,\mathrm{MeV/c^2}$ only the octet of lightest mesons (π, η, K) is accessible.

This approach leads to the Chiral Perturbation Theory (χPT) [1].

2.3.1.1 Chiral Perturbation Theory

χPT is the effective low-energy field expansion of QCD. As a series expansion it may converge even at higher momenta, however at the currently available two-loop level it is estimated that only for particle momenta up to $p < M_\rho c$ accurate predictions can be obtained. It allows the calculation of cross sections for the octet of lightest mesons [1].

χPT is based on the chiral symmetry $\mathrm{SU}(3)_L \times \mathrm{SU}(3)_R$ of the QCD langrangian which is neglecting the mass of the three lightest quarks. Because of the non-zero value of the quark condensate, the chiral symmetry is spontanously broken [1].

According to the Goldstone theory this leads to the appearance of eight massless Goldstone Bosons which can be identified as the octet of the lightest mesons. These are the fundamental particles of this theory and therefore their properties are of great interest.

Instead of the coupling parameter α_s the expansion can now be performed in orders of mass and momenta of the Goldstone bosons. Thus the polarizability of the pions can be calculated in χPT:

$$\alpha_\pi + \beta_\pi = \frac{\alpha_e}{16\pi^2 F_\pi^2 M_\pi}\left(c_{1\pm} + d_{1\pm} \cdot \frac{M_\pi^2}{16\pi^2 F_\pi^2} + O(M_\pi^4)\right), \tag{2.9}$$

where, in the chosen convetion for the polarizability, $F_\pi = (130.41 \pm 0.03)\mathrm{MeV}$ [16] is the pion decay constant [7].

The constants $c_{1\pm}$ and $d_{1\pm}$ are linked to the fundamental constants of χPT which have to be determined experimentally.

Using results from other experiments, χPT predicts the following:

$$\begin{aligned}
\alpha_\pi - \beta_\pi &= (5.7 \pm 1.0) \times 10^{-4}\,\mathrm{fm^3}, \\
\alpha_\pi + \beta_\pi &= (0.16 \pm 0.10) \times 10^{-4}\,\mathrm{fm^3}.
\end{aligned} \tag{2.10}$$

There are several other theoretical models predicting values for the polarizability up to $\alpha_\pi - \beta_\pi = (13.6 \pm 2.1) \times 10^{-4}\,\mathrm{fm^3}$. All theoretical models predict a value close to zero for $\alpha_\pi + \beta_\pi$.

2.3.2 Experimental situation

The measurement of the polarizability is done via Compton scattering of a photon at a hadron.

This can be performed for a long living or stable hadrons like protons in a straight forward way scattering photons off a proton target. Due to the short lifetime of the pion, the scattering has to be embedded in a more complex process.

2.3.2.1 Technique

The polarizability is determined using the photon-production via the Primakoff process (fig. 2.4).
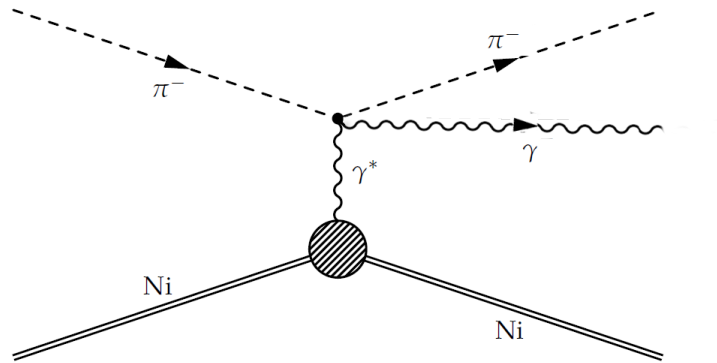

Figure 2.4: Sketch of photon-production via the Primakoff process.

The charged pion polarizability modifies the cross section for this process, as compared to the scattering off a structureless charge, in the following way[17, 18]:

$$\frac{\mathrm{d}\sigma_{\pi\gamma}}{\mathrm{d}\Omega} = \left(\frac{\mathrm{d}\sigma_{\pi\gamma}}{\mathrm{d}\Omega}\right)_{\mathrm{Born}} - \frac{\alpha m_\pi^3(s-m_\pi)^2}{4s(sz_+ + m_\pi^2 z_-)}\left(z_-^2(\alpha_\pi - \beta_\pi) + \frac{s^2}{m_\pi^4}z_+^2(\alpha_\pi + \beta_\pi)\right), \quad (2.11)$$

where $\alpha \approx \frac{1}{137}$ is the electromagnetic fine-structure constant, s the invariant mass of the $\pi\gamma$ final state and $z_\pm = 1 \pm \cos(\theta_{\mathrm{cm}})$ where θ_{cm} is the $\pi\gamma$ scattering angle in the center of mass reference system.

This can be expressed in the terms of fraction of the beam energy carried by the photon

$$x_\gamma = \frac{E_\gamma}{E_{\mathrm{beam}}} \quad (2.12)$$

and factorized as follows:

$$\frac{\mathrm{d}\sigma}{\mathrm{d}E_\gamma} = \left(\frac{\mathrm{d}\sigma}{\mathrm{d}E_\gamma}\right)_{\mathrm{Born}} + \left(\frac{\mathrm{d}\sigma}{\mathrm{d}E_\gamma}\right)_{\mathrm{pol.}} \quad (2.13)$$

The born term is then given by [19]

$$\left(\frac{\mathrm{d}\sigma}{\mathrm{d}E_\gamma}\right)_{\mathrm{born}} = \frac{4Z^2\alpha^3}{m_\pi^2}\frac{E_\pi}{E_\gamma \cdot E_{\mathrm{beam}}}\left[\frac{2}{3}\ln\frac{Q_{\mathrm{max}}^2}{Q_{\mathrm{min}}^2} - \frac{19}{9} + 4\sqrt{\frac{Q_{\mathrm{max}}^2}{Q_{\mathrm{min}}^2}}\right] \quad (2.14)$$

and the polarizability term by

$$\left(\frac{\mathrm{d}\sigma}{\mathrm{d}E_\gamma}\right)_{\mathrm{pol}} = \frac{4Z^2\alpha^3\alpha_\pi E_\gamma}{E_{\mathrm{beam}}^2}\left[\ln\frac{Q_{\mathrm{max}}^2}{Q_{\mathrm{min}}^2} - 3 + 4\sqrt{\frac{Q_{\mathrm{max}}^2}{Q_{\mathrm{min}}^2}}\right], \quad (2.15)$$

where $\alpha_\pi + \beta_\pi = 0$ is assumed. The ratio of the cross sections for a polarizable pion to a non-polarizable pion is given by [19]:

$$R(x_\gamma) = \frac{\left(\frac{\mathrm{d}\sigma}{\mathrm{d}E_\gamma}\right)_{\mathrm{born}} + \left(\frac{\mathrm{d}\sigma}{\mathrm{d}E_\gamma}\right)_{\mathrm{pol}}}{\left(\frac{\mathrm{d}\sigma}{\mathrm{d}E_\gamma}\right)_{\mathrm{born}}} = 1 + \alpha_\pi \cdot \frac{3}{2}\frac{m_\pi^3 x_\gamma}{\alpha(1-x_\gamma)}. \quad (2.16)$$

This function has α_π as its only free parameter. In order to obtain data for a non-polarizable pion a Monte Carlo simulation is used, which corrects at the same time for acceptance and efficiency effects. Finally, the polarizability is given by fitting Eq. (2.16) to the ratio of x_γ obtained by experiment and Monte Carlo simulation.

To verify the simulation, a sample with muon beam has been recorded as part of

the COMPASS measurement. As for muons the polarizability is zero [16], like for every elementary particle, the simulation can be verified using these data.

2.3.2.2 Previous results

The most precise measurement of α_π has been performed at COMPASS with 2009 data, using the same techniques as described and a value of $\alpha_\pi = (2.0 \pm 1.0) \times 10^{-4}\,\text{fm}^3$ has been obtained [6, 20].

Another analysis has been performed using data from e^+e^--collisions of several experiments, which have not been dedicated to this analysis. In addition this analysis is model dependent [21].

Another method tackled by two experiments is the radiative pion photoproduction $\gamma + p \rightarrow \gamma + \pi^+ + n$. The first experiment of this kind obtained $\alpha_\pi = (20 \pm 12) \times 10^{-4}\,\text{fm}^3$ [22]. The most recent high-statistical measurement extracted
$\alpha_\pi - \beta_\pi = (11.6 \pm 1.5_{\text{stat.}} \pm 3.0_{\text{syst.}} \pm 0.5_{\text{mod.}}) \times 10^{-4}\,\text{fm}^3$. This method requires theoretical modelling due to the pion as virtual exchange-particle and the contribution from baryon-resonance. The modelling error is claimed to be underestimated from [23].

The goal of the 2012 measurement is to confirm the 2009 result and extract a more precise result due to more events in both the muon test sample and the pion data set.

2.4 Chiral anomaly

In the naive construction the chiral lagrangian exhibits a symmetry under so-called "intrinsic" parity, implying that it only involves an even number of pion fields. As a consequence only an even number of pions can interact at a vertex. According to this result, the main decay channel of the π^0 into 2γ would be forbidden.

An effective field theory should obey the same symmetries as the underlying fundamental theory [1]. The "naive" chiral lagrangian is invariant under $\phi \leftrightarrow -\phi$ and $x \leftrightarrow -x$ separately while the QCD lagrangian is only invariant under $\phi \leftrightarrow -\phi$ and $x \leftrightarrow -x$ together.

This problem is solved by the Wess-Zumino-Witten (WZW) term, that allows interaction between uneven numbers of pion fields. Processes involving an uneven number of pions are called anomalous [24].

The low-energy dynamics of the process $\pi^-\gamma \to \pi^-\pi^0$ are governed by the WZW term [24]. At leading order of the chiral expansion the amplitude is fully determined by the electric charge e, the pion decay constant F_π and the number of colours N_c [24, 25]

$$F_{3\pi} = \frac{eN_c}{12\pi^2 F_\pi^3} = 9.78(05)\,\mathrm{GeV}^{-3}. \tag{2.17}$$

While the constant for the π^0 decay is in agreement with experiments to a remarkable precision of 1.5% relative uncertainty, the value $F_{3\pi}$ is tested only at a 10% level (compare results given in 2.1).

Method	Result [GeV^{-1}]
$\pi^-\gamma* \to \pi^-\pi^0$[8]	10.7 ± 1.2
$\pi^-e^- \to \pi^-\pi^0 e^-$ [10]	9.6 ± 1.1

Table 2.1: Previous results for $F_{3\pi}$.

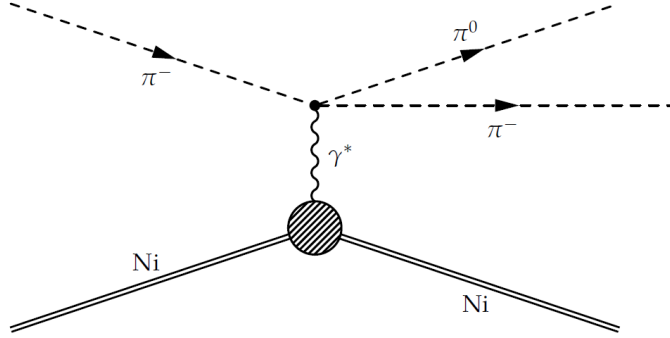The process $\pi^-\gamma \to \pi^-\pi^0$ is accessible via the Primakoff process as shown in Fig. 2.5.

Figure 2.5: Sketch of the process $\pi^- + \text{Ni} \to \pi^- + \pi^0 + \text{Ni}$ via the Primakoff process.

In contrast to the Serpukhov experiment, at COMPASS the cross section can be determined not only for the low-energy regime but also for center-of-mass energies including the $\rho(770)$ resonance and beyond [25]. As the chiral amplitude alone is only valid for regions well below the $\rho(770)$ resonance most of the data would be lost when constraining to the low-mass region. In [25] a dispersive framework is presented, that can be used to extract the chiral anomaly from a fit to data up to an invariant mass of the 2π final state of approximately $1\,\text{GeV}/c^2$ by fitting the cross section behaviour shown in Fig. 2.6 to the experimental data.
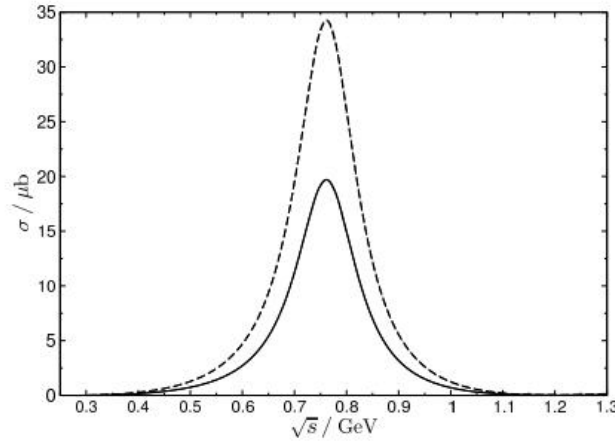
Figure 2.6: Theoretical invariant mass distribution for the $\pi^- \pi^0$ final-state for two different choices of parameters. [25]

Chapter 3

The COMPASS experiment

The **Co**mmon **M**uon **P**roton **A**pparatus for **S**tructure and **S**pectroscopy (COM-PASS) is a fixed target experiment located at CERN with a two-staged spectrometer using particles accelerated by the Super Proton Synchrotron (SPS) and secondary particles. COMPASS is among the longest running experiments at CERN, starting to take data in 2001 [26].

Another dedicated detector development relevant for this measurement are the cryogenically cooled silicon detectors, allowing extremely high spatial resolution for the small scattering angles of interest [27].

It has been a pioneer in adopting new detector types like **G**as **e**lectron **m**ultiplier (GEM) or **Micro**-**M**esh **Gas**eous Structure (MicroMegas) [28, 29]. These detector types are now implemented in other experiments like ATLAS or CAST.

3.1 Beam Line

The beam delivered by the SPS via the MS beam line to the COMPASS experiment consists of secondary hadrons or tertiary muons.

Primary protons with $400\,\mathrm{GeV/c}$ are extracted from the SPS and guided to a beryllium target (T6). The length of the target can be varied up to $500\,\mathrm{mm}$ to adjust the intensity of the final beam. A wealth of secondary particles are created by reactions in the target and can be used for different physics programs. For the 2009 and 2012 runs the muon and the hadron beam are of interest. The energy of the final beam is distributed around $190\,\mathrm{GeV}$ with profiles discussed below and in [26].

The hadron beam consists of approximately 95% π^-, 4.9% K^- and 0.1% $\bar{p}$ at the production target [30].

The proton extraction from the SPS is performed in spills of 9.6 s every 48 s.

The beam line has a length of 1.1 km, allowing the efficient production of tertiary muons via the decay of the secondary pions. The beam line is equipped with beam optics to guide and focus the beam. For the identification of the beam particle two Cherenkov detectors (CEDAR) are installed [26]. A direct measurement of the beam energy around 190 GeV is only provided for the muon beam via the beam momentum station (BMS). For the hadron beam the BMS is removed due to the high interaction probability leading to showers in the beam and a radiative level not allowed for the over-ground experiment. For hadrons the beam energy can be estimated based on the momentum direction and vertex position using a polynomial with 441 free parameters describing a neuronal network parametrization trained with exclusive $\pi^-\pi^+\pi^-$ events [31].

The energy and momentum direction for the muon beam is wider spread than the hadron beam as illustrated in Fig. 3.1.

(a) hadron beam   (b) muon beam
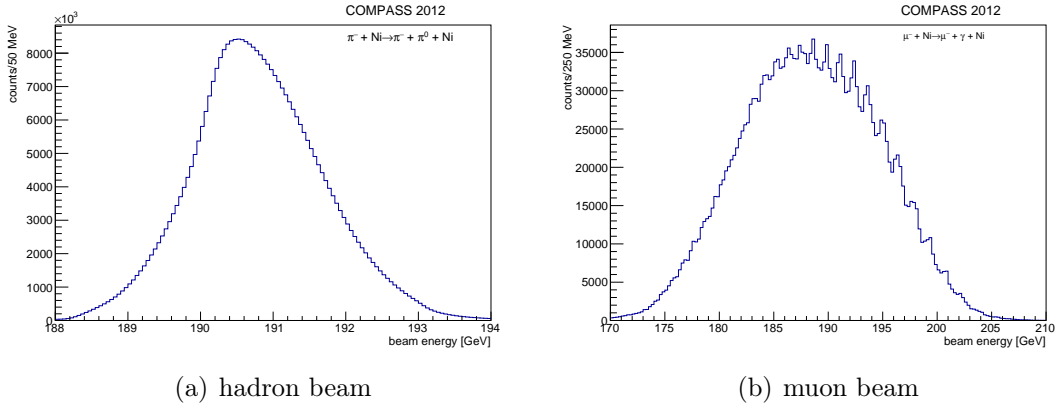
Figure 3.1: Distribution of the beam energy for (a) the hadron beam determined by the neuronal network and (b) for the muon beam determined by the BMS.

3.2 Layout of the COMPASS spectrometer

The COMPASS spectrometer is two-staged allowing the precise measurement of the particle properties over a wide momentum and angular range. Each of the two stages, the large angle spectrometer (LAS) and the small angle spectrometer

(SAS), has their own bending magnet, tracking detectors and calorimeters. The detectors of the LAS have open apertures to allow particles with low scattering angles to pass [26, 32].

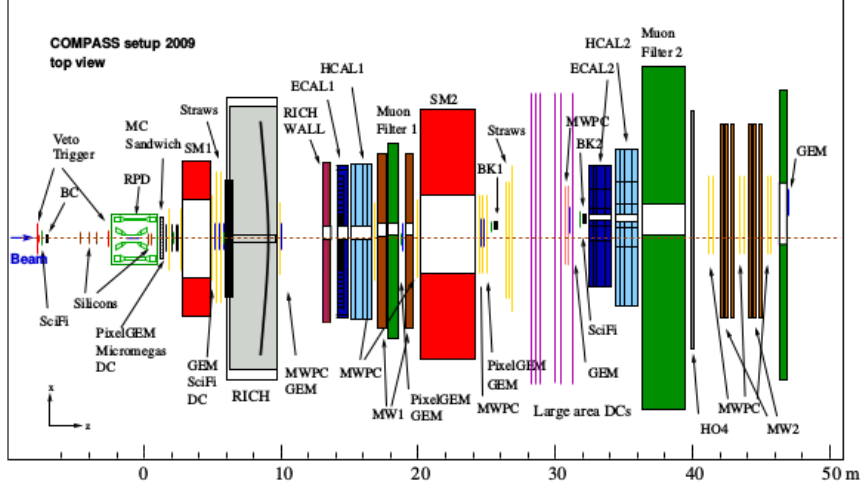A top view of the spectrometer is provided in Fig. 3.2.

Figure 3.2: Top view of the 2009 setup of the COMPASS spectrometer. The LAS is located from 0 m until the HCAL1 at about 15 m followed by the SAS. [32].

3.2.1 Tracking

The tracking system of the COMPASS spectrometer consists of various types of detectors, each especially designed for the position in the spectrometer and therefore suited for the respective particle momenta and rates [26].

Close to the target region five silicon detector units, each consisting of four planes, are installed for a precise determination of the primary vertex and the momentum direction of both the beam and the scattered charged particles. Their location within the target region is shown in Fig. 3.3 [32]. Their cryogenic cooling, implying a thermal stabilization on the ± 1 K level, is a key feature of the achieved resoluation, which is required for the analysis presented below [33].

Other tracking detectors are mostly located around the magnets in order to determine the particle momenta, behind the muon filter, consisting of 3 m concrete, for muon detection and close to the calorimeters to associate tracks to calorimeter clusters.
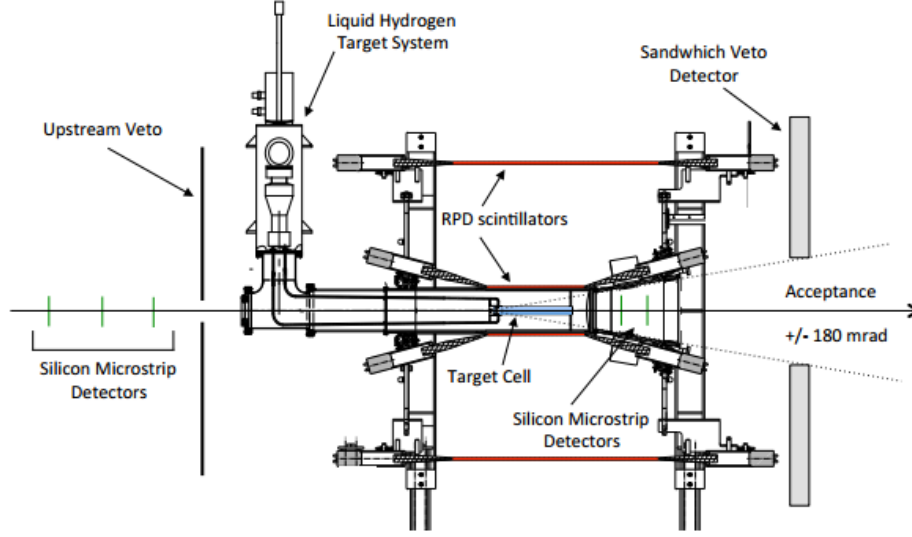
Figure 3.3: Side view of the target region for the liquid hydrogen target. For Primakoff data the liquid hydrogen target has been replaced by a nickel disc and tungsten foils. The silicon detectors for vertex detection are shown in green. [32]

3.2.1.1 Coordinate systems

In COMPASS several coordinate systems are used.

The main reference system (MRS) is defined with the z axis in the nominal beam direction.

Detector hits are stored in the wire-based coordinate system (WRS) $(u, v)^{\mathrm{T}}$. u denotes the coordinate perpendicular to the wires/strips and v parallel to them. Detectors like the silicon detectors or scintillation fibres can measure the u coordinate only while pixel detectors measure the u and v coordinate simultanously. Via the position of the detector in the MRS and angle of the wires in reference to the x axis of the MRS, the position of the hit in the MRS can be calculated.

3.2.2 Calorimeters

For the Primakoff measurements, focused mostly at small scattering angles, the SAS is of great importance. Neutral particles are detected in the second electromagnetic calorimeter (ECAL2). The energy of the charged hadrons is determined

via the bending magnets as it offers a better resolution than the hadronic calorimeter. Events are triggered by the two Primakoff triggers based on the energy deposit in the central ECAL2 region (Fig. 3.4).

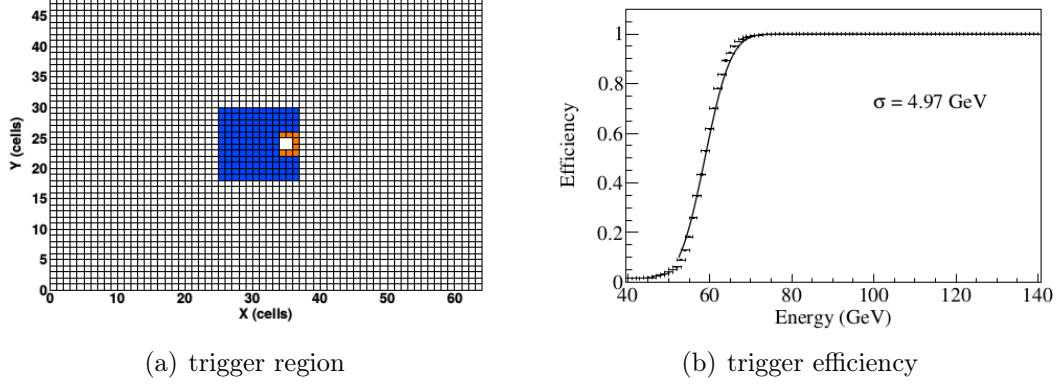(a) trigger region

(b) trigger efficiency

Figure 3.4: In (a) the active region of the Primakoff trigger in ECAL2 is shown in blue. Within the trigger area the hole of four omitted blocks is visible, allowing unscattered beam particles to pass. In (b) the efficiency of the main Primakoff trigger is shown depending on the energy deposit in the region shown in (a).

3.3 Target

Depending on the physics investigated, different targets can be used at COMPASS.

For the Primakoff measurement the target consists of a 4.2 mm thick nickel disc and 34 cm downstream a thin tungsten target were placed as targets. The tungsten disc is divided into two parts, one with a thickness of 25 µm and the other with 50 µm. The tungsten target will be used to determine the π^0 lifetime and to investigate the Z-dependence of the photon-density given in Eq. (2.3).

The support structures consist of stainless steel, the holding rods of carbon. A sketch of the target can be seen in Fig. 3.5
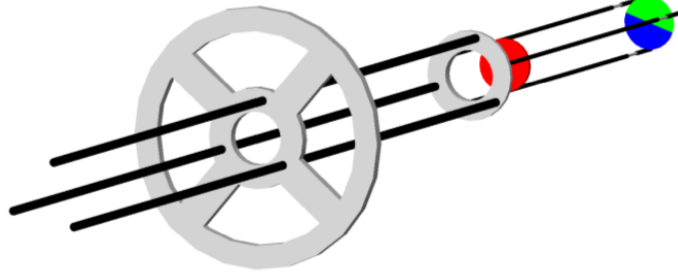
Figure 3.5: A sketch of the target used in 2012 Primakoff run taken from the visualisation software built in TGEANT. The nickel target is depicted in red, the 25 µm tungsten target in blue and the 50 µm tungsten target in green. The stainless steel support structure is shown in grey and the carbon holding-rods in black.

In the distribution of the z position of the primary vertex in Fig. 3.6, the position of the two targets can be seen as well as the silicon detectors SI04 and SI05 downstream the tungsten target.
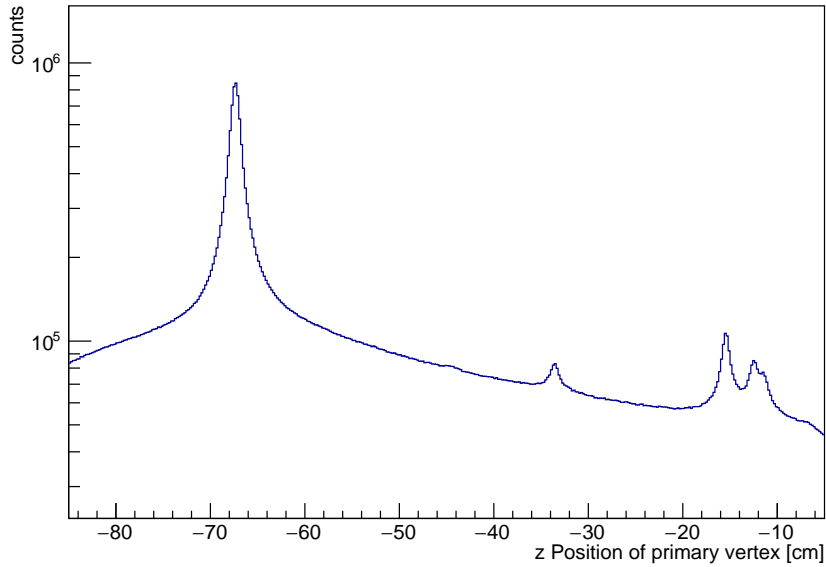
Figure 3.6: z position of the primary vertex. The nickel target can be seen by the reconstructed interactions in the peak at approximately -68 cm. The tungsten target is located at around -34 cm. The two peaks close to $z = -10$ cm originate from the Silicon detectors. The peak at around -16 cm is caused by the vacuum window.

Chapter 4

Analysis chain
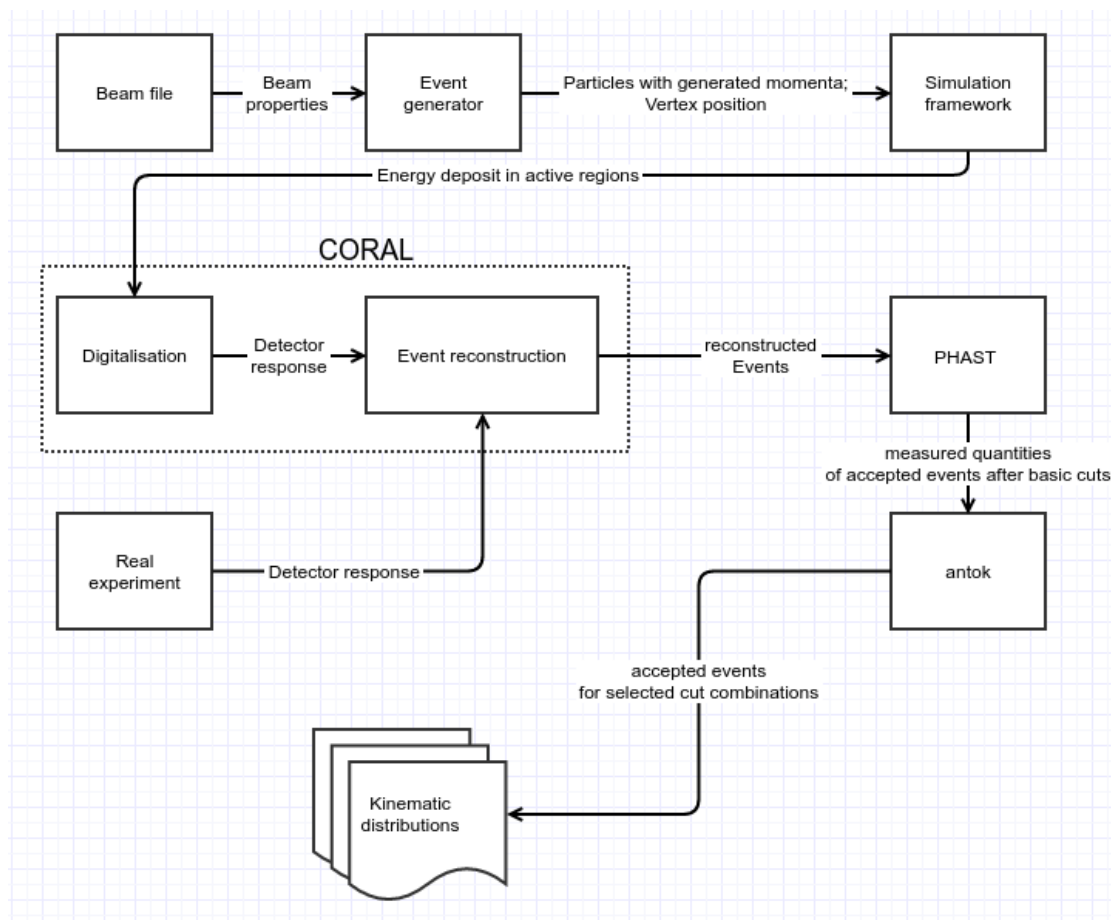
Figure 4.1: Sketch of the analysis chain as used in this thesis.

4.1 Monte Carlo simulation

A complex experiment like COMPASS requires a detailed simulation of the experiment, in order to understand where the apparatus is sensitive and where detector inefficiencies affect the performance. Especially for the measurement of the pion polarizability, which is extracted by the ratio between measured data and simulation, the Monte Carlo simulation plays a crucial role.

As seen in Fig. 4.1 the Monte Carlo chain is implemented such that real data and Monte Carlo data are handled as similar as possible.

The first step of the Monte Carlo simulation is the event generation. The generator creates all particles with their respective momenta and sets the vertex position. The vertex position and the beam properties are taken from a beam file, which contains the beam properties of real events. This ensures a realistic description of the beam and for a hadron beam the neural-network based formula can be used to determine the energy. The hadron beam file is created from exclusive $\pi^- \mathrm{Ni} \to \pi^- \pi^- \pi^+ \mathrm{Ni}$ reactions with a four-momentum transfer $Q^2 < 1.5 \times 10^{-3} \, (\mathrm{GeV}/c)^2$ while for the muon beam file $\mu \mathrm{Ni} \to \mu \gamma \mathrm{Ni}$ events have been used.

The output of the generator is fed into simulation framework, that propagates the particle through the setup, simulating important processes like ionisation and pair production. The output of the simulation is the energy deposit in active detector regions. This information is now fed into the CORAL framework. Based on the energy deposit the response of the detectors is simulated. After the digitalisation process Monte Carlo data is handled like real data.

There are two Monte Carlo simulation frameworks available for COMPASS, namely COMGEANT and TGEANT.

COMGEANT is based on the outdated GEANT3 framework and written in Fortran. Current setups cannot be simulated without further tedious adjustments as some components are not available and no alignment files are provided.

TGEANT is the successor of COMGEANT and based on the modern GEANT4 framework. In contrast to COMGEANT it allows a detailed description of geometries and uses modern technologies like C++ and the ROOT framework.

4.2 Data processing

Using the detector's response the CORAL framework reconstructs tracks of charged particles as well as calorimeter clusters [34]. The information of all events is then stored in mDST (mini Data Storage Table) files. These files can be accessed using PHAST, the physics analysis framework of COMPASS [35]. In this analysis PHAST is used to apply basic cuts for a first-level data skimming to reduce the amount of event by a factor of approximately 100.

The final event selection is done using `antok`, a software created and maintained by members of the E18 chair at TU München. This software allows to define, in an automated way, kinematic distributions for different cut combinations.

The whole analysis chain is sketched in Fig. 4.1.

Chapter 5

Studies on pion polarizability in 2012 Primakoff data

5.1 Summary of 2009 analysis

With the data set obtained in 2009 the most precise determination of the pion's polarizability was achieved by the COMPASS collaboration. The value obtained is $\alpha_\pi = (2.0 \pm 0.6_{\text{stat.}} \pm 0.7_{\text{syst.}}) \times 10^{-4}\,\text{fm}^3$ [20]. Although it is the most precise measurement so far, the error is still about 50%, which, of course, is also due to the small value that was determined [36]. The analysis of the data recorded in 2012 in [36] is the starting point of this thesis.

The goal of the analysis of the data taken in 2012 is to reduce both the statistical and systematic error. This is planned to be achieved by having a factor three more events for the pion data at $x_\gamma > 0.4$ and a larger muon test sample.

In addition the software used for Monte Carlo simulation has been changed from the GEANT3 based COMGEANT to GEANT4 based TGEANT, with the prospect of a more precise description and simulation of the setup.

5.2 Data selection

The data selection for the muon data is described in detail in [36] and is just briefly reviewed in this section.

- **beam properties:** The beam particle has to have hits in the BMS to get the beam energy precisely determined. At cut on the beam momentum direction as well as the position in the beam counter is applied.

- **charged track:** One outgoing track of the primary vertex of a negatively charged particle, that has generated hits in both silicon detector stations SI04 and SI05 in both x-position and y-position measuring planes. Tracks that are calculated such that they cross the yoke of one of the magnets are discarded.

- **Neutral particle:** Exactly one cluster in the ECAL2. Together with the energy of the charged particle, the event has to fulfill relation (2.8) within a given limit. The energy fraction of the photon has to be at least 40% to avoid efficiency effects of the Primakoff trigger.

- **additional cuts:** No other charged tracks in the spectrometer, apart tracks originating from unscattered beam particles ($|\boldsymbol{p}_{\text{track}}| < 170\,\text{GeV/c}$). In addition $Q^2 < 1.5 \times 10^{-3}\,(\text{GeV/c})^2$ is required to select events in the Primakoff region.

5.3 Muon test sample

As described in the introduction, the muon sample is used to estimate the systematic uncertainty that must be attributed to the Monte Carlo simulation. For checking the systematic uncertaintiy the "muon polarizability" can be left formally as a free parameter in a fit function inspired by that for the pion, compare Eq. (2.16). In case the simulation show no systematic effects, the result for α_μ will be consistent with zero wuth an uncertainty that estimates that for the MC simulation for the pions as well.

Comparing the x_γ spectrum of the data to the Monte Carlo simulation yields currently a false polarizablity of $\alpha_\mu^{\text{false}} = 2.5 \times 10^{-4}\,\text{fm}^3$ (compare Fig. 5.1). Thus the systematic error is in the order of the effect that is analyzed and the problem in the data reconstruction or the MC simulation has to be understood, before a value for α_π can be extracted.
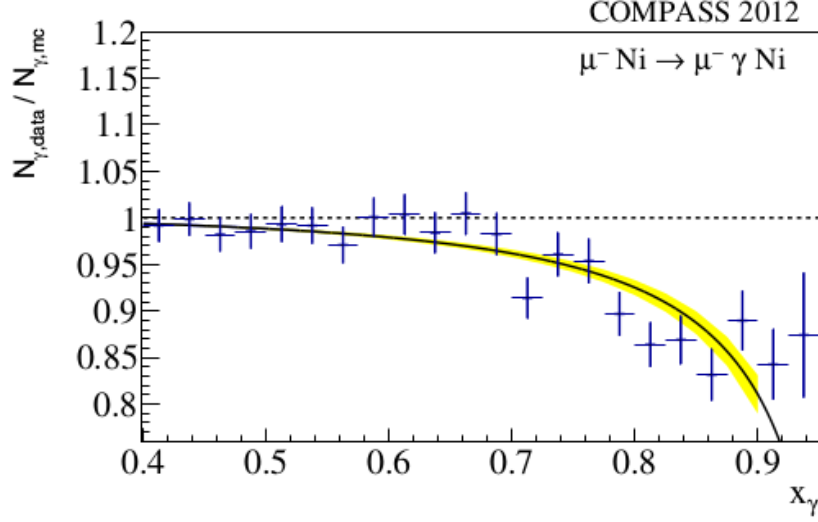
Figure 5.1: x_γ ratio for part of the muon data taken in 2012 with the TGEANT simulation. A false polarizability of $\alpha_\mu^{\text{false}} = 2.5 \times 10^{-4}\,\text{fm}^3$ has been extracted. The yellow band indicates the error [36].

5.4 Monte Carlo studies

To investigate this mismatch, the results of TGEANT are compared to COM-GEANT, by the use which a false polarizability of $\alpha_\mu = (0.5 \pm 0.5) \times 10^{-4}\,\text{fm}^3$ has been extracted for the data record in 2009.

As COMGEANT cannot simulate all components of the 2012 setup and TGEANT has not a built-in 2009 setup, a hybrid setup (COMPASS 2009*) has been created with the components, that both frameworks support. The hybrid setup is mostly consistent with the 2009 setup but does not include the multiplicity counter, the sandwich veto and the RICH pipe. The Monte Carlo studies are performed using pions.

The ratio of the x_γ spectrum between the two simulation frameworks, in the states prior to the investigations described below, is shown in Fig. 5.2. Without any cuts applied both simulations are in good agreement, yielding a relative false polarizability of $(0.6 \pm 0.5) \times 10^{-4}\,\text{fm}^3$. Cutting on the momentum transfer and the $\pi\gamma$ final-state mass results in a value of $(1.2 \pm 0.6) \times 10^{-4}\,\text{fm}^3$.

(a)   (b)
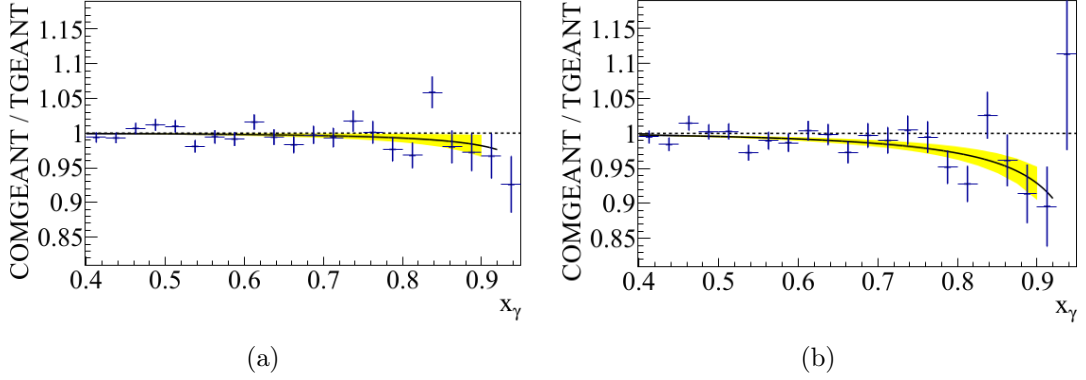
Figure 5.2: x_γ ratio for COMGEANT and TGEANT. In (a) no cuts are applied while in (b) a cut on the momentum transfer and the $\pi\gamma$ final state mass is applied. The yellow band indicates the statistical error.

In Fig. 5.3 the difference of the momentum transfer distribution is clearly visible. The $|Q|$-distribution is more narrow for events simulated with TGEANT and peaks at lower values. Considering that the momentum transfer of the Monte Carlo truth is mostly close to zero, it can be concluded that the experimental resolution of TGEANT events is in average too optimistic.
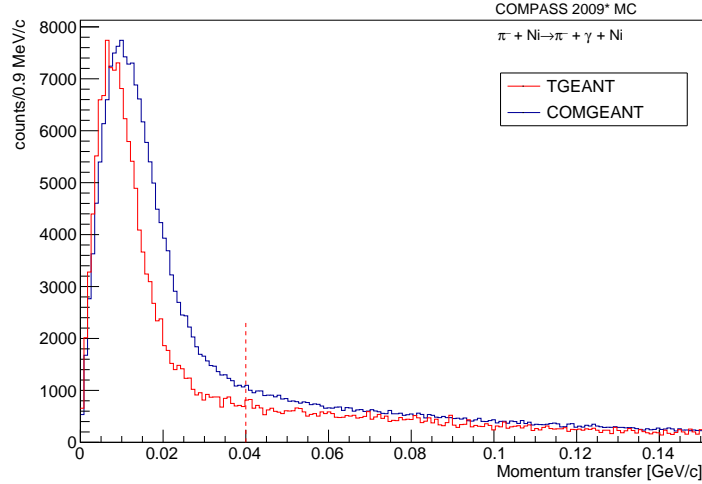
Figure 5.3: Reconstructed momentum transfer $|Q|$ for events simulated with COM-GEANT and TGEANT. The $|Q|$ distribution for TGEANT events peaks at a slighty lower value and is more narrow. The MC truth momentum transfer is mostly quasi-zero. The red dashed line indicates the applied cut on the momentum transfer. The distributions are normalized to the maximum.

To locate the underlying problem, all particles except one have been replaced by the Monte Carlo truth when analyzing the data. Then the distribution of $|Q|$ is compared between COMGEANT and TGEANT events. This way the influence of charged and neutral particles can be studied separately.

The reconstruction of the charged tracks has a big impact on the momentum transfer as it influences not only the determination of momenta of the beam and but also the scattered charged particle. In addition, via the primary vertex determination, also the reconstruction of the photon is influenced, as straight tracks from the primary vertex to center of the clusters in the calorimeter are assumed, having some influence on the photon emission angle.

Replacing all particles with the Monte Carlo truth except the scattered pion and the position of the primary vertex, the momentum transfer as seen in Fig. 5.4 is obtained. The peak of the momentum transfer is still shifted to the left and the width of distribution is smaller compared to COMGEANT. Thus at least part of the effect is stemming from the reconstruction of the scattered pion track.
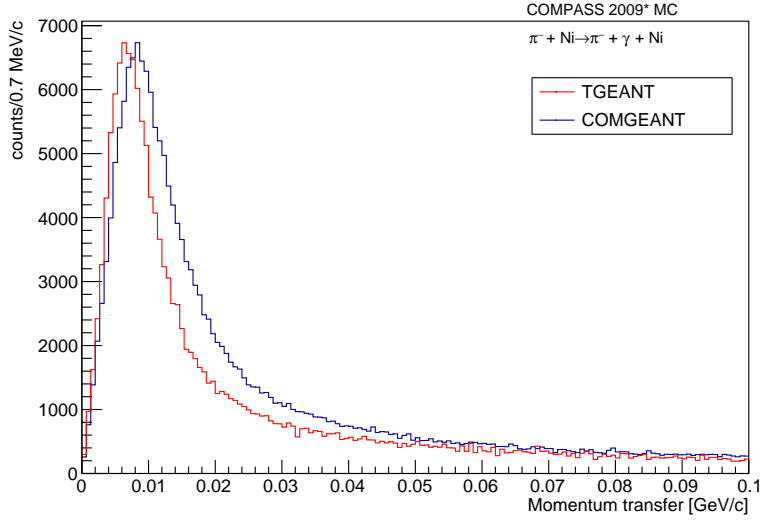
Figure 5.4: Reconstructed momentum transfer $|Q|$ for events simulated with COM-GEANT and TGEANT using the MC truth for both beam and photon. The distribution for TGEANT events peaks at lower values and is more narrow than for COMGEANT events. The distributions are normalized to the maximum.

5.4.1 Studies of charged track reconstruction

When comparing the reconstructed absolute value of momentum of the scattered pion and its momentum direction to the Monte Carlo truth, it can be seen, like in Fig. 5.5, that the reconstructed TGEANT events are on average closer to the generator output. This is in good agreement with the observed effect in the $|Q|$ spectrum.
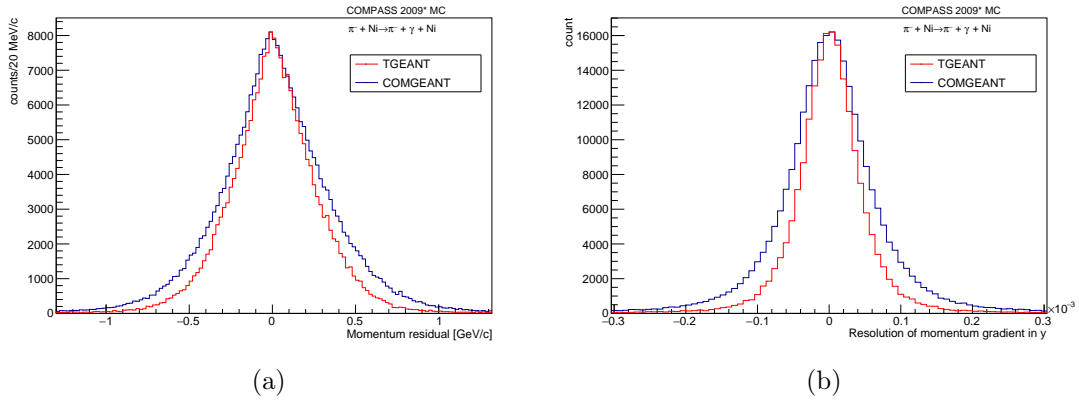
Figure 5.5: The difference between MC truth and reconstructed data is shown for COMGEANT and TGEANT events. In (a) the difference in the momentum is given while (b) shows the difference and the reconstructed momentum direction. The distributions are normalized to the maximum.

In addition the reconstruction of the z position of the primary vertex is more precise for TGEANT events as shown in Fig. 5.6.

This leads to the conclusion that the reconstruction of charged tracks is done with less blurring effects for TGEANT events and results in a more precise reconstruction of the primary vertex. This leads to the observed difference in the $|Q|$ distribution.
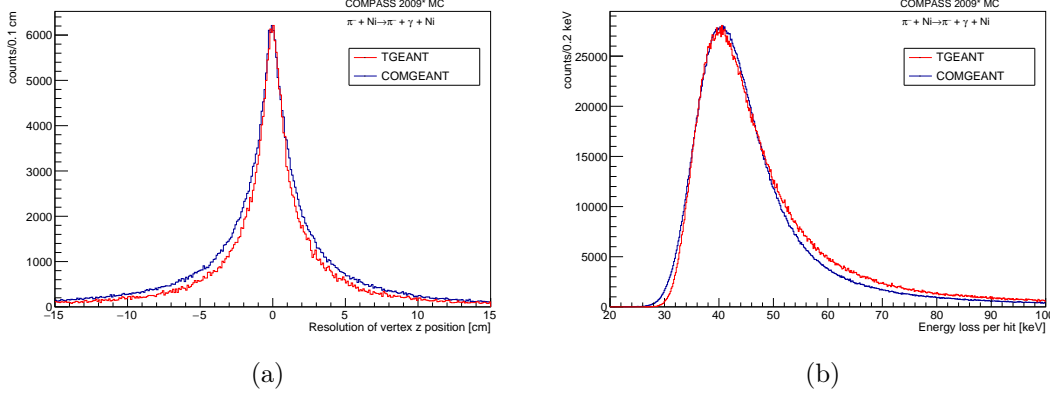
Figure 5.6: (a) Resolution of the vertex z position for COMGEANT and TGEANT events. The distributions are normalized to the maximum. (b) Energy loss per hit for COMGEANT and TGEANT events. The distributions are normalized to the maximum.

As the reconstruction of charged tracks is a complex task, using the data of various detector types, further studies will focus primarily on the silicon detectors as those have the biggest influence on determining the momentum direction and the primary vertex position. In the 2009 hybrid setup there are eight silicon planes downstream of the target.

When comparing the number of MC hits in the silicon planes, a small discrepancy in the number of MC hits in each silicon plane between COMGEANT and TGEANT can be found. With approximately 5% probability TGEANT produces two Monte Carlo hits in a silicon plane. Also the distribution of the energy loss per hit is slightly different as shown in Fig. 5.6 (b). Analyzing events with exactly one Monte Carlo hit in every silicon plane leads to the same difference in the $|Q|$ spectrum as considering all events.

The amount of deposited energy is used within CORAL to determine the number of strips that record a signal from the hit. As seen in Fig. 5.7 (a) the number of hit strips has impact on the spatial resolution as the hit position is determined via center of gravity considerations. The longer tail of the energy loss distribution for TGEANT events could result in an in average higher spatial resolution. However, as shown in Fig. 5.7 (b), this is not the case.
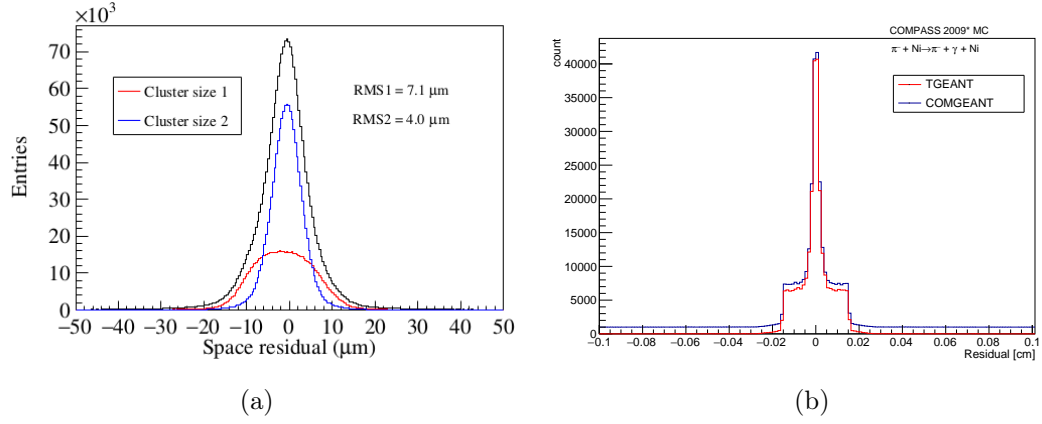
Figure 5.7: (a)Spatial residual of one exemplary silicon plane. The residual for hits spanning one detector strip and hits spanning two detector strips is shown individually as well as the integral which is shown in black [26]. (b)Spatial resolution in the SI05X detector. The difference between MC and reconstructed hit in u (compare section 3.3) is shown. The blue curve is vertically shifted as otherwise the spectrum would perfectly overlap.

5.4.2 Studies of charged particle handling

Assuming no interaction with matter, the charged particle should propagate along a straight line from the primary vertex to the silicon detectors.

To check deviations from this straight line the position of the Monte Carlo hit in the SI05X detector is compared to the position expected for a particle propagating along a straight line. The comparison in Fig. 5.8 shows that in TGEANT the particles' Monte Carlo tracks are closer to a straight line than in COMGEANT.

(a)   (b)
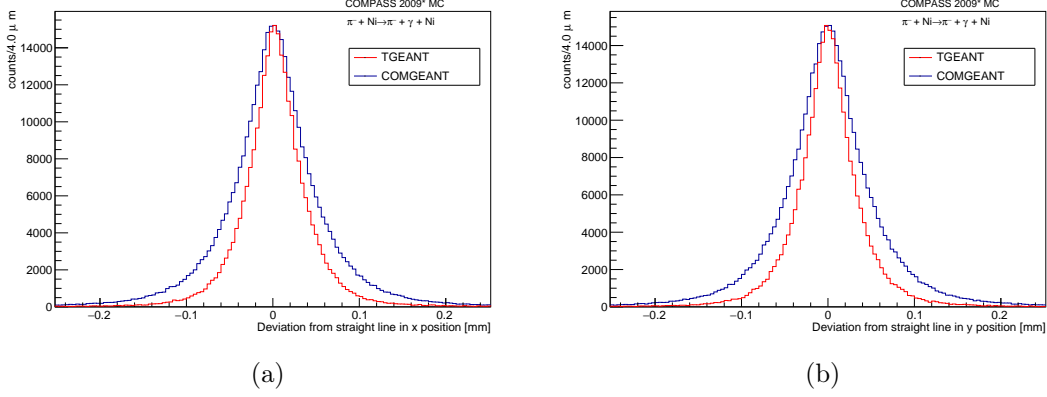
Figure 5.8: (a) x- and (b) y-position of the MC hits compared to the position expected when extrapolting the track as a straight line from the primar vertex for COMGEANT and TGEANT. The distributions are normalized to the maximum.

In addition one has to investigate how the momentum changes from the primary vertex to the silicon detectors.

(a)   (b)
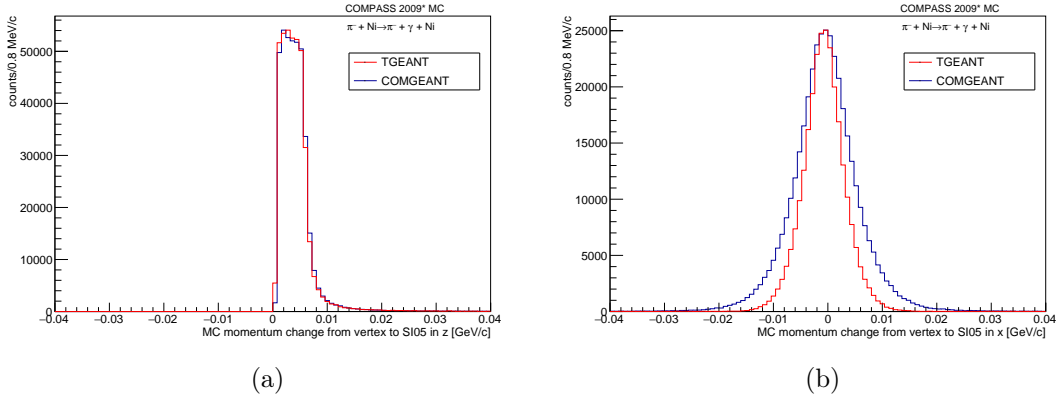
Figure 5.9: Difference between Monte Carlo truth momentum at the primary vertex and the SI05 detector station for (a) z-direction and (b) x-direction. The distribution for the y-direction looks similar to (b).

Thus it is concluded that the interaction with matter is significantly different in COMGEANT and TGEANT prior to the modifications described below.

Multiple scattering in the target is the main cause for deviations from a straight line. Thus the position of the primary vertex along z within the target has influence on this quantity.

5.4.2.1 Position of the primary vertex

In COMGEANT the vertex position is determined by the Primakoff generator. It distributes the z position uniformly within the target.

TGEANT is not using the generator output for the z position, but determines it in the C++ class representing the Primakoff target.

The position of the primary vertex has always been placed in the middle of the target in TGEANT. This has been changed to the same distribution used in COMGEANT, but did not affect the observed difference. This is presumably because placing the vertex for all events in the middle of the target should produce on average the same result as a uniform distribution over the target.

5.4.2.2 Simulation without multiple scattering

In order to understand the influence of multiple scattering, this process has been temporarily deactived. This is a global option in COMGEANT and deactivates multiple scattering for all particles, while in TGEANT the possible physics processes can be adjusted for each particle type separately.

Like in the previous section the studies focues on the track of the scattered pion only and use the MC truth for all other particles. The photon reconstruction in TGEANT does not work without multiple scattering, presumably this is caused by the different shape of showers in the calorimeter. As it can be seen in Fig. 5.10 the momentum transfer $|Q|$ distribution of TGEANT is now in good agreement with COMGEANT. Due to the absence of multiple scattering the reconstructed momentum transfer is now closer to the MC truth. The difference from the MC truth is mainly governed by the spatial resolution of the tracking detectors.
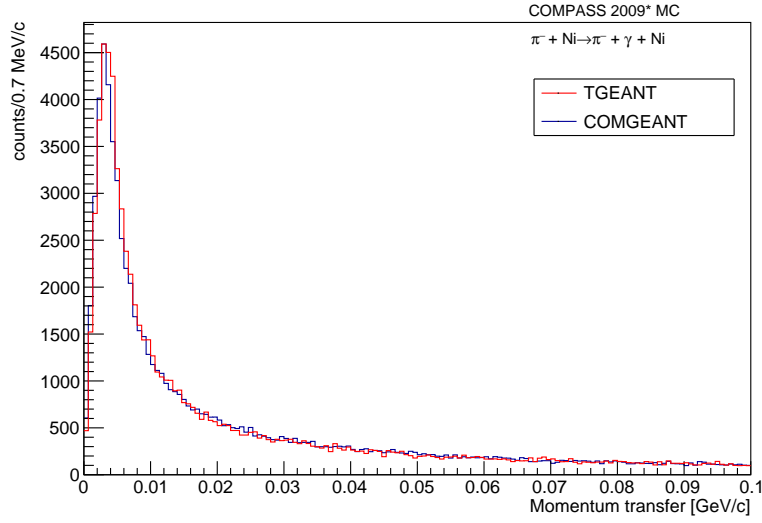
Figure 5.10: Momentum transfer $|Q|$ for COMGEANT and TGEANT events without multiple scattering. Both simulations are now in good agreement. The distributions are normalized to the maximum.

As COMGEANT had proved to be correctly working for the 2009 setup and the $|Q|$ distribution has been to narrow compared to real data, the treatment of multiple scattering is assumed to be implemented wrongly in TGEANT.

5.4.2.3 Multiple scattering

TGEANT offers several models to handle particle interactions with matter, which differ by the computational effort involved and the precision for angular and energy distributions that be achieved.

For multiple scattering processes several of these models exist. These models handle the calculation of momentum and position after each step. If no model is explicitely chosen, GEANT4 is using the Urban multiple scattering model developed by Laszlo Urban [37].

Independent of the model multiple scattering processes are calculated as follows. In the method *alongStepDoIt*, first the true step length t (including assumed zitterbewegung) is calculated based on information like material type, geometrical step length (assuming a straight line) and particle id. If t is above a certain limit, which is in the order of nano meters, the effect of multiple scattering is calculated

by the multiple scattering model. Depending on the model and the settings this affects the particle's momentum as well as the position after the calculated step.

The lateral displacement is returned by the model and the multiple scattering class changes this displacement if needed in way that the particle stays within the volume [38]. In the method *postStepDoIt* the position is changed according to the lateral displacement calculated before and the new momentum direction is set.

The used particles and physics processes to be used and their respective models are activated in the so-called physics list. The physics list is together with the geometry definition and the so-called action initizialization one of the three C++ classes that need to be passed over to GEANT4.

There are several so-called default constructors of the physics list, built for certain fields of application and levels of precisions. The developers of TGEANT have chosen not to use one of these default constructors but define their own physics list. As no further specifications have been made, the Urban multiple scattering model has been used by the beginning of the present work.

Urban scattering model   According to [37, 38] the Urban model has been tested mainly with electron at energies in the lower MeV regime and satisfies the needs of large LHC experiments like ATLAS or CMS. The model is based on Lewis theory [37].

The COMPASS experiment however differs from these experiments as it deals with very small scattering angles and especially for the Primakoff data needs a very accurate simulation of charged tracks.

The Urban scattering model can be further adjusted. By default the sampling of lateral displacement is switched off and the multiple scattering is only caused by changes in the particle's momentum. Switching on the lateral displacement didn't lead to any significant change in the observed differences between COMGEANT and TGEANT.

Wentzel-IV scattering model   Besides the Urban model GEANT4 offers the so-called Wentzel-IV scattering model that is combined with Coulomb single scattering.

After implementing the new scattering model the momentum transfer is again compared in Fig. 5.11. Now the distributions for the momentum transfer $|Q|$ are in good agreement for both simulations.
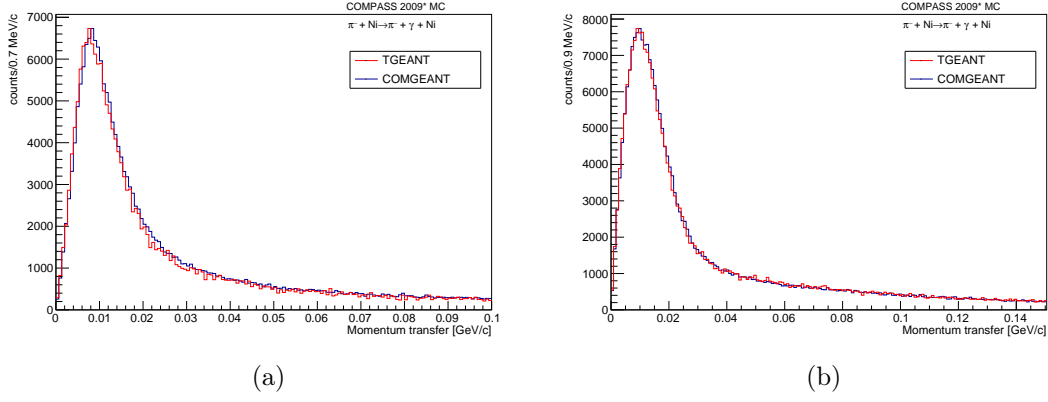
Figure 5.11: Distribution of $|Q|$ using MC truth for beam and photon in (a) and reconstructed data only in (b). Both simulations are now in good agreement. The distributions are normalized to the maximum.

In addition the precision of the z-position of the primary vertex can be compared again to the new multiple scattering model. As it can be seen in Fig. 5.12 the resolution is now equal for both simulations.
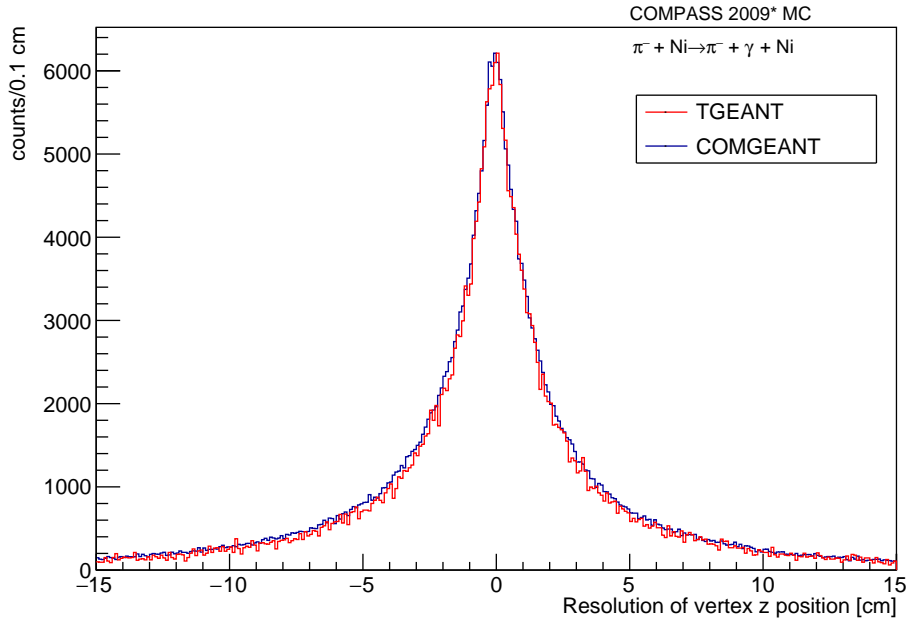

Figure 5.12: Resolution of the z position of the primary vertex for COMGEANT and TGEANT using Wentzel-IV scattering.

The same effect can be observed for the deviation from the straight line. As shown in Fig. 5.13 both simulation frameworks now show the same behaviour.
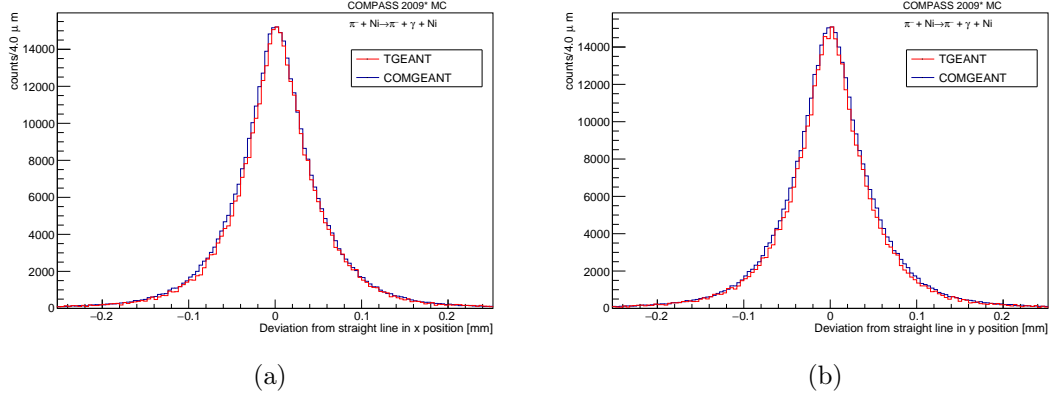
Figure 5.13: (a) *x*- and (b) *y*-position of the MC hits compared to the position expected when extrapolting the track as a straight line from the primar vertex for COMGEANT and TGEANT. The distributions are normalized to the maximum.

Differences Urban/Wentzel-IV scattering In Fig. 5.14 the distribution of the scattering angle per step is shown. The distributions of angles determined by the Urban scattering model peak at lower values but decrease faster than the angles of the Wentzel-IV scattering model. Due to the higher fraction of higher scattering angles in the WentzelIV model, this results in a stronger overall scattering and explains the behaviour shown in the section before.

Due to the good agreement with the COMGEANT simulation, the WentzelIV scattering model combined with Coulomb single scattering has been implemented in the TGEANT physics list.
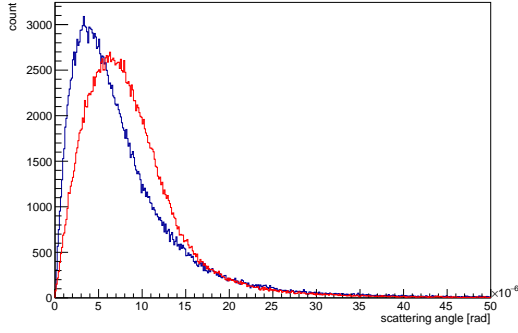
(a) Nickel, 10GeV
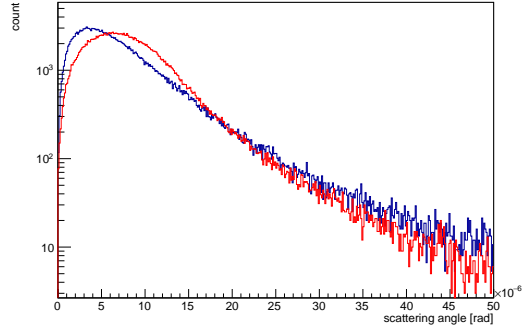
(b) Nickel, 10GeV
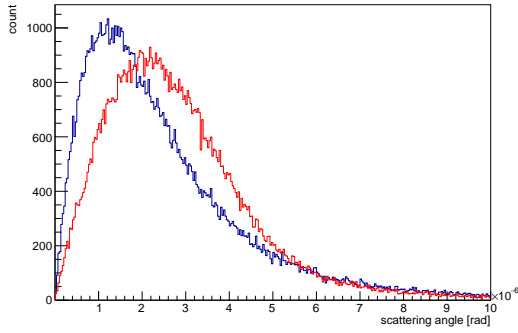
(c) Nickel, 30GeV
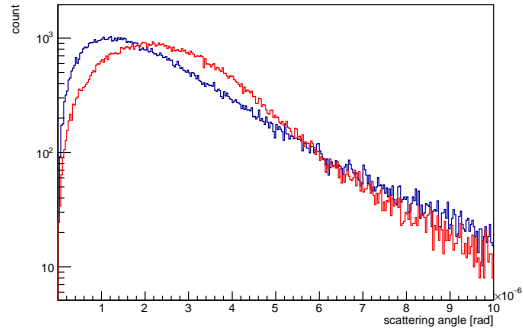
(d) Nickel, 30GeV
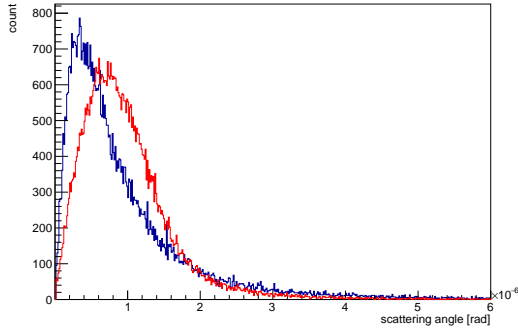
(e) Silicon, 30GeV
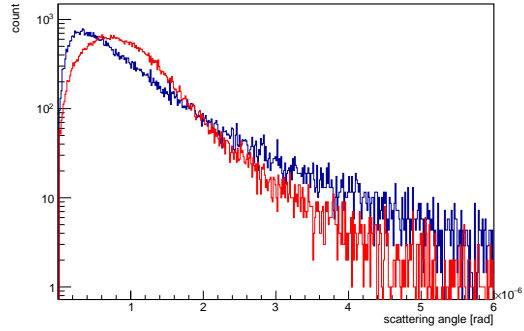
(f) Silicon, 30GeV

Figure 5.14: Scattering angles per step for different materials and pion energies. The blue curves represent the WentzelIV scattering and the red curves the Urban scattering. The histograms are normalized to the same number of entries.

5.4.3 Result

After changing the multiple scattering model and fixing the vertex z position, the x_γ ration of COMGEANT/TGEANT is shown in Fig. 5.15. The shown x_γ ratios results in a quasi-zero relative polarizability parameter. Thus the simulations are now in perfect agreement for the 2009* setup.
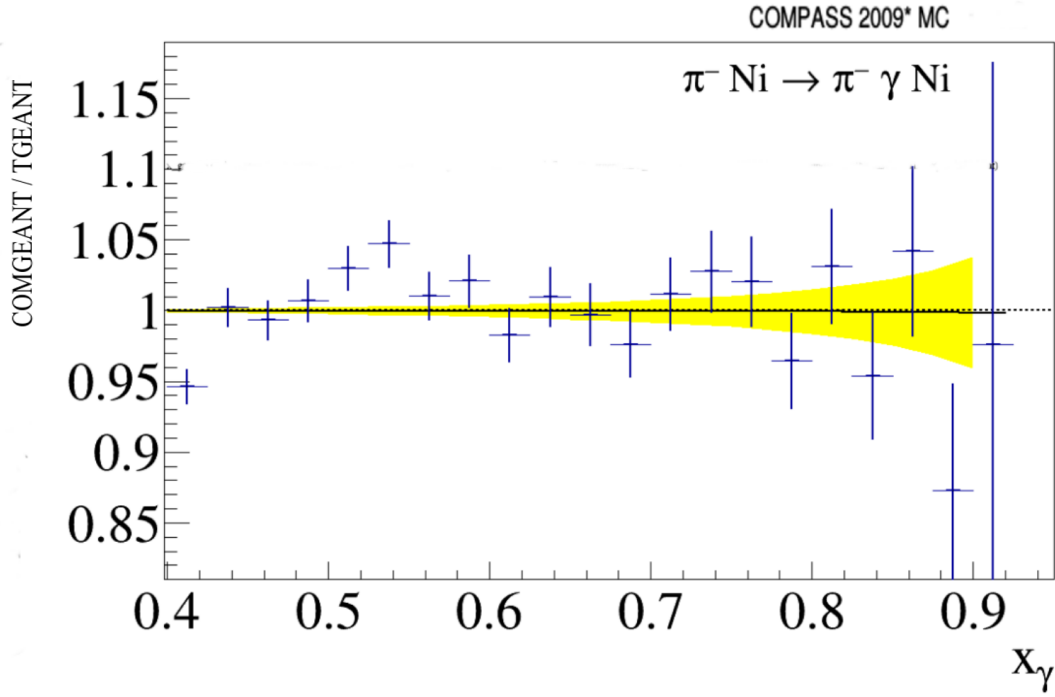
Figure 5.15: x_γ ratio for COMGEANT and TGEANT. Fitting the distribution results in a quasi-zero polarizability. The yellow band indicates the statistical error which is presumably mainly caused by the low event number.

When comparing the simulated data to real 2012 muon data still a large false polariziability is extracted as seen in Fig. 5.16.

Unfortunately the changes made increased the deviation between simulation and real data, but only excluded some reasons.
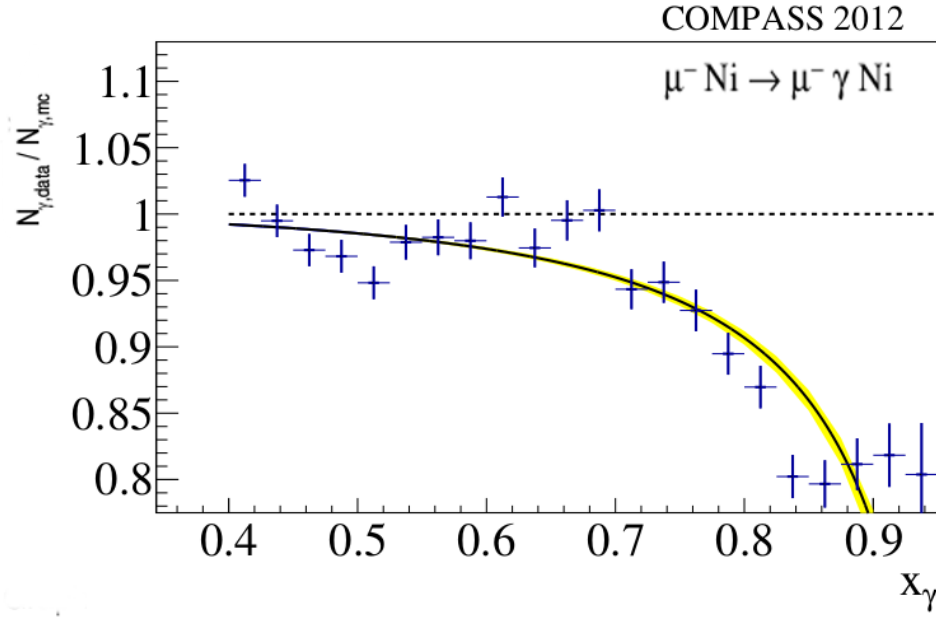
Figure 5.16: x_γ ratio of real data divided by Monte Carlo data. A false muon polarizability of $\alpha_\mu^{\text{false}} = 4 \times 10^{-4}\,\text{fm}^3$

In Fig. 5.17 kinematic distributions of the real data are compared to TGEANT event.

(a) $|Q|$

(b) p_T
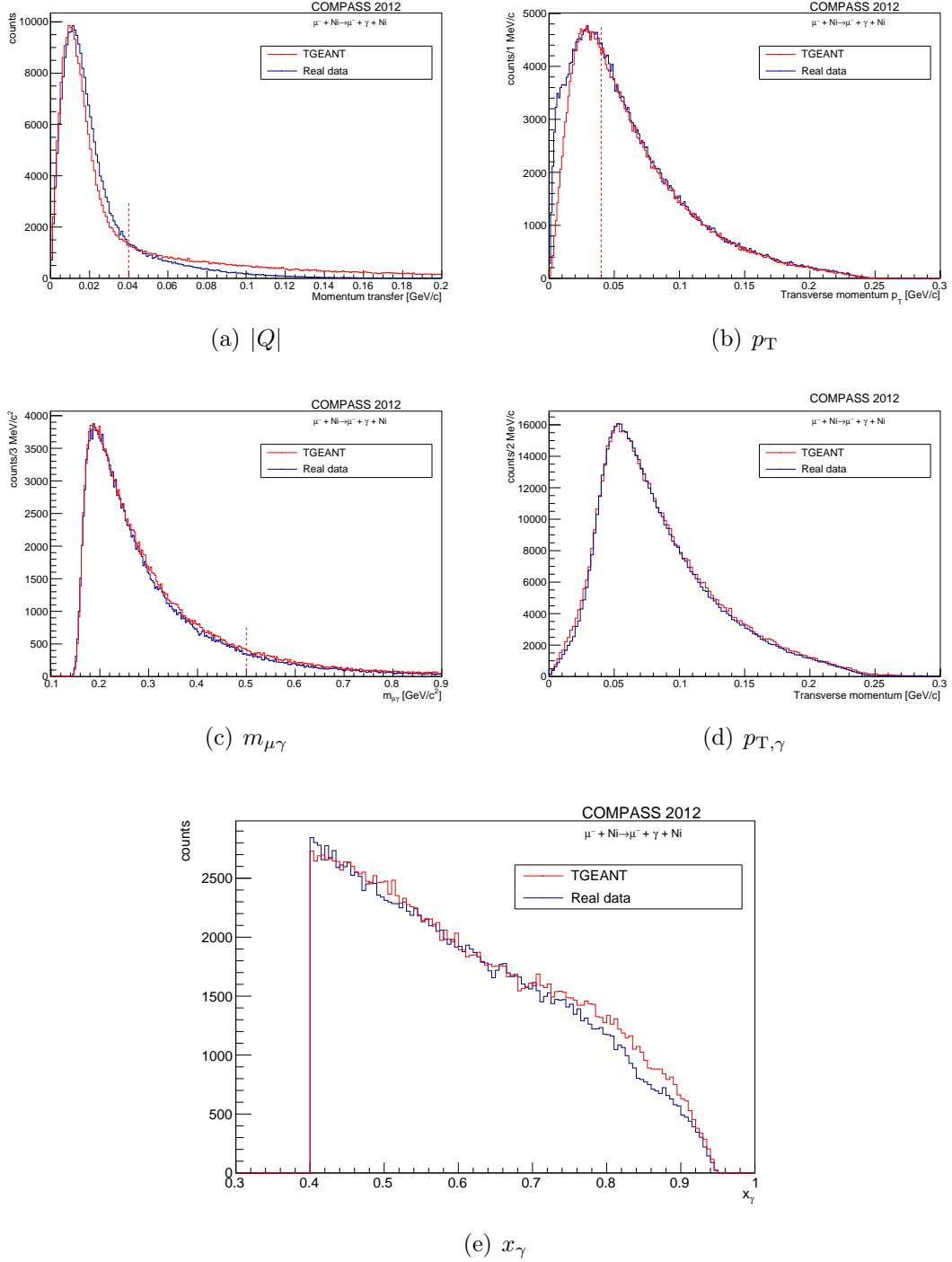
(c) $m_{\mu\gamma}$

(d) $p_{T,\gamma}$

(e) x_γ

Figure 5.17: Comparison of kinematic distributions for real data(blue) and simulation (red) after the presented changes for (a) momentum transfer, (b) transverse momentum of the muon, (c) invariant $\mu\gamma$ mass, (d) transverse momentum of the photon and (e) x_γ without their respective cut (except for x_γ). For p_T the data is in good agreement while for the other distributions deviations can be observed. The distributions are normalized to the maximum.

The spectrum of the momentum transfer shown in Fig. 5.17 (a) is now closer to the simulation in the important regions, still deviations can be seen there. The longer tail for the Monte Carlo data, that can be seen in Fig. 5.17, is due to the fact that the nuclear form factor is not implemented in the generator. This form factor is nearly constant for low values of $|Q|$ but then starts to decrease. In Fig. 5.18 the momentum transfer distribution is shown for two different x_γ ranges. The deviation is slightly depending on x_γ, being smaller for high x_γ, but this cannot explain the difference observed in Fig. 5.16.

(a) $x_\gamma < 0.7$ (b) $x_\gamma > 0.7$
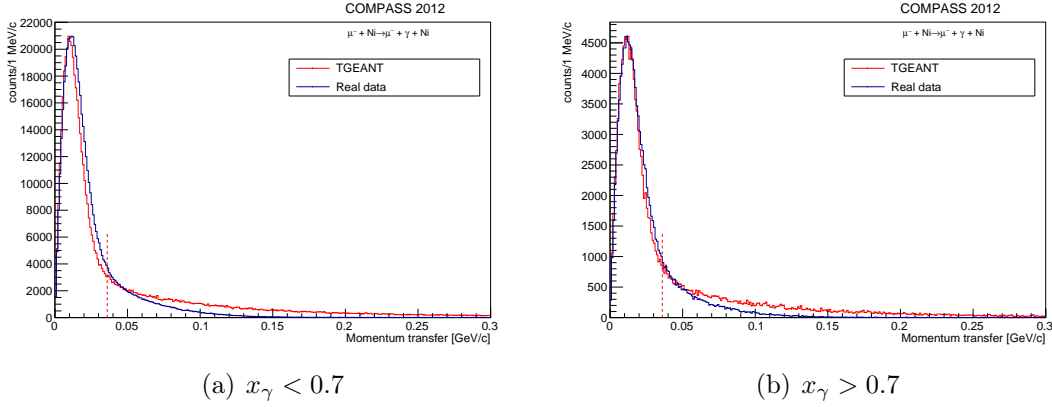
Figure 5.18: Distribution of four-momentum-transfer for high and low x_γ. The distributions are normalized to the maximum.

The spectrum of the transverse momentum of the scattered muon shown in Fig. 5.17 (b) is in good agreement in the important region. The deviation at lower p_T is stemming from pion-electron scattering.

The invariant mass of the $\mu\gamma$ final state shown in Fig. 5.17 (c) differs slightly for values above $0.3\,\mathrm{GeV/c^2}$. This behaviour is investigated for two different x_γ regions in Fig. 5.19. While for lower x_γ the simulation is in very good agreement with the real data, small deviations can be seen at higher x_γ. The deviations could be caused by the photon reconstruction as these distributions differ slightly at higher x_γ (compare Fig. 5.20).
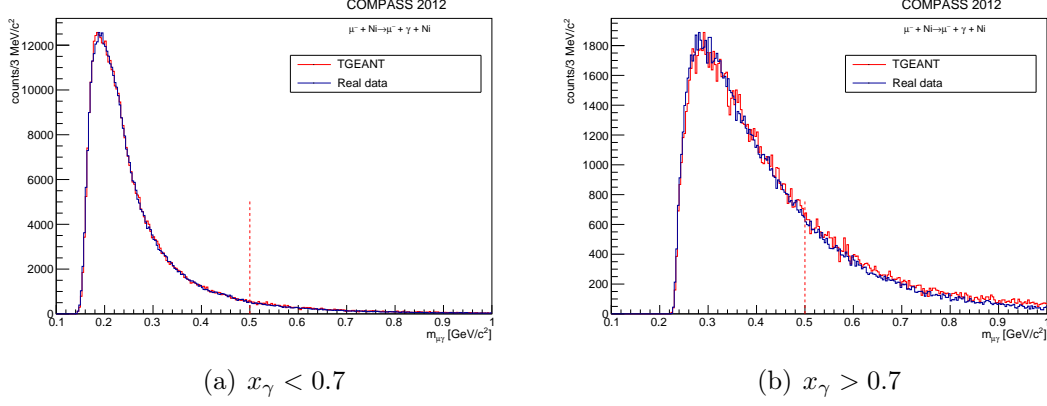
(a) $x_\gamma < 0.7$ (b) $x_\gamma > 0.7$

Figure 5.19: Distribution of $m_{\mu\gamma}$ for high and low x_γ. The distributions are normalized to the maximum.

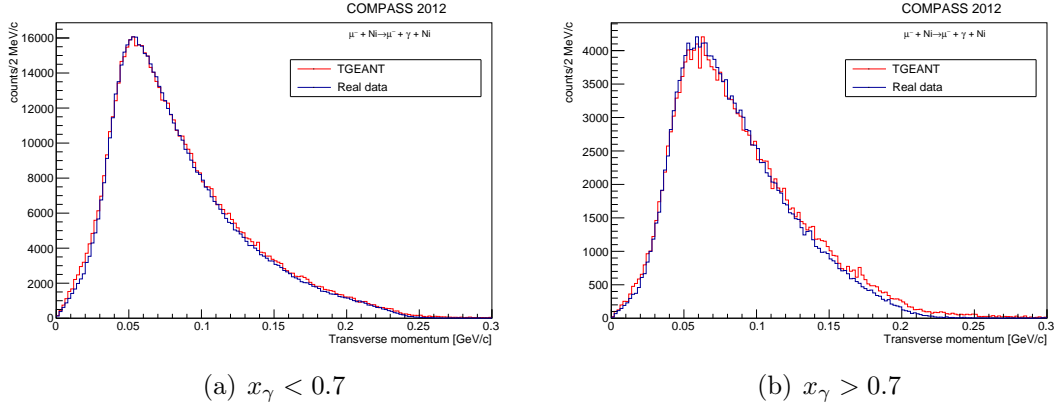(a) $x_\gamma < 0.7$ (b) $x_\gamma > 0.7$

Figure 5.20: Distribution of the transverse momentum of the photon for high and low x_γ. The distributions are normalized to the maximum.

As the observed differences in the kinematic distributions between real data and Monte Carlo simulation do not explain the deviations seen in the x_γ spectrum, acceptance effect have to be considered next. These could be caused by wrong dectector alignment in the Monte Carlo simulation or wrong detector efficiencies. These issues are discussed in the next sections.

5.5 Alignment

Another possible source of deviations from Monte Carlo data to real data is a wrong detector alignment in the simulation. The alignment has been carefully checked and a wrong x position (MRS) has been found for the strawtube detector ST02. The detector has been 8 cm shifted. As the straw tube detectors cover the low energetic regime of the spectrometer, they have a hole to enable high energetic particles to mass without passing through material.

Shifting the detector for 8 cm results in high energetic particles passing additional material while low energetic particles may not be measured.

The miss-alignment happened due to a wrong alignment file for real data. According to this file the ST02 detector has been moved while the GEM detector that is linked to the ST02 detector stayed in place. Therefore it is plausible that is discrepancy has been introduced as a typo. In addition the production of this data taking period should be redone.

5.6 Background tracks

Studying the effect of the single cuts applied reveiled an unexpected behaviour for cuts on background tracks. As seen in Fig. 5.21 the cut on background tracks discards unproportionally many events in the region of x_γ between 0.75 and 0.9. This effect can be observed for all periods except W74 as shown in Fig. 5.21.
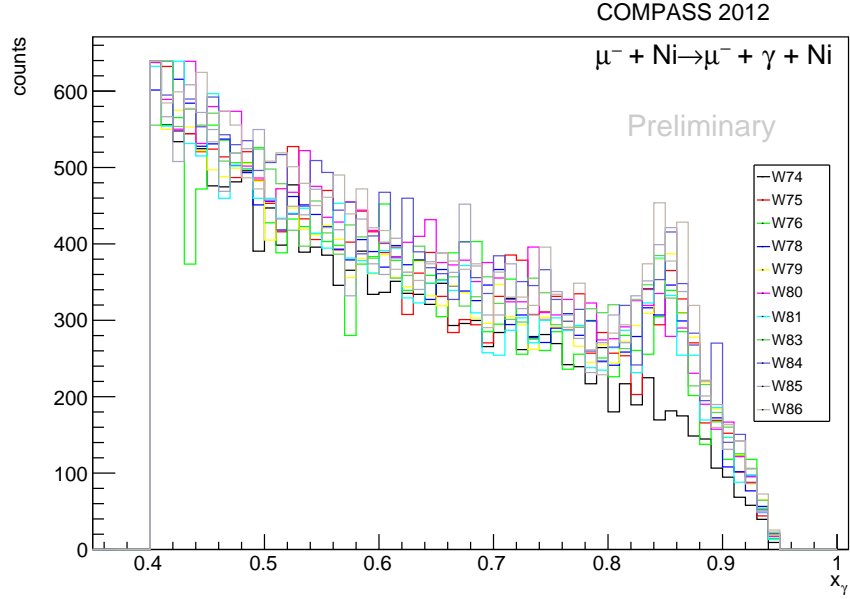
Figure 5.21: x_γ spectrum with inverted cut on background tracks for all data taking periods. A clear excess at high x_γ can be observed for all periods except W74.

This effect is also present in the Monte Carlo simulation however nearly at the same strength.

Studying the background most upstream hit of the track (z_{min}), an excess for low energetic muons (and therefore high x_γ) can be seen at the first detector after the SM2 (compare Fig. 5.22).
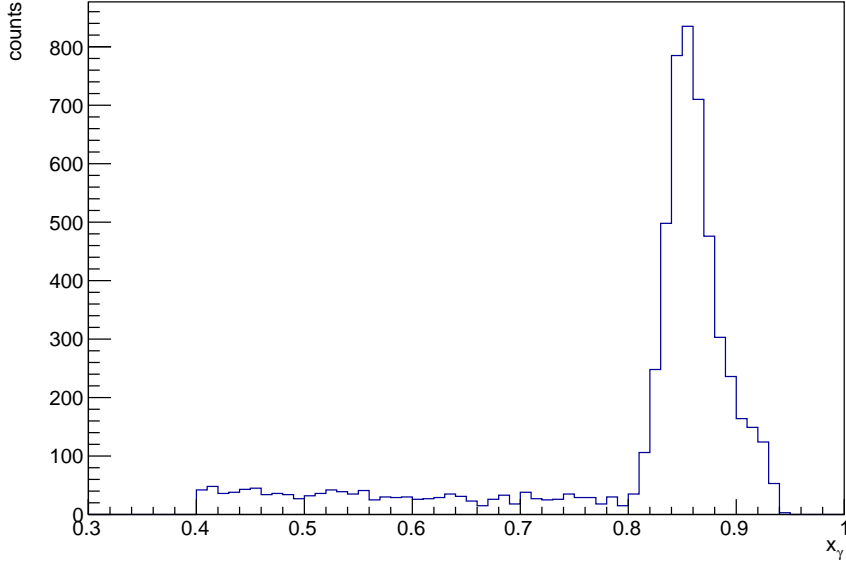
Figure 5.22: x_γ spectrum for events with background tracks beginning at the first detector after SM2 at $z \approx 20.4\,\mathrm{m}$. One has to consider that there are overall fewer events for high x_γ.

This effect has been studied using the Monte Carlo simulation. Most of the background tracks are created before the SM1, although first reconstructed after the SM2, at the multiplicity counter.

This matches the observation, that the effect is not present in the period W74, as the multiplicity counter has been installed afterwards.

In order to get a consistent Monte Carlo description of the whole setup and data taking period, the W74 period has to be skipped.

5.7 Detector efficiencies

As visualized in Fig. 5.16, the x_γ ratio is flat until $x_\gamma \approx 0.7$. Then the ratio starts to decrease rapidly in roughly to steps at $x_\gamma \approx 0.7$ and $x_\gamma \approx 0.8$. x_γ is directly linked to the momentum of the μ^-. For different momentum regimes, different tracking detectors are taking part in the event reconstruction. As seen in Fig. 5.23, the transition are more or less sharp.
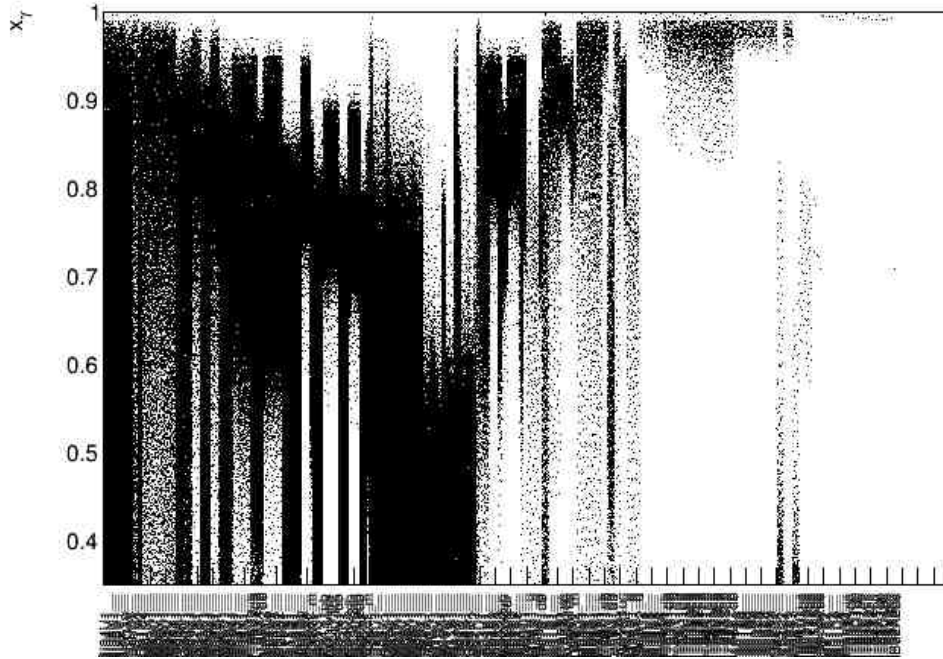
Figure 5.23: Detector hit map over x_γ. The detectors involved depend on x_γ with a sharp transition. The x axis is in principle listed by detector names, which are however too numerous to be readable. They are sorted by z position.

In CORAL the detector efficiencies are adjusted for each detector as a single parameter per default but position dependent efficiency maps can be used. It is crucial that these efficiencies match with the real ones. While for Monte Carlo simulation the efficiency of a detector can be easily determined by the ratio of Monte Carlo hits and reconstructed hits, this does not work for real data.

To treat real data and Monte Carlo data the same way, the efficiencies are determined as follows. Each track that passes through the active area of a detector will increase the number of expected hits for this detector. If the track has no

hit in the detector, the track is extrapolated to the z position of the detector to determine wether the track passed through an active area. The efficiency is then defined by the ratio of actual hits and expected hits. The ratio of these efficiencies, that should be equal to 1 for each detector, is shown in Fig. 5.24. The effect of a similar behaviour has been studied in [39] and was in the order of 50% of the discrepancy observed in the 2012 data.

Further improvements of the simulation should start with determining the correct detector efficiencies. TGEANT allows to introduce position dependent detector efficiencies, which should be prefered to adjusting the global efficiencies. The position dependent pseudo efficiencies have been determined. As an example the position dependent pseudo efficiencies of the MP01MX tracking detector is shown in Fig. 5.25. It is clearly visible that the assumption of a global efficiency does not sufficiently describe the dector response. The rather experimental pixel micromegas (MP) have been first used productively in the 2012 Primakoff run to replace the broken SI04X detector plane.
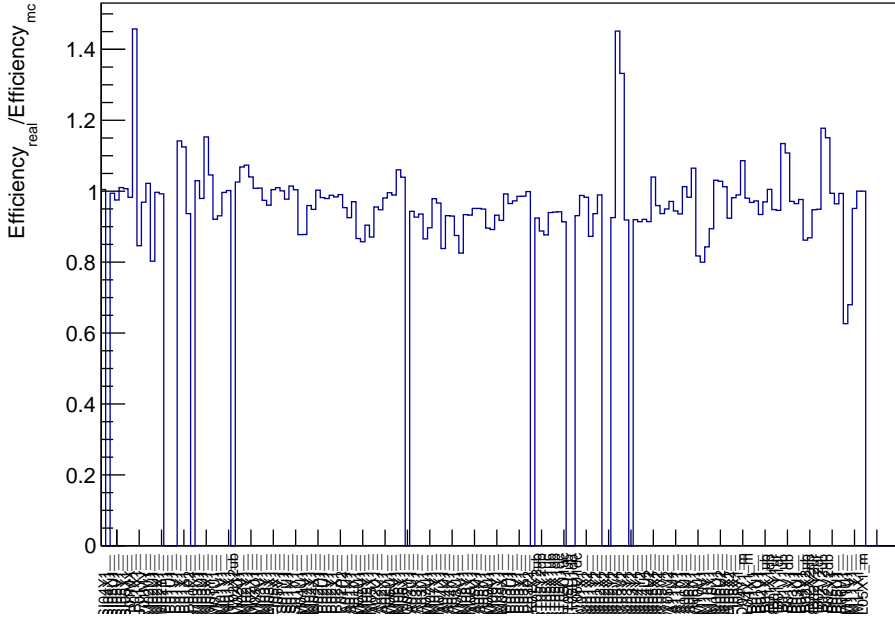
Figure 5.24: Ratio of detector efficiencies for Monte Carlo and real data. In the optimal case, the ratio is equal to 1 for all detectors.
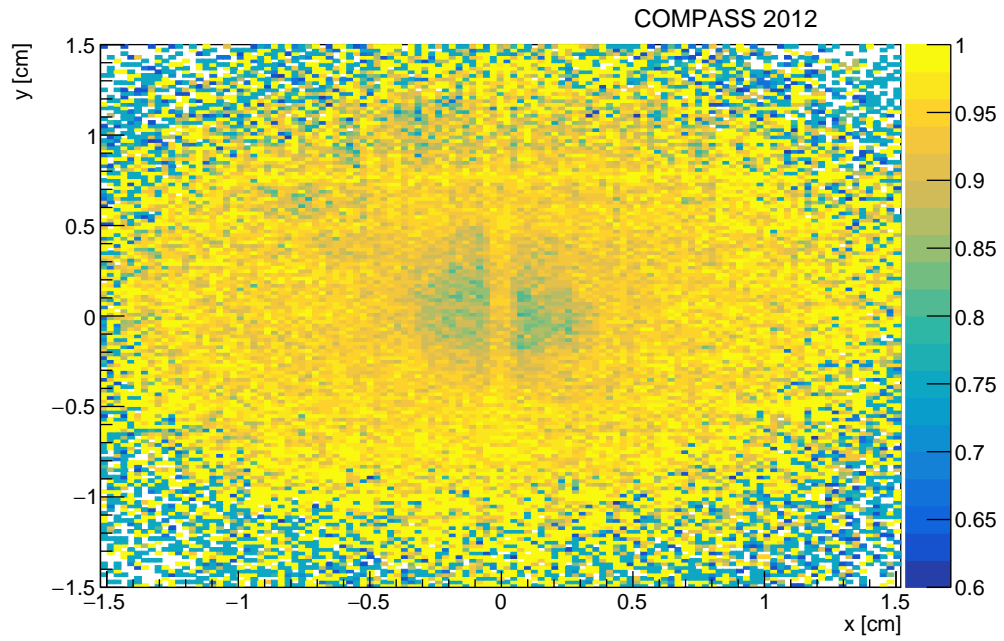
Figure 5.25: Position dependent pseudo efficiencies for the pixel micromega tracking detector MP01MX.

Chapter 6

Kinematic distributions for $\pi^- \mathrm{Ni} \to \pi^- \pi^0 \mathrm{Ni}$

6.1 Event selection

In this chapter the selection of events according to the reaction $\pi^- + \mathrm{Ni} \to \pi^- + \pi^0 + \mathrm{Ni}$ is described. The data have been taken during the 2009 and 2012 COMPASS runs using the Primakoff target, described in detail in section 3.3.

The goal of the event selection is to obtain the $m_{2\pi}$ mass spectrum which will be used to extract the chiral anomaly $F_{3\pi}$.

The data selection is done similarly for 2009 and 2012 data.

6.1.1 Event pre-selection

Basically events involving a charged pion and a neutral pion require a single charged track as well as at minimum two calorimeter clusters. The goal of the pre-selection is to match these basic conditions and reduce the amount of data in a way that they can be stored and analyzed efficiently for several physics processes involving a single charged outgoing particle. The first basic selection, matching these requirements, is performed using PHAST at the CERN computing grid. The number of events is reduced by a factor of approximately 100 compared to the full data set.

The following selection criteria have been applied:

- **Primary vertex:** Events with no vertex or multiple primary vertices have been discarded in order to ensure a single reaction. The primary vertex has to be located roughly in the target region between $z = -200\,\text{cm}$ and $z = 100\,\text{cm}$. This choice allows the analysis of both reactions in the target and also the free kaon decay in the almost material free region around the main target, which is used in chapter 7.4 to determine the beam luminosity.

- **Track properties:** Events with multiple outgoing tracks are discarded, as the only events with a single charged track stemming from a scattered π^- are of interest. The outgoing track has to have passed at least the LAS to have a reconstructed momentum and charge. The momentum has to be below $170\,\text{GeV/c}$ to avoid the admixture from unscattered beam particles.

- **Calorimeter clusters:** As the π^0 decays dominantly into a 2γ final state, at least two calorimeter clusters above $2\,\text{GeV}$ are required. Due to the low momentum transfer mostly small scattering angles are expected. Therefore most photons are expected in ECAL2. Hits in the ECAL1 are ignored.

- **Beam properties:** The beam particle has to be identified as either a kaon or a pion by the CEDAR detectors.

In addition all events recorded in the first period (W24) of 2012 are currently not used due to their different beam profile. This could lead to wrongly determined beam energy by the neural network. The energy distribution differs significantly between W24 and the other periods as shown in Fig. 6.1. After careful checking and parametrization of the neural network for W24 period, the data could be used.
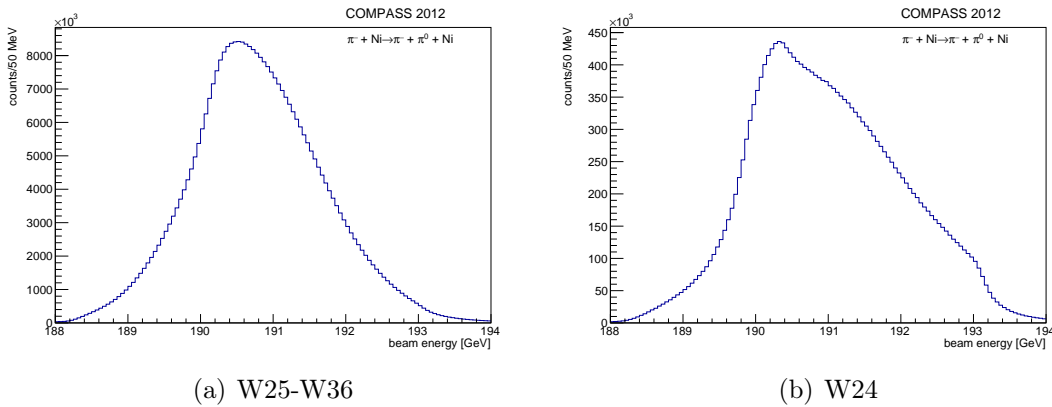

(a) W25-W36 (b) W24

Figure 6.1: (a) Beam energy for all weeks except W24 (b) Beam energy for W24. Due to deviations in the beam divergence in W24 the energy cannot be determined with the neuronal network.

6.1.2 Photon reconstruction

Hits below 2 GeV are ignored as a save cut-off against noise which is normally around 300 MeV.

While the clusterization algorithm supposedly works well for real data, there is a 4.5% chance that clusters in Monte Carlo events are split into two clusters with small distance [36]. This can be compensated by merging clusters with a distance below 5 cm for both real and Monte Carlo data. The new position is the energy-weighted mean of the two single positions [36].

In Fig. 6.2 is shown that clusters are mostly within 8 ns with respect to the beam time. Clusters that are not within an 8 ns window around to the beam time are ignored.

For the data recorded in 2009 a position-dependent energy calibration is performed based on [39]. For data recorded in 2012 this step has been implemented in the mDST production [36].
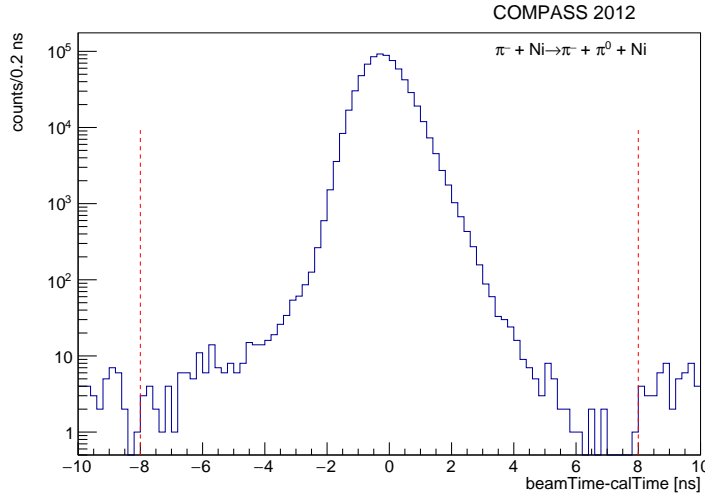
Figure 6.2: Time distribution of calorimeter clusters relative to the beam time in 2012. Only clusters within ± 8 ns (indicated by the dashed red line) are considered as part of the event

The track association of clusters to charged tracks is redone for two reasons.

- The position of the cluster may have changed due to merging clusters.

- The track association algorithm assumes the shower profile of non-hadronic particles. As the pion may produce showers with a different profile in ECAL2, the association algorithm may not work precisely.

All clusters with a distance $R < 3\,\mathrm{cm} + \frac{16\,\mathrm{cm}\,\mathrm{GeV}}{E_{\mathrm{cluster}}}$ close to the track of the scattered pion are discarded[36].

The direction of the Lorentz vectors of the photons are reconstructed by assuming a straight line from the primary vertex to the center of the respective cluster.

6.1.3 Beam divergence

Rejecting events from the beam halo, where momentum and PID are not well known, is done by applying the elliptical cut

$$\frac{\left(\frac{\mathrm{d}X}{\mathrm{d}Z} - \frac{\mathrm{d}X}{\mathrm{d}Z}_{\mathrm{mean}}\right)^2}{a_{\mathrm{x}}^2} + \frac{\left(\frac{\mathrm{d}Y}{\mathrm{d}Z} - \frac{\mathrm{d}Y}{\mathrm{d}Z}_{\mathrm{mean}}\right)^2}{a_{\mathrm{y}}^2} < 1^2, \tag{6.1}$$

with values given in table 6.1.

	2009	2012
$\frac{\mathrm{d}X}{\mathrm{d}Z}_{\mathrm{mean}}$	-3.5×10^{-5}	1.1×10^{-4}
$\frac{\mathrm{d}Y}{\mathrm{d}Z}_{\mathrm{mean}}$	-2.0×10^{-4}	2.6×10^{-5}
a_{x}	2.5×10^{-3}	1.5×10^{-3}
a_{y}	0.3×10^{-3}	0.4×10^{-3}

Table 6.1: Parameters for the elliptical cut on the beam divergence for 2009 and 2012 data.

As shown in Fig. 6.3 the cut discards events from the beam halo mainly.
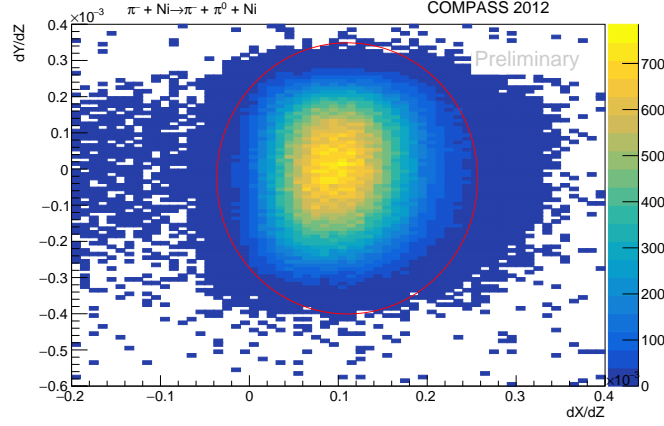
Figure 6.3: Beam divergence for 2012 data without applying the beam divergence cut. The red ellipse indicates beam divergence cut.

6.1.4 Number of clusters

Only two neutral hits stemming from the π^0 decay are expected in the calorimeter. Keeping events with two clusters only, reduces the background from events with more neutral pions or photons involved, e.g. $\pi^- + \mathrm{Ni} \to \pi^- + \pi^0 + \pi^0 + \mathrm{Ni}$ where one π^0 is sufficiently low energetic enough, such that the event appears kinematically complete without it. Events that have not exactly two clusters above $2\,\mathrm{GeV}$ are discarded.

6.1.5 Beam particle identification

A significant contribution to the background of the analyzed process is the decay of negative kaons $K^- \to \pi^- + \pi^0$ due to the same final state and obviously no momentum transfer to a nucleus since the decay is in free space.

A fraction of approximately 2.5% of the beam particles are negative Kaons.

To identify the beam particle, the CEDAR detectors are used.

All events with a beam particle identified by the CEDARs as a Kaon are discarded. As seen in Fig. 6.4 a small fraction of K^- are miss-identified as pions and contribute to the selected events. As the Kaons decay with a probability of around 21% in a charged pion and a neutral pion in the final state and the Kaon

mass is well defined due to the long lifetime, these miss-identified Kaons contribute significantly to the selected events at $m_{\pi^- \pi^0} \approx m_{K^-}$.

The peak of charged kaon mass ($m_{K^-} = 493.677 \,\text{MeV}/\text{c}^2$) can be seen clearly in Fig. 6.4 at $(494.27 \pm 0.01) \,\text{MeV}/\text{c}^2$ for 2012 data. For 2009 data the peak is found at $(494.69 \pm 0.04) \,\text{MeV}/\text{c}^2$. The values have been obtained by fitting the distribution around the kaon mass with a gaussian and a quadratic background. The agreement of these values demonstrates the quality of the energy calibration that is applied.

(a) all cuts   (b) no cut on CEDAR PID
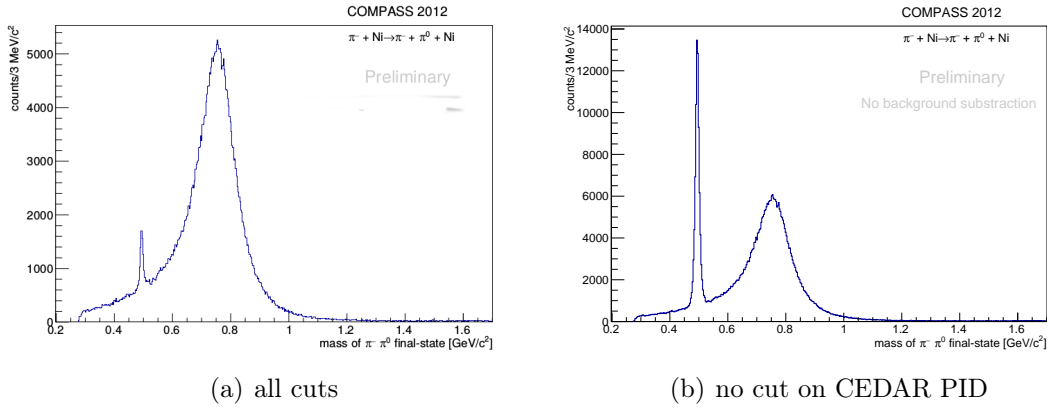
Figure 6.4: Invariant mass of the $\pi^- \pi^0$ final state in the 2012 data with (a) all cuts applied (b) all cuts except CEDAR PID cut applied. The peak at $494.4 \,\text{MeV}/\text{c}^2$ is stemming from the decay of the charged kaon into a charged and a neutral pion.

6.1.6 2γ final state

A photon pair stemming from a π^0 decay is identified by cutting on the invariant mass of the 2γ Lorentz vector.

A possible background is the decay of an η meson ($m_\eta = 547.862 \,\text{MeV}/\text{c}^2$) into two photons.

Fitting the spectrum shown in Fig. 6.5 between $100 \,\text{MeV}/\text{c}^2$ and $160 \,\text{MeV}/\text{c}^2$ with a gaussian and linear background results in an invariant mass of $m_{2\gamma} = (134.77 \pm 0.01) \,\text{MeV}/\text{c}^2$. For 2009 data $m_{2\gamma} = (135.22 \pm 0.02) \,\text{MeV}/\text{c}^2$ is obtained. When considering systematic effects this is consistent with the current world average for the $m_{\pi^0} = (134.9776 \pm 0.0006) \,\text{MeV}/\text{c}^2$ [16].

Fitting the spectrum between $450 \, \mathrm{MeV/c^2}$ and $620 \, \mathrm{MeV/c^2}$ gives a peak at an invariant mass of $m_{2\gamma} = (542.89 \pm 0.01) \, \mathrm{MeV/c^2}$. For 2009 data $(545.57 \pm 0.10) \, \mathrm{MeV/c^2}$ is extracted. This can be identified with the η meson.

To enrich the selection with events involving π^0, only events with photons stemming from a π^0 decay are taken into account a cut is applied on the 2γ invariant mass between $m_{2\gamma} = 120 \, \mathrm{MeV/c^2}$ and $m_{2\gamma} = 150 \, \mathrm{MeV/c^2}$.
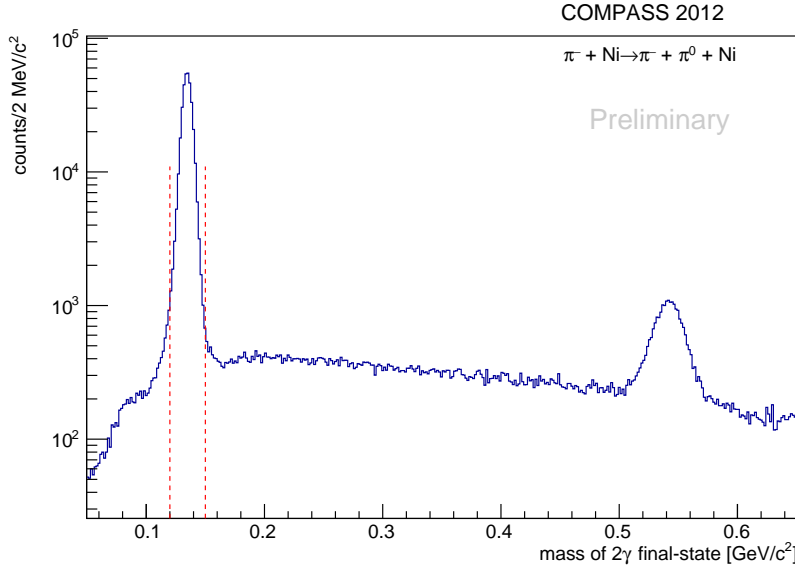
Figure 6.5: Invariant mass of the 2γ final state after all cuts except the cut on the 2γ final state mass have been applied. The peak at $134.8 \, \mathrm{MeV/c^2}$ is stemming from the π^0 decay. The peak at $543 \, \mathrm{MeV/c^2}$ is stemming from the η decay. The dashed red lines indicate the cut applied on the 2γ invariant mass.

6.1.7 z position of primary vertex

The resolution of the z position of the primary vertex depends on the scattering angle of the scattered pion. As the primary vertex is found by the intersection of the extrapolated beam track and scattered pion track, imprecisions in the track reconstruction contribute stronger for smaller angles.

Therefore the cut on the z position of the primary vertex is depending on the scattering angle θ in the lab system and a reasonable θ dependent cut was formulated in [36]:

$$|z - z_{\mathrm{mean}}| < 2.5 \left(0.5 \, \mathrm{cm} + \frac{6.5 \, \mathrm{cm \, mrad}}{\theta} \right), \qquad (6.2)$$

with $z_{\text{mean}} = -67.3\,\text{cm}$. In addition $z < -50\,\text{cm}$ is required to separate events from the nickel target from those in the tungsten foils. For 2009 $z_{\text{mean}} = -73.3\,\text{cm}$ has been used due to the different target position.
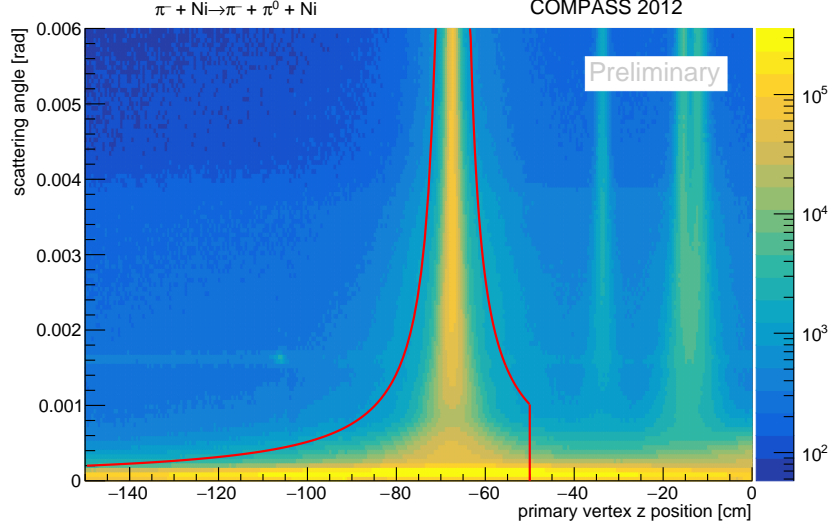
Figure 6.6: Scattering angle θ plotted over the vertex z position. The red line indicates the applied cut. In the distribution the position of the Nickel disc at around $z \approx -73\,\text{cm}$, the tungsten foils at $z \approx -35\,\text{cm}$ and the silicon detectors at $z \approx -18\,\text{cm}$. The band visible at around $1.6\,\text{mrad}$ is stemming from the K^- decay.

6.1.8 Background tracks

In order to enrich the events in the selection, events with background tracks are rejected. A track is considered to be a background track if it fulfills the following criteria:

- Within a time window of $4\,\text{ns}$ with respect to the beam time

- If the momentum has been measured, it has to be below $170\,\text{GeV}$. This prevents beam particles to be tagged as background tracks.

- Begin of the tracks z_{first} has to be in a sensible region therefore below $3.5\,\text{m}$

Background tracks can occur due to pair production of photons, showers created by the charged pion or scattering off electrons.

6.1.9 Transverse position of vertex

To select events stemming from interaction with the nickel disc a circular cut on the xy position is applied. The primary vertex has to be within a circle with radius $1\,\text{cm}$ around $(-0.1\,\text{cm}, 0\,\text{cm})^{\text{T}}$ as shown in Fig. 6.7. This cut also ensures a correct reconstruction of the primary vertex position.
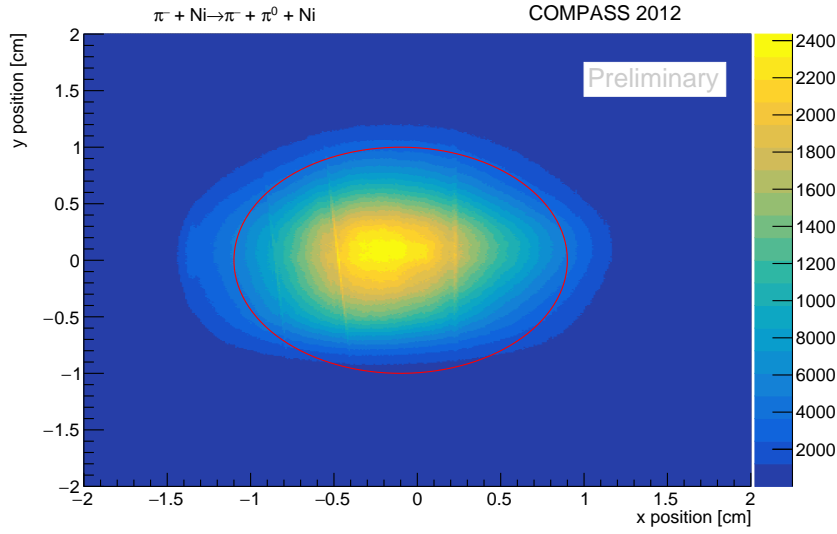
Figure 6.7: xy position of the primary vertex without any cuts applied. The circular shape of the Nickel disc is clearly visible. The cut is indicated as the red line.

6.1.10 Muon rejection

In order to reject events for which the scattered particle is a muon or the pion decays in a muon within the spectrometer two cuts are applied.

- The track of the scattered pion is not measured behind the muon wall in the hodoscope 4 (HO04).

- The track length has passed a calculated material budget equivalent to less than 15 radiation lengths.

6.1.11 Exclusivity

To enricht the selection with events that are exclusive, a cut on the energy balance is applied. As described in section 2.2 the energy transferred to the target is negligible and the energy balance $\Delta E = E_{\text{out}} - E_{\text{beam}}$ should be distributed around zero. As shown in Fig. 6.8 and 6.9 a clear peak is visible, that can be associated with exclusive events. For negative values the radiative tail is visible further a contribution from background events involving additional π^0 that have not been reconstructed is expected.
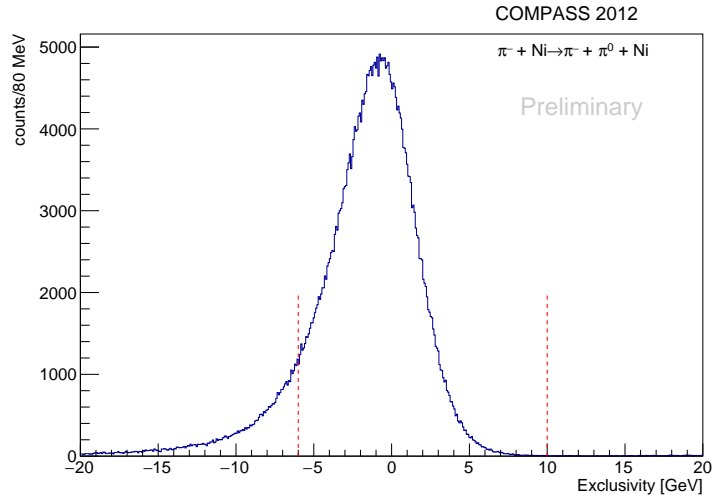
Figure 6.8: Exclusivity $E_{\text{out}} - E_{\text{beam}}$ of 2009 events for all cuts except the exclusivity cut. The cut is indicated by the red dashed lines.
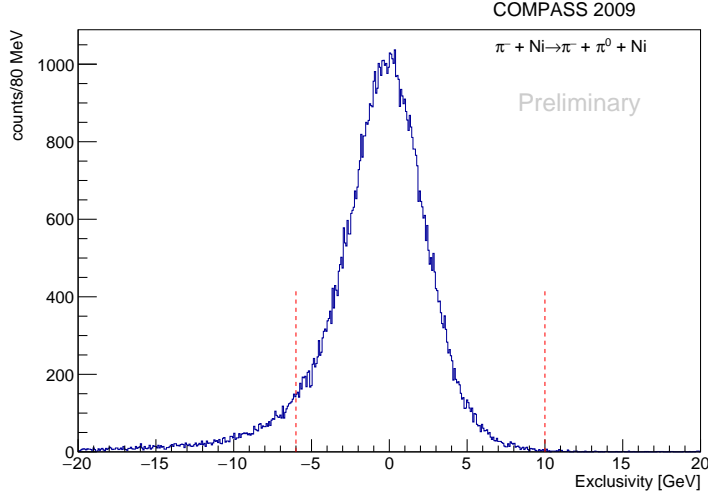
Figure 6.9: Exclusivity $E_{\text{out}} - E_{\text{beam}}$ of 2009 events for all cuts except the exclusivity cut. The cut is indicated by the red dashed lines.

6.1.12 Momentum transfer

The main background to Primakoff production of $\pi^-\pi^0$ are miss-identified $\pi^-\pi^0\pi^0$ events from Primakoff or diffractive production. These events can be found mainly for higher momentum transfer. Requiring a momentum transfer $|Q| < 0.036\,\text{GeV/c}$ minimizes the contribution of background events.

As described in section 2.1 the shape of the momentum transfer of Primakoff events depends on the beam energy and the target material. For a high energetic beam at COMPASS and the sufficiently high atomic number of nickel, the four-momentum transfer is mostly close to zero. Due to imperfections of the apparatus, the peak can only be reconstructed to the limit given by the experimental resolution. However the resolution of the COMPASS spectrometre is sufficent to clearly distinguish the peak as seen in Fig. 6.10.
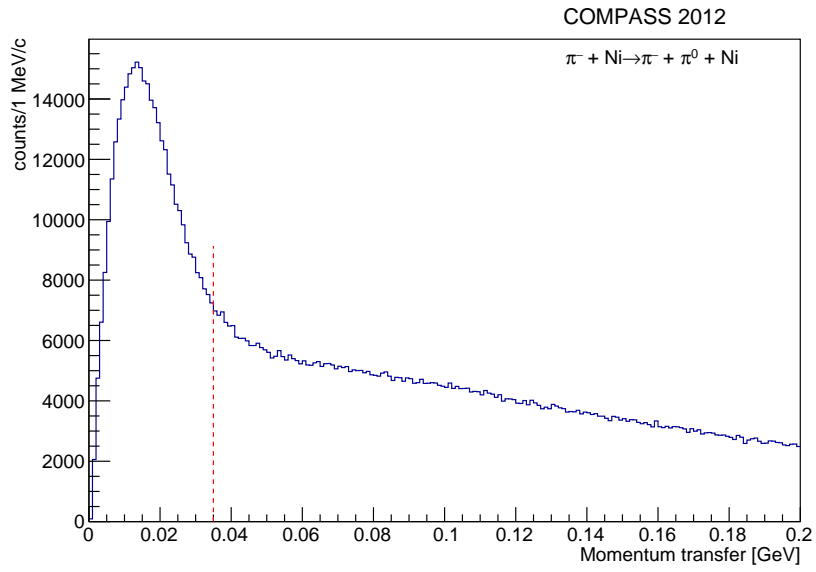
Figure 6.10: Spectrum for $|Q|$ for 2012 events after all cuts are applied except the $|Q|$ cut. The peak on the left is stemming from Primakoff events. The dashed red line indicates the applied cut.

6.2 Data stability

When taking data over a longer period of time, deviations in the data due to e.g. temperatur fluctuations or broken detectors occur. In Fig. 6.11 the $m_{\pi^-\pi^0}$ invariant mass is shown separately for all periods. The data fits nicely for every period except W30 where the CEDAR detector calibration has to be adjusted. As the induced background is well understood, no influence to the analysis is expected.
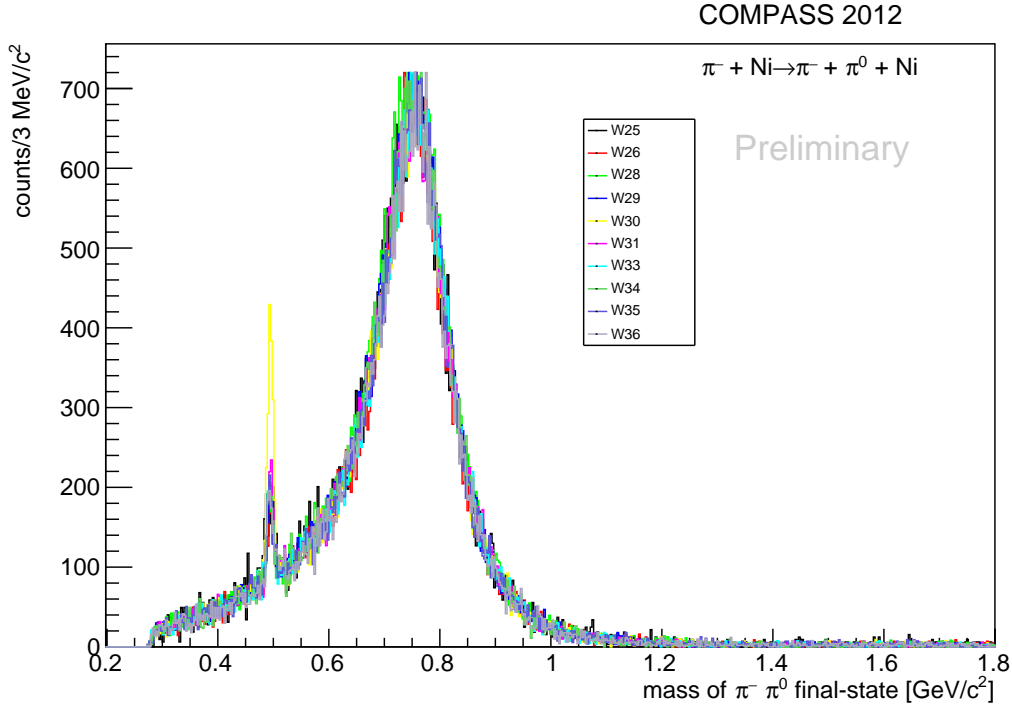
Figure 6.11: Invariant mass spectrum of $m_{\pi^-\pi^0}$ final state for each data taking period in 2012 normalized to maximum.

6.3 A closer look at the $\pi^- \pi^0$ final-state mass distribution

In this section the result in terms of the invariant-mass distribution of the two pion final state is presented. As it can be seen in figures 6.12 and 6.13, the main contribution to the final state is from ρ mesons that are produced via the Primakoff effect. The beam pion is spin-excited by the photon of the electromagnetic field of the nucleus. The ρ meson decays predominantly in the observed final state of a π^- and a π^0 [16].

In the logarithmic plots an excess at about $1.7\,\mathrm{GeV/c^2}$ can be seen. In this region two excited ρ meson states are claimed to exist, namely $\rho_3(1690)$ and $\rho(1700)$ [16]. A detailed analysis is presented in 7.5.

It has to be taken into account that the photon flux is dependent on the invariant mass and therefore has an influence on the shape of the distribution especially below $1\,\mathrm{GeV/c^2}$. For more details it is referred to the analysis chapter.

For both years a significant contribution of beam Kaon decay can be seen, that has been miss-identified by the CEDAR detector analysis as a pion.

In Fig. 6.15 the invariant mass spectrum is shown for both the nickel and the tungsten target.

In Fig. 6.16 the invariant mass spectrum is shown for events with a beam particle tagged as a kaon. The target region is cut out here. As still the $\rho(770)$ peak is visible, events with miss-identified beam particles contribute to the spectrum. As the peak decreases when sparing the region even more generously, it is concluded that the events in the ρ region are stemming from Primakoff reactions of miss-identified pions in the target with unprecisely determined z position of the vertex.

(a)

(b)

Figure 6.12: Invariant mass of $\pi^-\pi^0$ final state for 2012 data. Most events are stemming from ρ decay. At around 495 MeV/c a peak at the kaon mass can be seen.
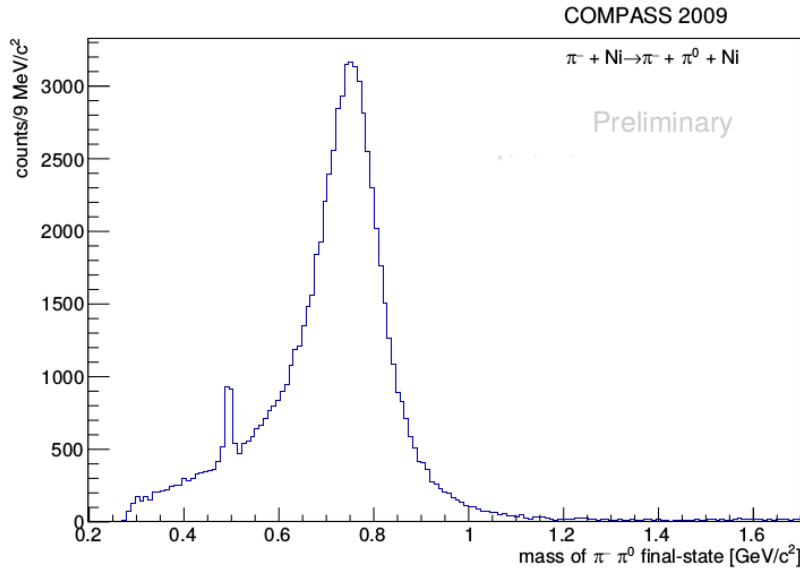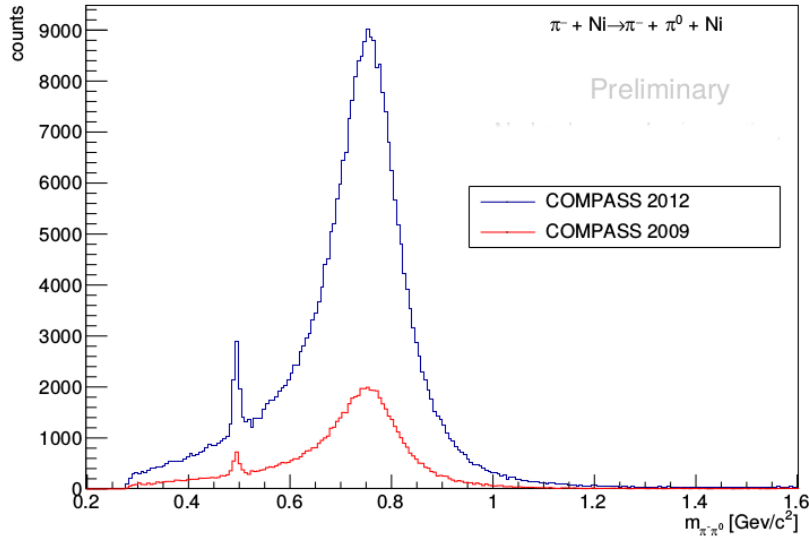
(a)
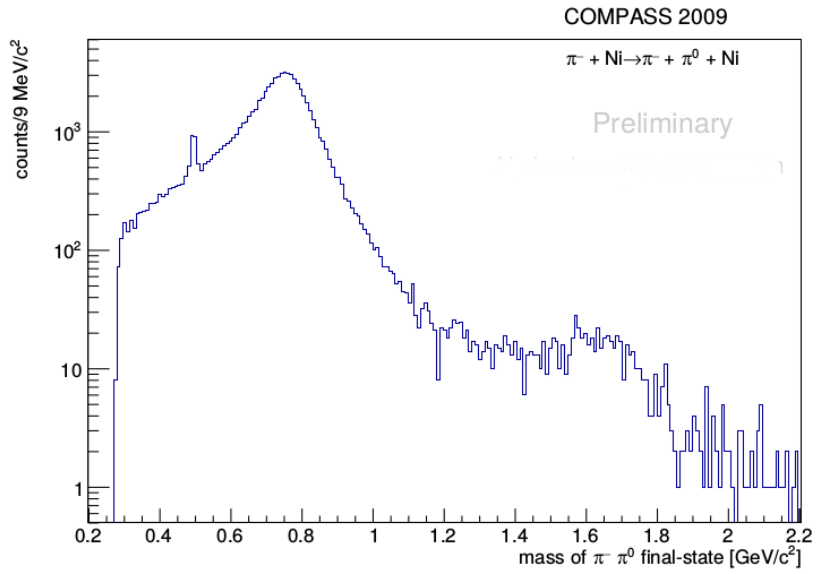
(b)

Figure 6.13: Invariant mass of $\pi^- \pi^0$ final state for 2009. Most events are stemming from ρ decay. At around $495\,\mathrm{MeV/c}$ a peak at the kaon mass can be seen.

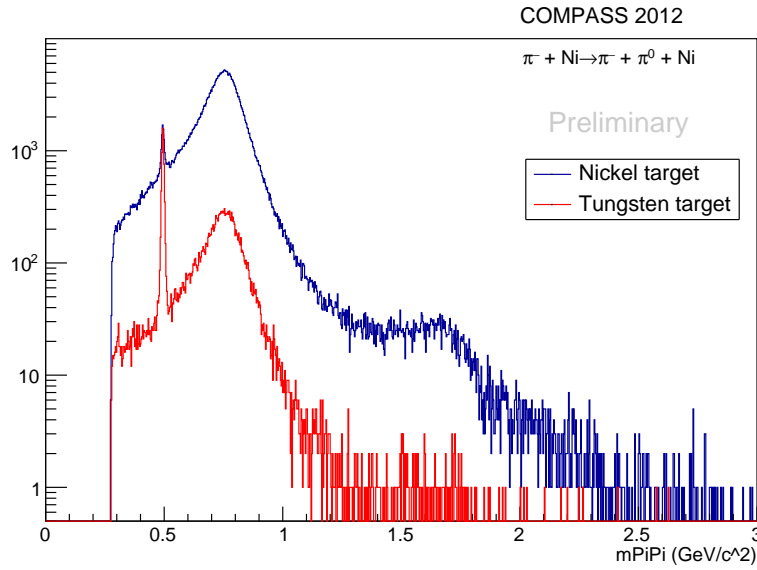Figure 6.14: Invariant mass of $\pi^-\pi^0$ final state for 2009 and 2012 data.

Figure 6.15: Invariant mass of $\pi^-\pi^0$ final state for the tungsten target and the nickel target.
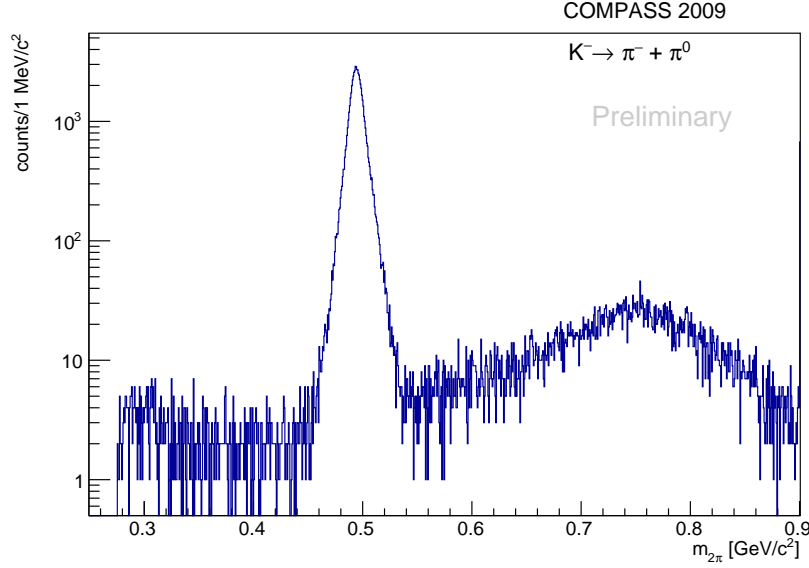
Figure 6.16: Invariant mass of $\pi^-\pi^0$ final state for beam particles tagged as kaons for vertex positions upstream and downstream the nickel target not including the tungsten target.

6.3.1 Distributions for the scattering angle θ_{GJ}

The $\pi^-\pi^0$ final states, that are produced via the $\rho(770)$ resonance are expected to have an angular distribution in θ_{GJ} proportional to $1 - \cos^2(\theta_{GJ})$ as the ρ meson has a total angular momentum $J = 1$ (compare section 7.5). The same angular distribution is expected in the low $m_{\pi^-\pi^0}$ region that is dominated by the chiral anomaly.

In Fig. 6.17 the angular distribution is plotted for both mentioned regions. Due to the acceptance effects discussed in section 7.2 the distributions are not symmetric around 0, but the p-wave is already somewhat visible.
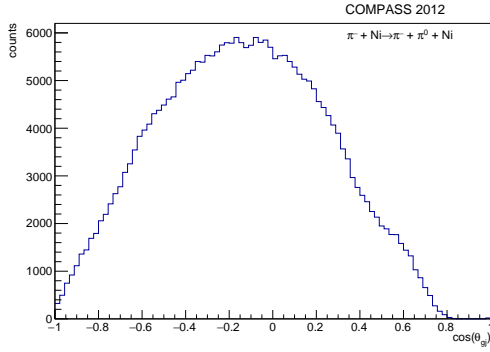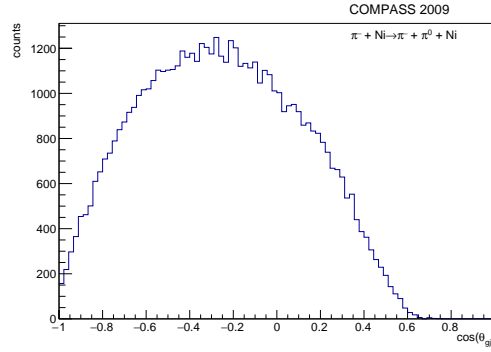
(a) 2012: $0.6\,\mathrm{GeV/c^2} < m_{\pi^-\pi^0} < 0.9\,\mathrm{GeV/c^2}$ (b) 2009: $0.6\,\mathrm{GeV/c^2} < m_{\pi^-\pi^0} < 0.9\,\mathrm{GeV/c^2}$
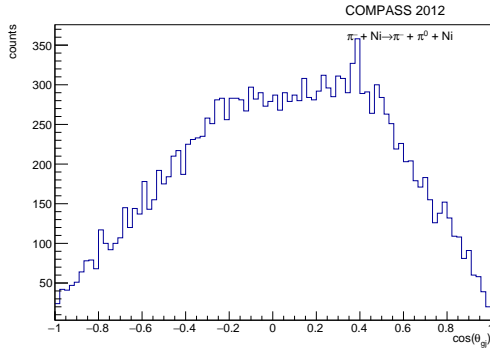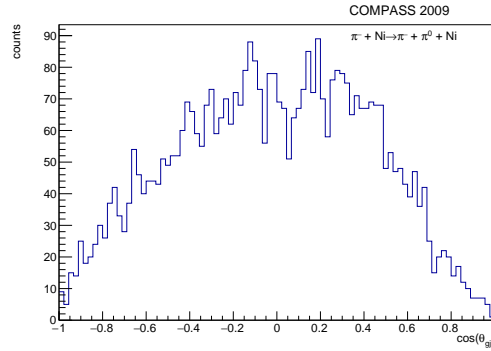
(c) 2012: $m_{\pi^-\pi^0} < 0.49\,\mathrm{GeV/c^2}$ (d) 2009: $m_{\pi^-\pi^0} < 0.49\,\mathrm{GeV/c^2}$

Figure 6.17: $\cos(\theta_{\mathrm{GJ}})$ for two different regions of $m_{\pi^-\pi^0}$ for 2009 and 2012 data.

Chapter 7

Analysis of $\pi^-\pi^0$

In this chapter all essential steps that were taken are described to extract the chiral anomaly $F_{3\pi}$ from the $\pi^-\pi^0$ final state kinematic distributions. For the analysis an accurate Monte Carlo simulation is crucial. Due to the known inaccuracies of the Monte Carlo simulation for 2012 data (compare chapter 5), the analysis is performed for 2009 data only.

7.1 Background estimate

There are three main processes that contribute to the background.

- K^- decay into $\pi^-\pi^0$, $e^-\pi^0\bar{\nu}_e$, $\mu^-\pi^0\bar{\nu}_\mu$

- K^- decay into $\pi^-\pi^0\pi^0$

- $\pi^- + \mathrm{Ni} \to \pi^- + \pi^0 + \pi^0 + \mathrm{Ni}$

The Kaon decay into two pions can be easily identified, as these occur only at a well known mass range in the invariant mass spectrum. As the shape of the background is known it is not subtracted but implemented in the theoretical fit function.

The same argument cannot be applied for the $e^-\pi^0\bar{\nu}_e$ and $\mu^-\pi^0\bar{\nu}_\mu$ as the neutrino is not reconstructed. Therefore the mass of the $e^-\pi^0$ and $\mu^-\pi^0$ final state would be shifted to lower values. These tail to lower masses is not visible as shown in Fig. 6.16. It is concluded that these events do not contribute to the mass spectrum, as the events presumably discarded by applying cuts on the exclusivity and momentum transfer.

The Kaon decay into three pions has a branching ratio that is one order of magnitude smaller than for $\pi^-\pi^0$ [16]. As the acceptance for $\pi^-\pi^0\pi^0$ events, when applying the proposed $\pi^-\pi^0$ event selection is significantly smaller, it can be concluded that the effect is negligible.

This section will concentrate on estimating the background stemming from $\pi^- + \mathrm{Ni} \to \pi^- + \pi^0 + \pi^0 + \mathrm{Ni}$.

This process contributes as background most likely for events involving at least one low energtic π^0 as the photons stemming from its decay may not hit the calorimeter. If the π^0 is sufficiently low energeti, i.e. its energy is a few GeV, these events cannot be removed by the exclusivity cut. However most events are discarded by the cut on the 4-momentum transfer.

To estimate the background Monte Carlo $\pi^-\pi^0\pi^0$ events are used. The Monte Carlo events, evenly distributed in the available phase space, are weighted according to the model and total cross section obtained in [30]. The $\pi^-\pi^0\pi^0$ final state can be produced either via the Primakoff process or via diffractive production. Both mechanisms are simulated and weighted independently. As seen in Fig. 7.1 the estimated background fits the observed $|Q|$-spectrum for all invariant mass regions for the higher $|Q|$-region. Events with lower $|Q|$-region are mostly steming from correctly identified $\pi^-\pi^0$ events.

(a) full dataset

(b) $0.2\,\mathrm{GeV/c^2} < m_{\pi^-\pi^0} < 0.4\,\mathrm{GeV/c^2}$

(c) $0.5\,\mathrm{GeV/c^2} < m_{\pi^-\pi^0} < 0.9\,\mathrm{GeV/c^2}$

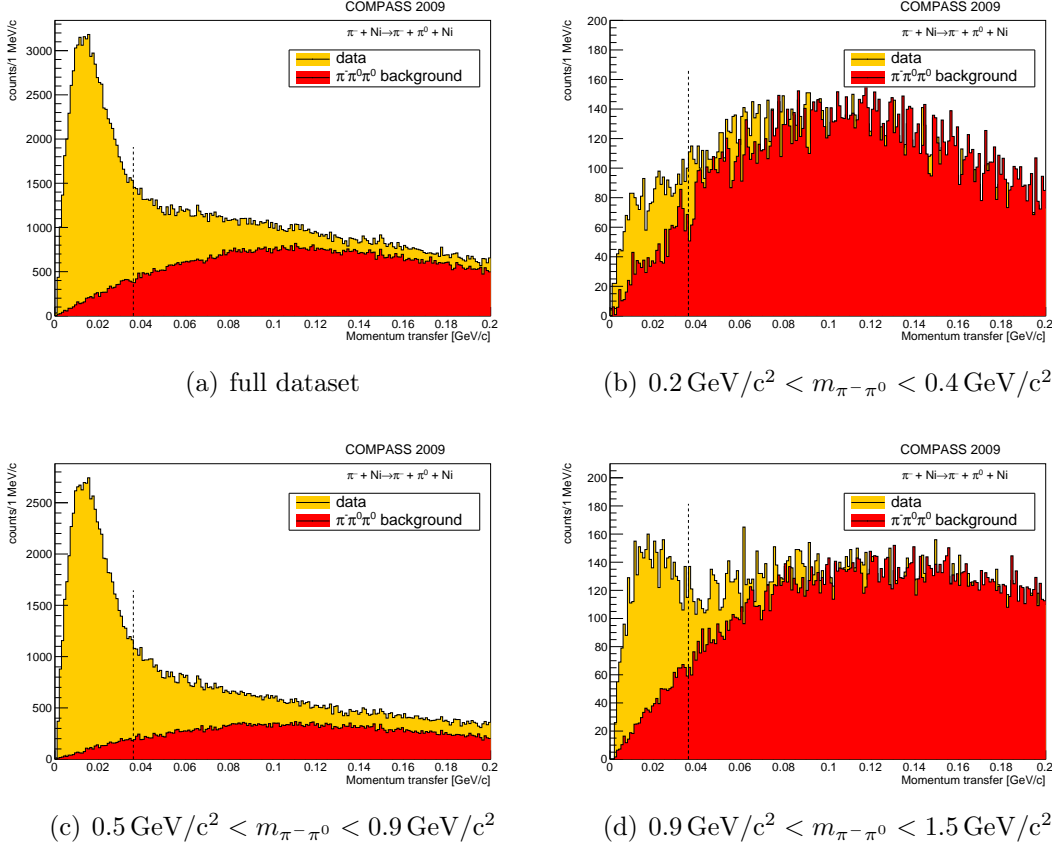(d) $0.9\,\mathrm{GeV/c^2} < m_{\pi^-\pi^0} < 1.5\,\mathrm{GeV/c^2}$

Figure 7.1: Distribution of the four-momentum-transfer for reconstructed data and estimated background from $\pi^-\pi^0\pi^0$ for different $m_{\pi^-\pi^0}$ regions. The black dashed line indicates the cut applied on the momentum transfer.

The estimated background is shown in Fig. 7.2. The background contributes most for small invariant mass $m_{\pi^-\pi^0} < 0.5\,\mathrm{GeV/c}$ and masses well beyond the $\rho(770)$ resonance.

As shown in Fig. 7.3 the exclusivity of background events is slightly shifted to negative values due to a missing π^0, but the lost π^0 is sufficiently low energetic that most events are kept after the exclusivity cut.

Most events stemming from $\pi^-\pi^0\pi^0$ are discarded by requiring exactly two hits in ECAL2. In addition the cut on the momentum transfer has a huge impact, as most $\pi^-\pi^0\pi^0$ events are produced via diffractive production at higher momentum transfers. The Primakoff $\pi^-\pi^0\pi^0$ events are shifted to higher momentum transfer as one π^0 is missing. Therefore the background is mostly at high momentum transfer as shown in Fig. 7.1.
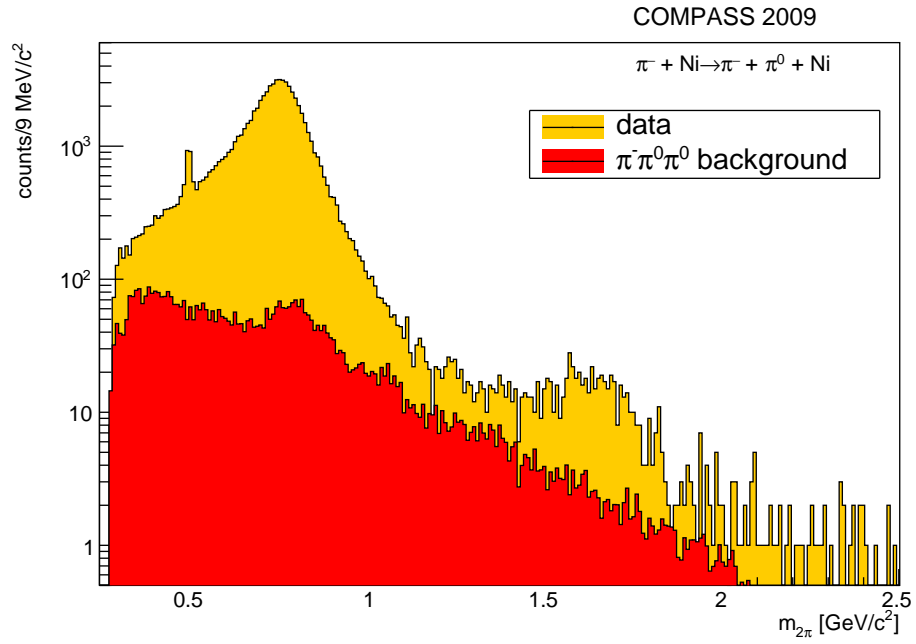
Figure 7.2: Background estimation for $\pi^-\pi^0\pi^0$ via weighted Monte Carlo events.
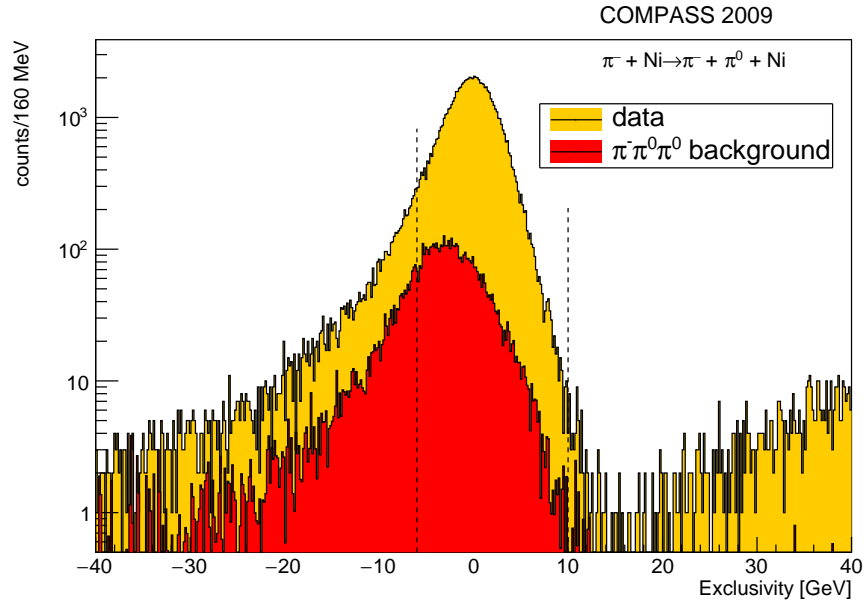

Figure 7.3: Exclusivity of $\pi^-\pi^0\pi^0$ background events compared with reconstructed data.

Additional background could be stemming from $\rho(770)$ production via omega exchange. This interesting background is not yet studied but expected.

7.2 Acceptance correction

For a detailed understanding of the measured data, the unavoidable imperfections of the apparatus have to be taken into account. To correct these imperfections a realistic Monte Carlo simulation of the experiment is essential. The Monte Carlo data is processed through the full analysis chain that has been described in chapter 4.

The generated events, containing beam particle and scattered pions, are evenly distributed in s, θ_{GF} and ϕ_{TY} (compare section 2.1.1), and with a realistic $|Q|$ distribution.

The acceptance is defined as the ratio of the total number of Monte Carlo events and the number of accepted events after applying all cuts. The acceptance correction is performed in s, θ_{GF} and ϕ_{TY} simultaneously.

Events that have an overall energy deposit of less than $78\,\mathrm{GeV}$ in the active trigger region are discarded for both Monte Carlo events and real data. Above this energy deposit the Primakoff trigger has an efficiency of approximately 100%, therefore a detailed simulation of the trigger is not necessary (compare section 3.2.2).

7.2.1 Energy calibration

The position dependend energy calibration, that is performed for real data, cannot be applied to the Monte Carlo data. The cluster energy of Monte Carlo events are corrected by the linear function

$$E_{\mathrm{Cluster,corrected}} = 0.094\,\mathrm{GeV} + 0.979\,\mathrm{GeV}^{-1} \cdot E_{\mathrm{Cluster,\ reconstructed}}. \tag{7.1}$$

The values are obtained by fitting the respective distribution shown in Fig. 7.4, which proves the respective scaling factor and offset to be necessary.
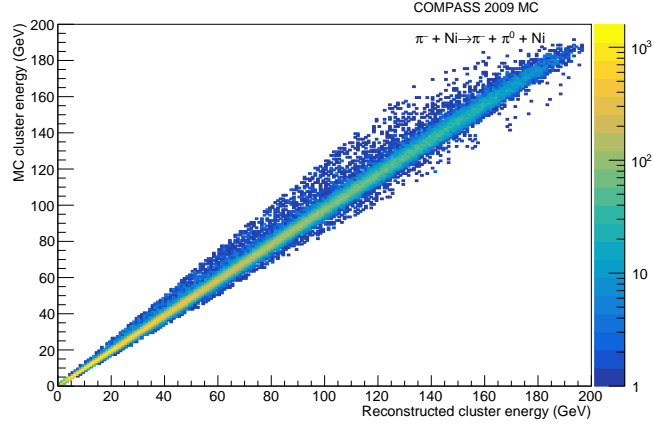
Figure 7.4: Monte Carlo truth cluster energy vs. reconstructed cluster energy.
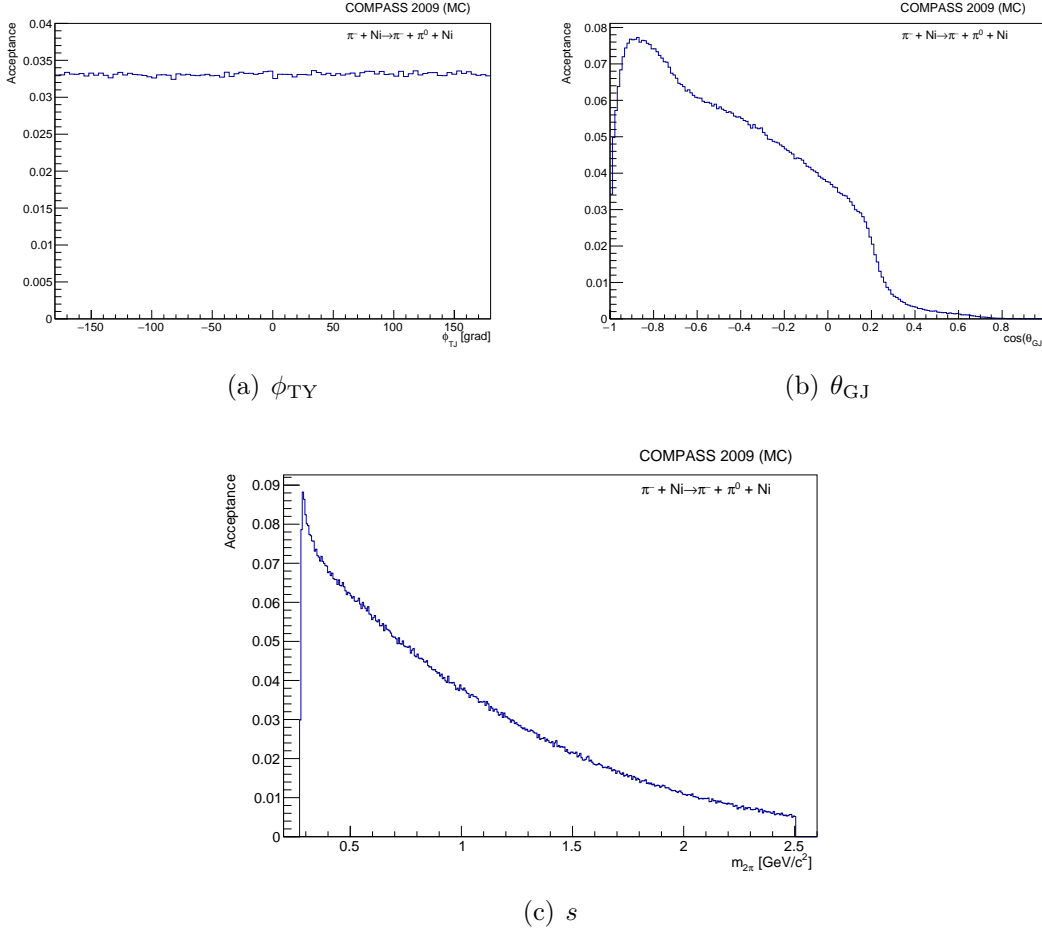
7.2.2 Acceptances

In Fig. 7.5 the acceptances are shown for the quantities that are used for the acceptance correction.

The acceptance for ϕ_{TY} is flat, as this angle is not directly linked to any quantity in the lab system, and the x- and y-axis of the Gottfried-Jackson-Frame are rotated randomly with reference to the lab reference system.

The acceptance is mostly dominated by the photon reconstruction. The higher the π^0 energy the more likely the resulting photons are reconstructed and enough energy is deposited in the active trigger region. Therefore the acceptance in $\cos(\theta_{\mathrm{GJ}})$, which is directly linked to the π^0 energy (compare section 2.1.1), is decreasing for higher values of $\cos(\theta_{\mathrm{GJ}})$. For $\cos(\theta_{\mathrm{GJ}}) > 0.2$ the acceptance drops rapidly to 0 as the energy in the calorimeter is not sufficient for the Primakoff trigger.

Without cutting on the momentum transfer the acceptance in the invariant mass s is slowly for values above $0.5\,\mathrm{GeV/c}$ and around 10%. However with increasing invariant mass $Q_{\min}$ for Primakoff events is shifted to higher values (compare Eq. (2.3)) leading to further decreasing acceptance.

(a) ϕ_{TY}

(b) θ_{GJ}

(c) s

Figure 7.5: Acceptance in (a) ϕ_{TY}, (b) θ_{GJ} and (c) s.

7.2.3 Acceptance corrected spectra

In Fig. 7.6 the acceptance corrected spectrum for $\cos(\theta_{\mathrm{GJ}})$ is shown. The distribution has then the maximum at 0 and has a shape close to the expected $L = 1, M = 1$ p-wave. The deviations from a pure p-wave are steming from contributions of s-wave, f-wave and possibly d-wave. For detail it is referred to 7.5. The $\cos(\theta_{\mathrm{GJ}})$ spectra for different invariant mass regions is given in Appendix A.

As for $\cos(\theta_{\mathrm{GJ}}) > 0$ the number of events is dropping due to the Primakoff trigger and the distribution is expected to be symmetric around 0, only events with $\cos(\theta_{\mathrm{GJ}}) < 0$ are considered.
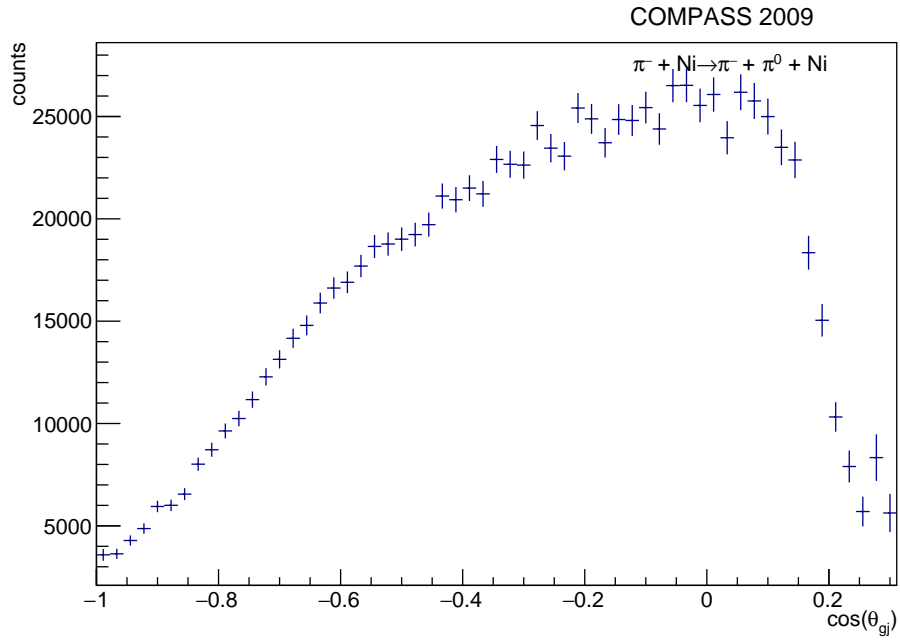
Figure 7.6: Acceptance corrected spectrum for $\cos(\theta_{\mathrm{GJ}})$.

The acceptance correction is performed independently for the reconstructed data and the estimated background. The resulting invariant mass distribution is shown in Fig. 7.7.
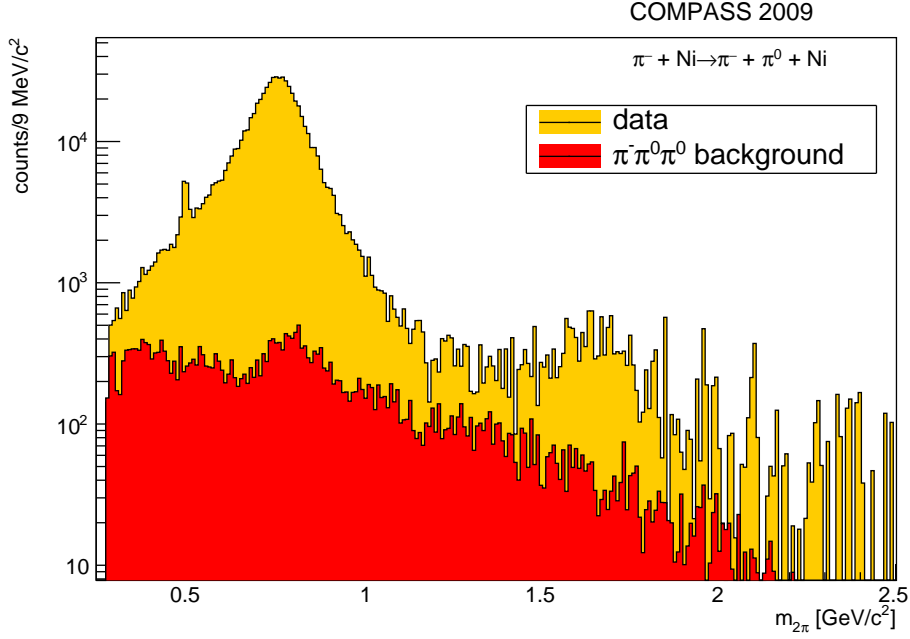
Figure 7.7: Distribution for the invariant mass of the 2π final state and the estimated background after acceptance correction.

7.3 Normalization to the photon flux

According to the Weizsäcker-Williams approximation the cross section for the process is factorized into a term describing the photon density and a term describing the photon pion interaction. To compare the result to the theory prediction given in [25], the spectrum of the invariant mass $m_{\pi^- \pi^0}$ has to be normalized by the photon flux.

The t and m dependence is given by

$$d_{\text{WW}}(m, Q) = \frac{Z^2 \alpha}{\pi (m^2 - m_\pi^2)} F^2(Q^2) \frac{Q^2 - Q_{\text{min}}^2}{Q^4}, \qquad (7.2)$$

which has been taken from Eq. (2.3), the nucleus elastic form factor F described in Eq. 2.5 and Q_{min} given by Eq. 2.4.

To calculate the correct number of events per mass bin, the flux needs to be

81

integrated for each bin from m_{low} to m_{high} as:

$$D_{m,t} = \int\limits_{E_{\text{beam}}} \int\limits_{m_{\text{low}}}^{m_{\text{high}}} \int\limits_{Q_{\text{min}}}^{Q_{\text{max}}} \mathrm{d}E_{\text{beam}} \mathrm{d}m \mathrm{d}Q \bar{\rho}_{\text{beam}}(E_{\text{beam}}) \cdot d_{\text{WW}}(m,t) \qquad (7.3)$$

where ρ_{beam} denotes the normalized beam energy distribution. As the beam energy within narrow energy range it is approximated as a Gaussian around 191 GeV and a width of $\sigma_{\text{beam}} = 2\,\text{GeV}$ as suggested in [30]. $Q_{\text{max}} = 0.036\,(\text{GeV/c})^2$ is chosen according to the proposed event selection.

The evaluated integral yields the result seen in Fig. 7.8.
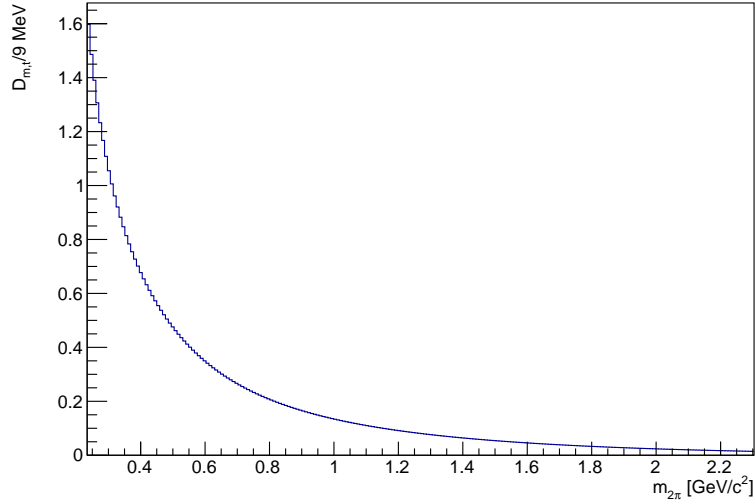
Figure 7.8: Photon flux according to Weizsäcker-Williams approximation.

7.4 Determination of beam luminosity

The model given to extract the chiral anomaly is not only sensitive to the shape of the invariant mass distribution but also to the cross section given by the number of events normalized to the beam luminosity.

To determine the integrated luminosity $\int \mathcal{L}_\pi \mathrm{d}t$ of pions in the 2009 run, the distributions and intensity of the decay of beam kaons is used. The lifetime of the charged kaon is known with high precision and the kaon fraction in the COMPASS beam is known with 5% relative uncertainty. Thus by knowing the number of free kaon decays in a certain volume the total amount of pions can be calculated.

In the following method the decay of the charged kaon into $\pi^-\pi^0$ is used. This decay has quite a high branching ratio of about 20% [16] and due to using the same final state as in the analysis unkown systematic effects can be compensated.

7.4.1 Event selection

The event selection is based on the selection described in section 6.1 with some modifcations. The CEDAR cut is inverted and only beam particles tagged as Kaons are accepted. The cut on the primary vertex position is adapted. As the real momentum transfer is zero, the cut on the reconstructed momentum transfer is applied more strictly requiring $|Q| < 0.02\,\mathrm{GeV/c}$ to discard events from decay channels involving neutrinos.

7.4.2 Calculation of beam luminosity

The number of kaon decays is determined by weighting the number of Monte Carlo events of the Kaon decay to match the number of reconstructed Monte Carlo events with reconstructed events in the real data. The number of weighted Monte Carlo events before the selection then corresponds to the actual number of kaon decays.

To enable this procedure the Monte Carlo events of the kaon decay are distributed in the available phase space as expected for the free kaon decay.

The decay volume is selected according to Fig. 7.11, sparing the target region as well as for z positions below $-130\,\mathrm{cm}$. Below this value the number of Monte Carlo events is decreasing as the Monte Carlo simulation includes events only until $z \approx -140\,\mathrm{cm}$.

The acceptance of $K^- \to \pi^-\pi^0$ is shown in Fig. 7.9. Events downstream the target have twice the acceptance compared to events upstream the target. This effect is caused by interaction with the Nickel target.
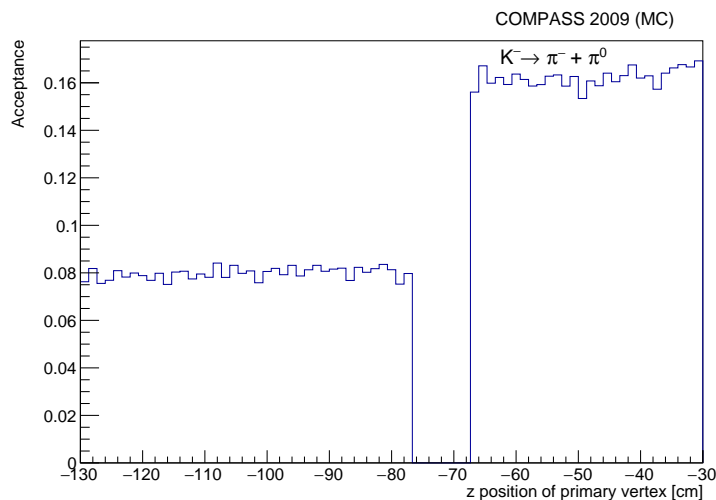

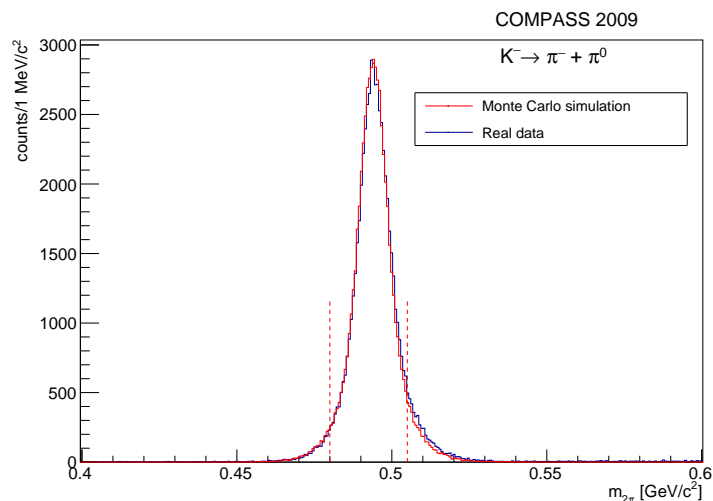Figure 7.9: Acceptance of $K^- \to \pi^-\pi^0$.

Figure 7.10: Invariant mass of the $\pi^-\pi^0$ final state for weighted Monte Carlo events and reconstructed data. The red dashed lines mark the area of considered events.
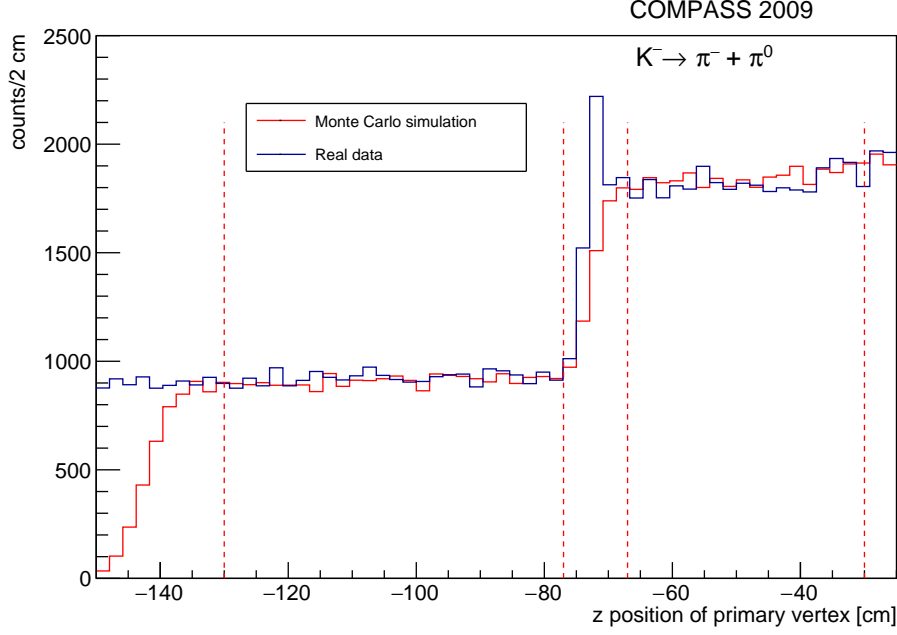
Figure 7.11: z position of primary vertex for weighted Monte Carlo events and real data. The red dashed lines indicate the selected decay volume, excluding the target region between $z = -77$ cm and $z = -67$ cm as well as the region for $z < -130$ cm and $z > -30$ cm.

The integrated beam kaon flux can be calculated by dividing number of true kaon decays in $\pi^-\pi^0$ by the percentage of kaons that are expected to decay into this final state within the selected decay volume. Weighting this quantity with the relative kaon fraction in reference to the pion content of the beam at the target and the tag efficiencies of the CEDAR detectors, the integrated flux of correctly tagged pions can be calculated as given in Eq. (7.4).

$$\int \Phi_\pi \mathrm{d}t = \frac{N_{\mathrm{K,c}}}{\left(1 - e^{-\frac{l}{c\beta\gamma\tau}}\right) BR(K^- \to \pi^-\pi^0)\frac{N_{K^-,\mathrm{beam}}}{N_{\pi^-,\mathrm{beam}}}} \cdot \frac{\epsilon_{\pi^-}}{\epsilon_{K^-}} = 1.57(19) \times 10^{11}, \quad (7.4)$$

with $l = 0.9$ m being the length of the selected decay volume, $\epsilon_{K^-} = 0.869$ the kaon tag efficiency of the CEDAR[30], $\epsilon_{\pi^-} = 0.934$ the pion tag efficiency [40] and $N_{\mathrm{K,c}} = 506 \times 10^3$ the acceptance corrected number of kaon decays, 298×10^3 upstream the target and 208×10^3 downstream.

$$\frac{N_{K^-,\mathrm{beam}}}{N_{\pi^-,\mathrm{beam}}} = \frac{2.59}{97} \quad (7.5)$$

85

is the relative kaon fraction. $\tau = 1.2380 \times 10^{-8}\,$s is the lifetime of the charged kaon taken from [16]. $\beta = \frac{v}{c}$ is approximated by 1 as the kaons are highly relativistic. $BR(K^- \to \pi^-\pi^0) = 0.2066$ is the branching ratio for the decay into $\pi^-\pi^0$ [16]. The Lorentz factor γ can be calculated, using the average beam energy $\bar{E}_{\text{beam}} = 191\,$GeV and the mass of the charged kaon taken from [16], with the following equation:

$$\gamma = \frac{\bar{E}_{\text{beam}}}{m_{K^-} \cdot c^2}. \tag{7.6}$$

In order to obtain the luminosity the pion flux has to be multiplied by the particle density per area of the 4.2 mm thin nickel disc.

$$\int \mathcal{L}_\pi \mathrm{d}t = \int \Phi_\pi \mathrm{d}t \cdot \frac{d \cdot \rho_{\text{Nickel}}}{AW_{\text{Nickel}}} = (6.0 \pm 0.7) \times 10^3\,\mu\text{b}^{-1}, \tag{7.7}$$

where $d = 4.2\,$mm is the thickness of the target, $\rho = 8.908\,$g/cm^3 the density of nickel and $AW_{\text{Nickel}} = 58.6934\,$u the atomic weight of nickel. The relative uncertainty introduced by the Monte Carlo simulation is estimated at 2.4% in addition to the 10% relative uncertainty of the kaon fraction in beam. Another contribution of 2% to the relative uncertainty is stemming from the unkown contribution of e^- or μ^- events. As argued in section 7.1, the contribution is presumably negligible, but needs careful checking.

The value is in tension with the value obtained in [30] ($\int \mathcal{L}_\pi \mathrm{d}t = (4.52 \pm 0.28) \times 10^3\,\mu\text{b}^{-1}$) using the $\pi^-\pi^0\pi^0$ final state.

The final normalized and acceptance corrected invariant mass distribution with subtracted background is shown in Fig. 7.12. The observed excess at around $1.7\,$GeV/c^2 is now clearly visible, even in the non-logarithmic presentation. The origin of this peak is discussed in more detail in the next section.
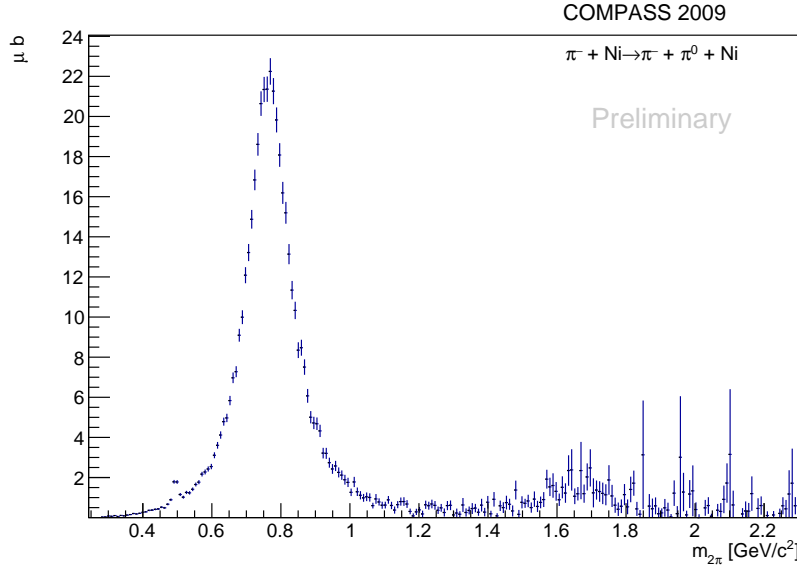
(a)
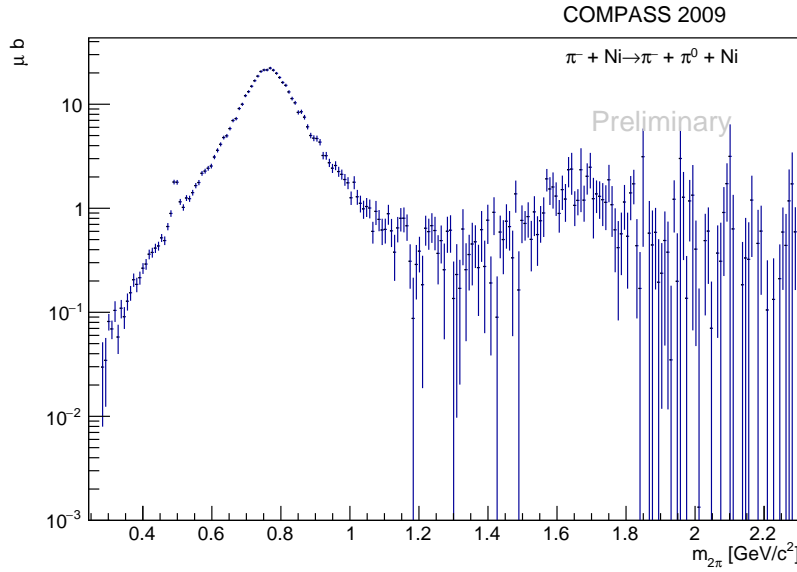
(b)

Figure 7.12: Final invariant mass spectrum of the $\pi^-\pi^0$ final state after acceptance correction, background subtraction and normalization to photon flux and luminosity. The bin width is chosen like for the calculated photon flux ($9\,\mathrm{MeV}/\mathrm{c}^2$).

7.5 Study of the ρ_3 peak

To investigate the origin of the peak observed around $1.7\,\mathrm{GeV/c^2}$ a very first partial wave analysis is performed for the whole mass spectrum. In the mass region above $1.4\,\mathrm{GeV/c^2}$ three particles decaying into $\pi^-\pi^0$ exist, namely $\rho(1450)$, $\rho_3(1690)$ and $\rho(1700)$. While the $\rho(1450)$, $\rho(1700)$ and $\rho(770)$ have total angular momentum $J=1$ the decay via a p-wave. The $\rho_3(1690)$ has total angular momentum $J=3$ and decays via an f-wave. Another particle contributing to the invariant mass spectrum is the K^- with total angular momentum $J=0$ and therefore decaying in a s-wave [16].

The spin of the ρ resonance is coming predominantly from the photon and is parallel to the beam axis due to spin conservation. The additional angular momentum of the $\rho_3(1690)$ is carried by the valence quarks, in the classical image rotation around their center of mass.

According to Fig. 7.13 it is most likely that the events are produced via the Primakoff effect, as all events not stemming from $\pi^-\pi^0\pi^0$ are at lower momentum transfer. At high invariant mass the Q_{min}, given in Eq. (2.4), is rising and the events are at higher momentum transfer. In addition the limited resolution of the detectors have to be taken into account. This gives a hint at a non-vanishing radiative coupling of the ρ_3 resonance.
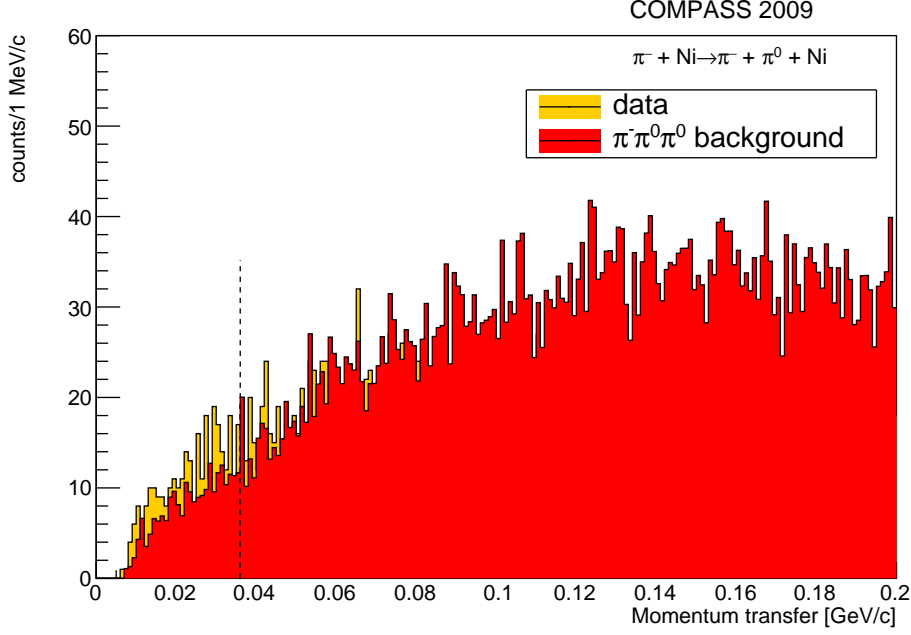
Figure 7.13: $|Q|$ distribution between $m_{\pi^-\pi^0} = 1.6\,\mathrm{GeV/c}$ and $m_{\pi^-\pi^0} = 1.8\,\mathrm{GeV/c}$ with the estimated background.

The angular distributions are taken from [41] and are given as follows:

$$d_{00}^0(\theta) = \frac{1}{2} \qquad\qquad \text{(s-wave)}$$

$$d_{10}^1(\theta) = -\frac{\sqrt{3}}{2}\sin(\theta) \qquad\qquad \text{(p-wave)}$$

$$d_{10}^3(\theta) = -\sqrt{3}\sin(\theta)(\frac{5}{4}\cos(\theta) - \frac{1}{4}). \qquad\qquad \text{(f-wave)}$$

While the p-wave and f-wave have to be summed coherently, due to the same production mechanism, this is not the case for the s-wave of the Kaon decay. The fit of the angular distribution is performed in $100\,\mathrm{MeV/c^2}$ mass bins and between $600\,\mathrm{MeV/c^2}$ and $1\,\mathrm{GeV/c^2}$ in $50\,\mathrm{MeV/c^2}$ mass bins. As an approximation the Breit-Wigner-Distribution is assumed to be constant within the mass bins yielding the following ansatz for the fit function $\mathcal{F}(\theta)$:

$$\mathcal{F}(\theta, m_{\pi^-\pi^0}) = \left|A_p(m_{\pi^-\pi^0}) \cdot d_{10}^1(\theta) + A_f(m_{\pi^-\pi^0}) \cdot d_{10}^3 \cdot e^{i\phi}\right|^2 + \left|A_s(m_{\pi^-\pi^0}) \cdot d_{00}^0(\theta)\right|^2,$$
$$(7.8)$$

with A_p, A_f and A_s being the amplitudes of the respective waves and ϕ the relative

phase between p-wave and f-wave. The respective intensities are given by the square of the amplitudes.

The fit results for each mass bin is given in Fig. A.1 in the appendix, three examples are given in Fig. 7.14.

(a) $0.45\,\mathrm{GeV/c^2} < m_{\pi^-\pi^0} < 0.5\,\mathrm{GeV/c^2}$

(b) $0.77\,\mathrm{GeV/c^2} < m_{\pi^-\pi^0} < 0.78\,\mathrm{GeV/c^2}$

(c) $1.65\,\mathrm{GeV/c^2} < m_{\pi^-\pi^0} < 1.7\,\mathrm{GeV/c^2}$
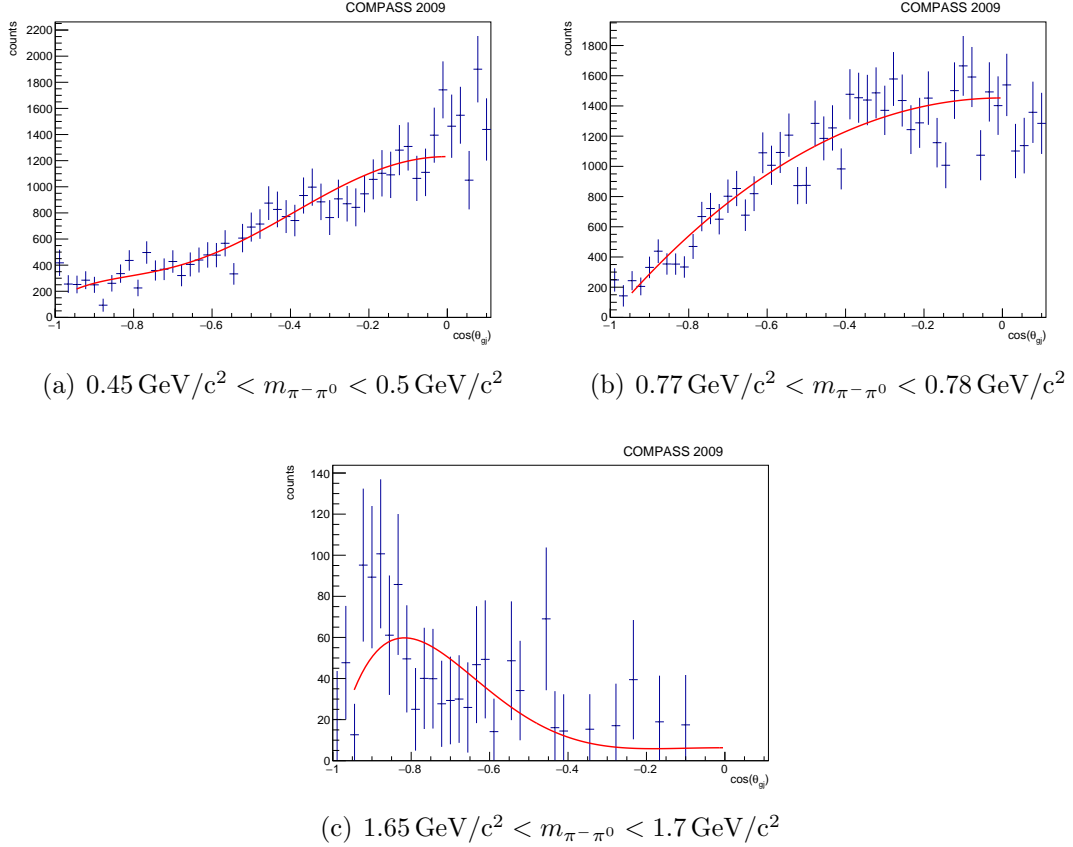
Figure 7.14: Fit result for $\mathcal{F}$ in different mass bins. In (a) the influence of the s-wave stemming from the K^- decay can be seen as an offset of the fit function. The distribution in (b) is dominated by the p-wave of the $\rho(770)$ while in (c) the influence of the f-wave of the $\rho_3(1690)$ can be seen.

The obtained intensities of the partial waves are shown in Fig. 7.15. Around the $\rho(770)$ resonance the p-wave is dominant and the interference term is changing its sign at the resonance mass as expected. Around the peak at $1.6\,\mathrm{GeV/c}$ the f-wave is dominant. Thus the observed peak is stemming from the $\rho_3(1690)$, although the partial wave peaks at too low values. As there is not much data available in this region, this is still consistent with the expectation.

A small excitation in the p-wave is also visible in this region, hinting for some contribution of the $\rho(1700)$. This result is consistent with results of advanced partial wave analysis performed on COMPASS data for other final states, where only a small contribution of the $\rho(1700)$ was visible compared to the $\rho_3(1690)$ contribution. Due to the limited amount of data, it cannot be claimed that this contribution is stemming from the $\rho(1700)$.
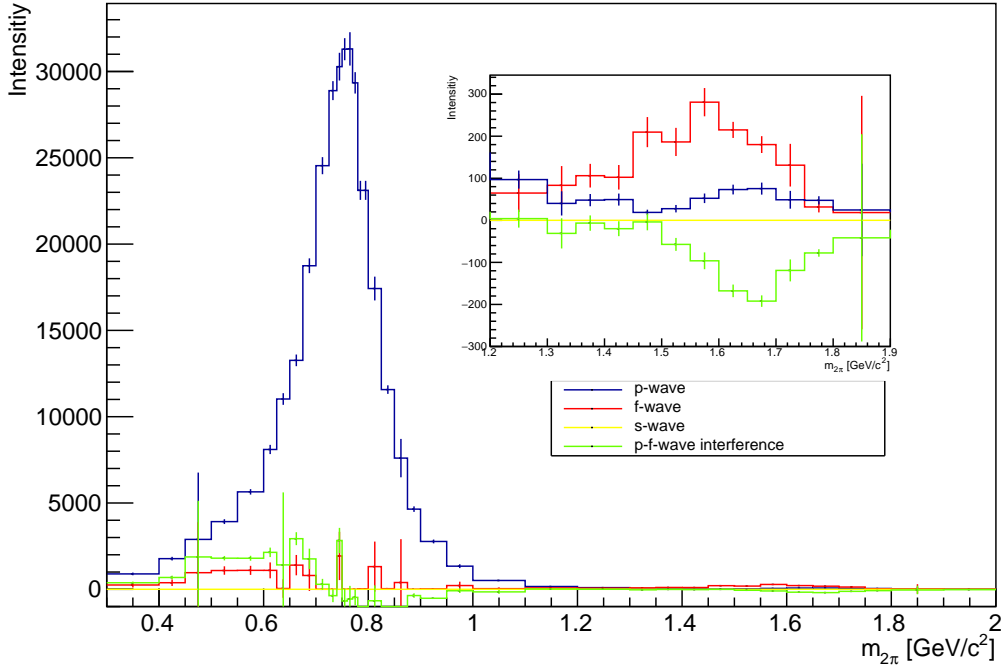
Figure 7.15: Intensities of the partial waves over the invariant mass. For the $\rho(770)$ region the p-wave is dominant. The region above $1.5\,\mathrm{GeV/c^2}$ is dominated by the f-wave.

7.6 Extraction of the chiral anomaly

Finally the obtained $m_{\pi^- \pi^0}$ spectrum is fitted to the theory prediction given in [25]. An additional term for the kaon peak is added to the model by the function $A_\mathrm{K}(s)$.

The differential cross section then given by:

$$\sigma(s) = A_\mathrm{K}(s) + \frac{(s - 4M_\pi^2)^{\frac{3}{2}}(s - M_\pi^2)}{1024\pi\sqrt{s}} \int\limits_{-1}^{0} \mathrm{d}z(1 - z^2)\left|\mathcal{F}(s, t, u)\right|^2, \qquad (7.9)$$

where s, t, u denote the Mandelstam variables and $z = \cos(\theta_\mathrm{GJ})$, has two free parameters $C_2^{(1)}$ and $C_2^{(2)}$, the prefactors of the partial waves contribution to $\mathcal{F}$, obtained by the fit. The limits of the integral correspond to the fact that only events with $\cos(\theta_\mathrm{GJ}) < 0$ are considered.

The kaon peak is described by the sum of two Gaussian distributions. This is necessary because kaon decays upstream and downstream the target contribute. Due to interaction with the target, the kaon mass distribution more wide for events upstream the target compared to events downstream the target.

The mean values and standard deviations of the two gaussian peaks are determined using the mass distribution shown in Fig. 6.16. The fit function is given by:

$$A_\mathrm{K}(s) = A_{\mathrm{K},1} \cdot e^{-0.5\left(\frac{\sqrt{s} - m_{\mathrm{K},1}}{\sigma_{\mathrm{K},1}}\right)^2} + A_{\mathrm{K},2} \cdot e^{-0.5\left(\frac{\sqrt{s} - m_{\mathrm{K},2}}{\sigma_{\mathrm{K},2}}\right)^2}. \qquad (7.10)$$

The fit shown in Fig. 7.16 gives the result presented in 7.1.

Parameter	Estimate	Standard Error
$A_{\mathrm{K},1}$ [Events/MeV/c^2]	2.24×10^3	0.02×10^3
$m_{\mathrm{K},1}$ [MeV/c^2]	494.1	0.1
$\sigma_{\mathrm{K},1}$ [MeV/c^2]	4.66	0.52
$A_{\mathrm{K},2}$ [Events/MeV/c^2]	0.52×10^3	0.02×10^3
$m_{\mathrm{K},2}$ [MeV/c^2]	494.6	0.9
$\sigma_{\mathrm{K},2}$ [MeV/c^2]	1.11	0.13

Table 7.1: Fit result for double gaussian describing the kaon mass distribution.
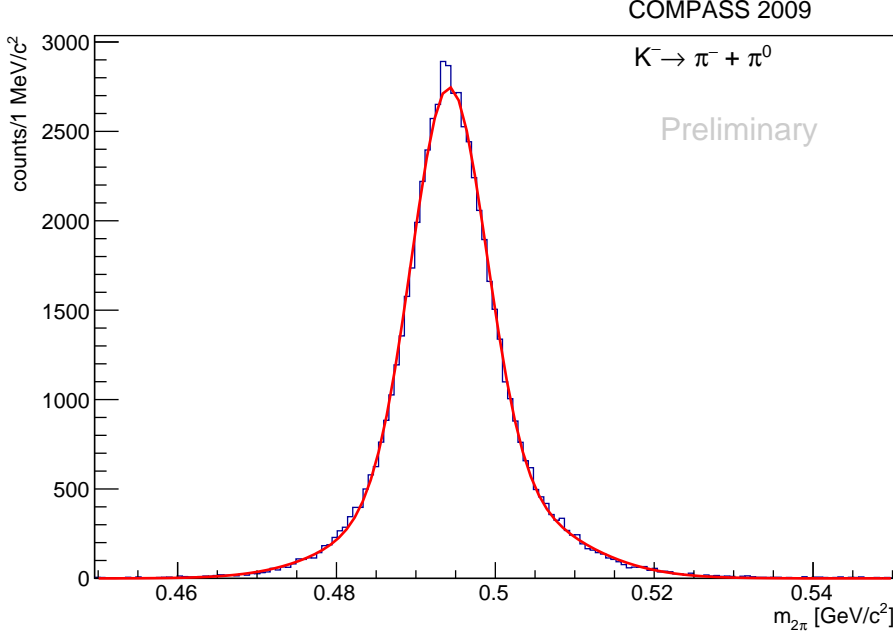
Figure 7.16: Invariant mass distribution for kaon decays upstream and downstream the target fitted with the function given in Eq. (7.10)

$m_{K,1}$ and $m_{K,2}$ as well as $\sigma_{K,1}$ and $\sigma_{K,2}$ are fixed and only the amplitudes are fitted to the $\pi^-\pi^0$ mass spectrum together with the free parameters $C_2^{(1)}$ and $C_2^{(2)}$. The fit to the $\pi^-\pi^0$ mass spectrum is shown in Fig. 7.17 and the result presented in table 7.2. The fit curve is in good agreement with the data, however for values below the kaon mass deviations can be seen in Fig. 7.17 (b). As in this region the background events contribute significantly, a more detailed study of the background may be necessary.

Parameter	Estimate	Standard Error
$C_2^{(1)}$ (GeV^{-3})	13.1	0.1
$C_2^{(2)}$ (GeV^{-5})	30.9	0.1
$A_{K,1}$ (µb)	1.74	0.11
$A_{K,2}$ (µb)	0.01	0.01

Table 7.2: Fit results
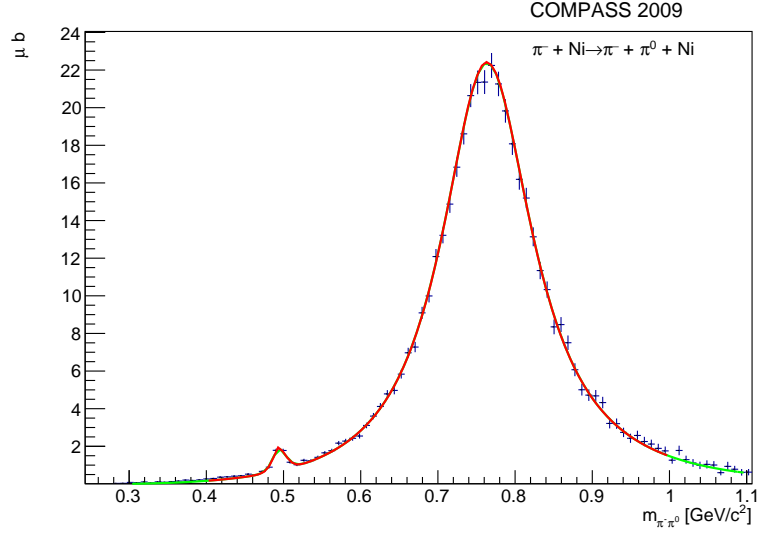
(a)
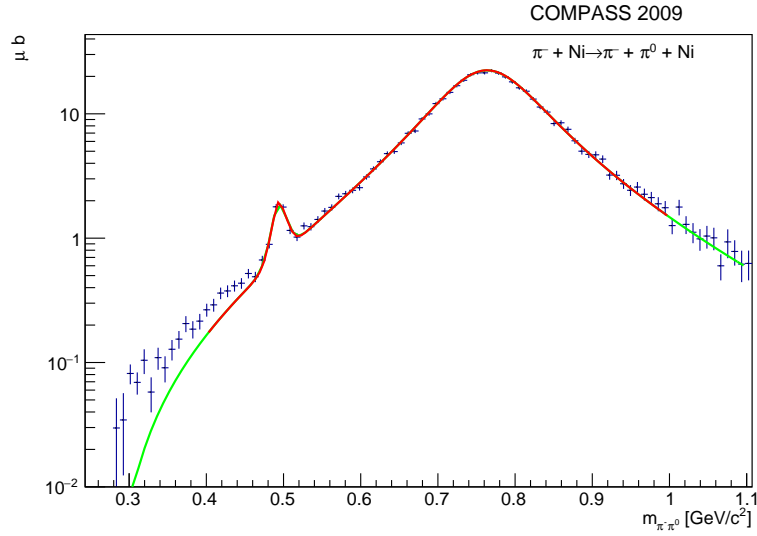
(b)

Figure 7.17: Result of the fit given in Eq. (7.9). The red curve indicates the fit range and the green curve the extrapolated fit result.

Using the result the radiative width of the ρ meson can be determined [42], yielding $\Gamma_\rho = 139\,\text{keV}$. This result significantly from $\Gamma_\rho = (81 \pm 8)\,\text{keV}$ proposed in [43] giving a hint for a problem concerning the overall normalization of the events by the luminosity. When normalizing the cross section in a way that the extracted

radiative width of the ρ meson matches the value obtained in [43], the values presented in table 7.3 are obtained.

Parameter	Estimate	Standard Error
$C_2^{(1)}$ (GeV^{-3})	10.4	0.1
$C_2^{(2)}$ (GeV^{-5})	24.6	0.1
$A_{K,1}$ (µb)	0.41	0.13
$A_{K,2}$ (µb)	0.47	0.07

Table 7.3: Fit results for histogram normalized by the radiative width of the ρ meson.

The chiral anomaly is defined as $\mathcal{F}(0,0,0)$. The extrapolation to $s = t = u = 0$ is performed using χPT:

$$C_2 = F_{3\pi}(1 + 3M_\pi^2\bar{C}) = C_2^{(1)} + C_2^{(2)}m_\pi^2 \tag{7.11}$$

where $\bar{C}$ is given by

$$\bar{C} = -\frac{64\pi^2}{3e}C_2^{\mathrm{r}}(\mu) - \frac{1}{96\pi^2F_\pi^2}\left(1 + \log\left(\frac{M_\pi^2}{\mu^2}\right)\right), \tag{7.12}$$

where

$$C_2^{\mathrm{r}}(\mu) = -\frac{3e}{128\pi^2M_\rho^2} \tag{7.13}$$

is the resonance saturation estimate, $\mu = M_\rho = 775.26\,\mathrm{MeV/c^2}$, $F_\pi = 92.21\,\mathrm{MeV}$ the pion decay constant, M_π the pion mass and e the elementary charge.

$$1 + 3M_\pi^2\bar{C} = 1 + 0.067 \tag{7.14}$$

Using the fit result obtained with the normalization by the kaon flux, the following value for $F_{3\pi}$ is obtained:

$$F_{3\pi,K} = (12.9 \pm 0.1(\mathrm{stat.}))\,\mathrm{GeV}^{-3} \tag{7.15}$$

Using the fit result obtained with the normalization to the radiative width of the ρ meson, the following value for $F_{3\pi}$ is obtained:

$$F_{3\pi,\rho} = (10.2 \pm 0.1(\mathrm{stat.}))\,\mathrm{GeV}^{-3} \tag{7.16}$$

The result obtained using the normalization to the radiative width of the ρ meson

is agreement with the theoretical expectation. To obtain this result, Fig. 7.12 has to be scaled by a factor of about 1.6, a factor that cannot be explained currently. Possible sources are the luminosity determination and/or the correction for acceptance. Thus the value obtained with the kaon normalization is used as the result. To take the radiative width into account a systematic uncertainty of $2.7\,\mathrm{GeV}^{-3}$ is proposed.

The low statistical error indicates the potential of the measurement once the systematic uncertainties, stemming from the absolute normalization, are understood.

Chapter 8

Conclusion and outlook

An event selection for the event signature $\pi^-\text{Ni} \to \pi^-\pi^0\text{Ni}$ from the COMPASS data record in 2009 and 2012 has been developed. The event selection has been cross-checked and the result has been released by the COMPASS collaboration to be shown on conferences.

The $\pi^-\pi^0$ invariant mass spectrum of the selected events offers the possibility to extract the chiral anomaly using a theory model proposed in [25]. The necessary steps for this analysis have been performed using the data record in 2009.

The background from $\pi^-\pi^0\pi^0$ has been estimated using weighted Monte Carlo data according to [30]. Estimated background and reconstructed data have been acceptance corrected using a Monte Carlo simulation. The invariant mass has been normalized by both the photon flux according to EPA and the beam luminosity, that has been re-estimated using the decay of beam kaons in $\pi^-\pi^0$. A preliminary value for $F_{3\pi}$ has been extracted:

$$F_{3\pi} = (12.9 \pm 0.1(\text{stat}) \pm 2.7(\text{sys}))\,\text{GeV}^{-3}. \tag{8.1}$$

This large systematic uncertainty is introduced by the absolute normalization of the invariant mass distribution that depends on the method chosen. Understanding the deviations between the two different methods should be the starting point for an improvement of the analysis.

As seen in Fig. 7.17 (b) deviations of the fit function from the data at low invariant masses is visible. This could be stemming from e.g. $\pi^-\pi^0\pi^0$ background. For an advanced $\pi^-\pi^0\pi^0$ background estimate, Monte Carlo data should be generated using the model extracted in [30]. The data should be analyzed for the $\pi^-\pi^0\pi^0$ final state and weighted that it fits with selected $\pi^-\pi^0\pi^0$ events from real data. Applying this weight the leakage in $\pi^-\pi^0$ can determined precisely. The background stemming from ω exchange has still to be estimated.

In addition a first step towards a PWA of the $\pi^-\pi^0$ final state has been taken, observing contributions from the $\rho_3(1690)$ meson that hint to a radiative coupling of that resonance. In addition a probable contribution of the $\rho(1700)$ has been observed. The contribution of the f-wave in the region of $600\,\mathrm{MeV/c^2}$ has not been yet understood and requires further investigation.

For further investigations the data recorded in 2012 should be considered, as it provides approximately five times more events. In addition a calibration for the ECAL1 is available. Using data from the ECAL1 should increase the acceptance and should lead to a better understanding and suppression of $\pi^-\pi^0\pi^0$ background. This analysis requires a carefully checked and working Monte Carlo simulation for the 2012 setup.

This issue has been tackled when analysing the 2012 data for the $\pi^-\gamma$ final state using the event selection proposed in [36] to extract the pion polarizability. The analysis has been started in [36], where deviations in the kinematic distributions between real data and Monte Carlo simulation have been observed. This effect has been studied and solved by changing the multiple scattering model. Still a false polarizability of the muon is extracted from the data. Detector efficiencies have been studied, discovering wrongly estimated efficiencies for the Monte Carlo simulation. Position dependent detector efficiencies have been extracted from real data, that should be applied to the Monte Carlo simulation.

Considering that COMGEANT and TGEANT are in perfect agreement for the 2009 hybrid setup, one should focus on the components that differ between the 2009 and 2012 setup. One of the main differences is the tracking system close to the target. In 2012 the SI04X silicon plane was broken and the SI04Y plane was not working probably. The lack of these planes has been compensated by the use of the pixel micromegas which are still in development stage. The influence of these changes are of great interest. In order to study this, a data taking period could be re-produced not using both the SI04X/Y planes as well as the pixel micromegas. The data could then be compared to Monte Carlo data reconstructed without using these detectors.

Another difference is the different position of the SAS. This leads to the effect that for higher x_γ the low energetic pions/muons cross the yoke of the SM2. This behaviour is the same in the simulation and real, but maybe some issues are introduced when it is not recognized that a track crossed the yoke or the magnetic field changes close to the yoke.

Acknowledgement

Ich bedanke mich bei meinem ehemaligen Physik-Lehrer Wolfgang Rubenbauer, der mich immens bei der Aneignung meiner Programmierkenntnisse gefördert hat. Ohne ihn wäre diese Arbeit so nicht möglich gewesen. Ebenso geht ein großes Dankeschön an meinen Mathematik-LK Lehrer Christian Eckardt, der mich mit seiner Art und Weise zu denken perfekt auf das Studium vorbereitet hat.

Natürlich geht der Dank an mein privates Umfeld. An meine Freundin Marion, die manch schlechte Launen von mir gutmütig ertragen hat und zahlreiche dumme Tippfehler in meiner Arbeit gefunden hat. Und an meine Eltern, welche ebenfalls immer an meinen Fortschritten interessiert waren, mich unterstützt haben und immer Vertrauen in mich hatten.

Last but for sure not least geht der Dank an Stefan Huber. Ohne dich wäre Vieles nicht möglich gewesen. Die vielen Stunden nach deiner Arbeitszeit, die du mit mir verbracht hast, sind mit nichts aufzuwiegen.

Appendix A

PWA fit results
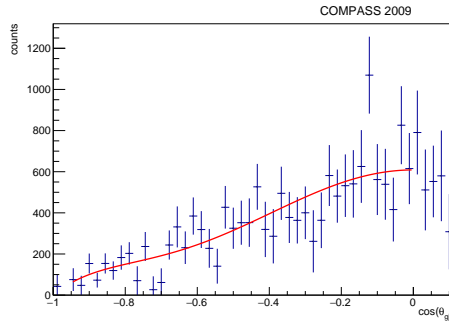
(a) $0.3 \, \text{GeV/c}^2 < m_{\pi^- \pi^0} < 0.4 \, \text{GeV/c}^2$
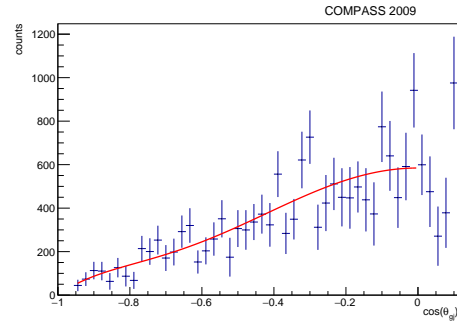
(b) $0.4 \, \text{GeV/c}^2 < m_{\pi^- \pi^0} < 0.45 \, \text{GeV/c}^2$
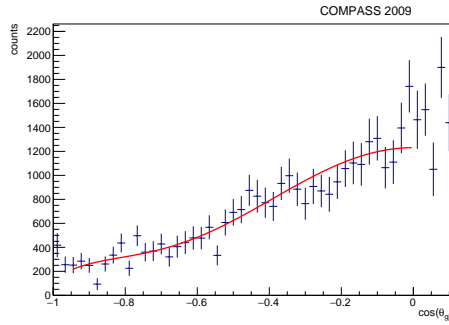
(c) $0.45 \, \text{GeV/c}^2 < m_{\pi^- \pi^0} < 0.5 \, \text{GeV/c}^2$
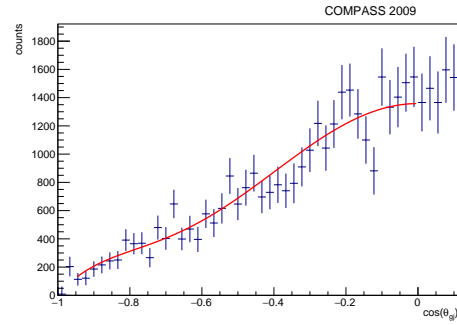
(d) $0.5 \, \text{GeV/c}^2 < m_{\pi^- \pi^0} < 0.55 \, \text{GeV/c}^2$
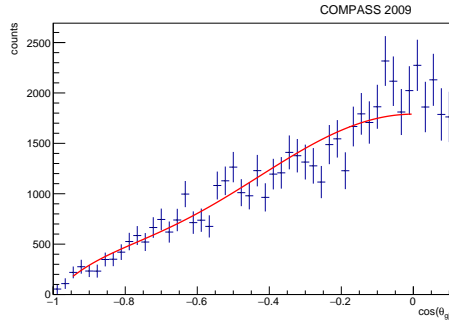
(e) $0.55 \, \text{GeV/c}^2 < m_{\pi^- \pi^0} < 0.6 \, \text{GeV/c}^2$
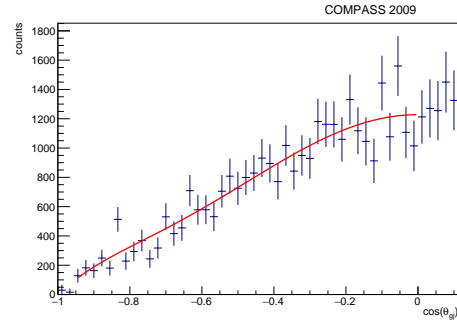
(f) $0.6 \, \text{GeV/c}^2 < m_{\pi^- \pi^0} < 0.625 \, \text{GeV/c}^2$
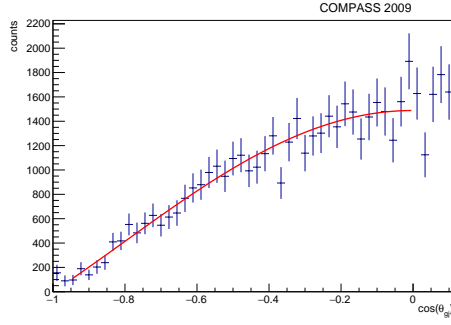
(g) $0.625\,\mathrm{GeV/c^2} < m_{\pi^-\pi^0} < 0.65\,\mathrm{GeV/c^2}$
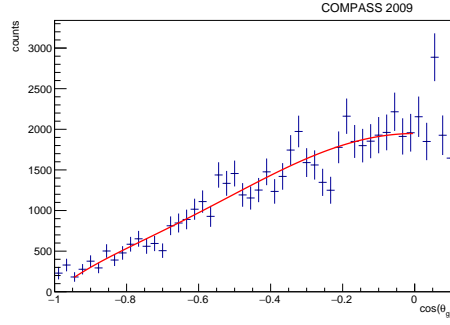
(h) $0.65\,\mathrm{GeV/c^2} < m_{\pi^-\pi^0} < 0.675\,\mathrm{GeV/c^2}$
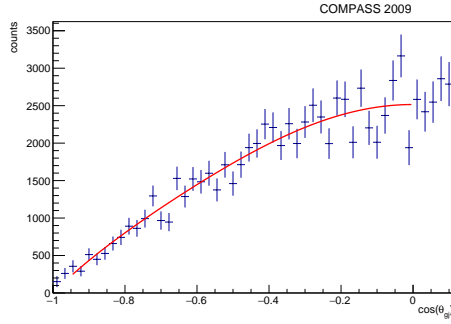
(i) $0.675\,\mathrm{GeV/c^2} < m_{\pi^-\pi^0} < 0.7\,\mathrm{GeV/c^2}$
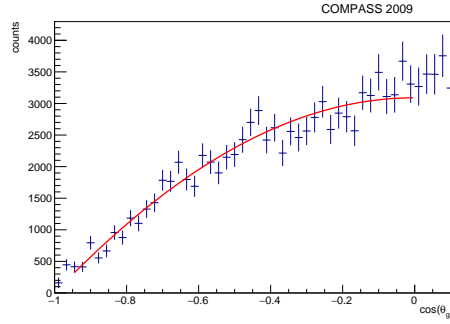
(j) $0.7\,\mathrm{GeV/c^2} < m_{\pi^-\pi^0} < 0.725\,\mathrm{GeV/c^2}$
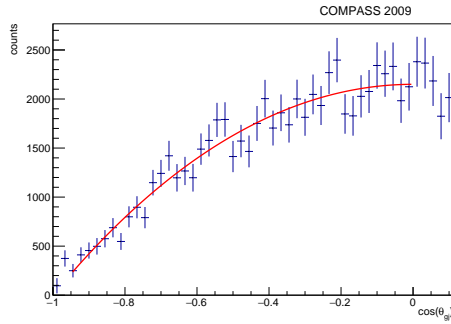
(k) $0.725\,\mathrm{GeV/c^2} < m_{\pi^-\pi^0} < 0.74\,\mathrm{GeV/c^2}$

(l) $0.74\,\mathrm{GeV/c^2} < m_{\pi^-\pi^0} < 0.75\,\mathrm{GeV/c^2}$

(m) $0.75\,\mathrm{GeV/c^2} < m_{\pi^-\pi^0} < 0.76\,\mathrm{GeV/c^2}$ (n) $0.76\,\mathrm{GeV/c^2} < m_{\pi^-\pi^0} < 0.77\,\mathrm{GeV/c^2}$

(o) $0.77\,\mathrm{GeV/c^2} < m_{\pi^-\pi^0} < 0.78\,\mathrm{GeV/c^2}$ (p) $0.78\,\mathrm{GeV/c^2} < m_{\pi^-\pi^0} < 0.79\,\mathrm{GeV/c^2}$

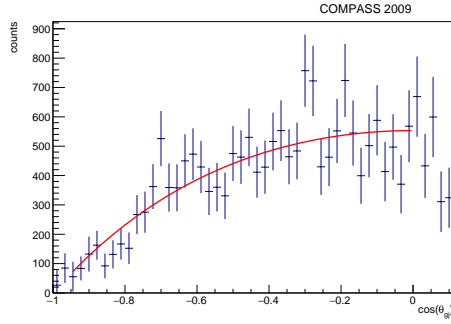(q) $0.79\,\mathrm{GeV/c^2} < m_{\pi^-\pi^0} < 0.8\,\mathrm{GeV/c^2}$ (r) $0.8\,\mathrm{GeV/c^2} < m_{\pi^-\pi^0} < 0.825\,\mathrm{GeV/c^2}$
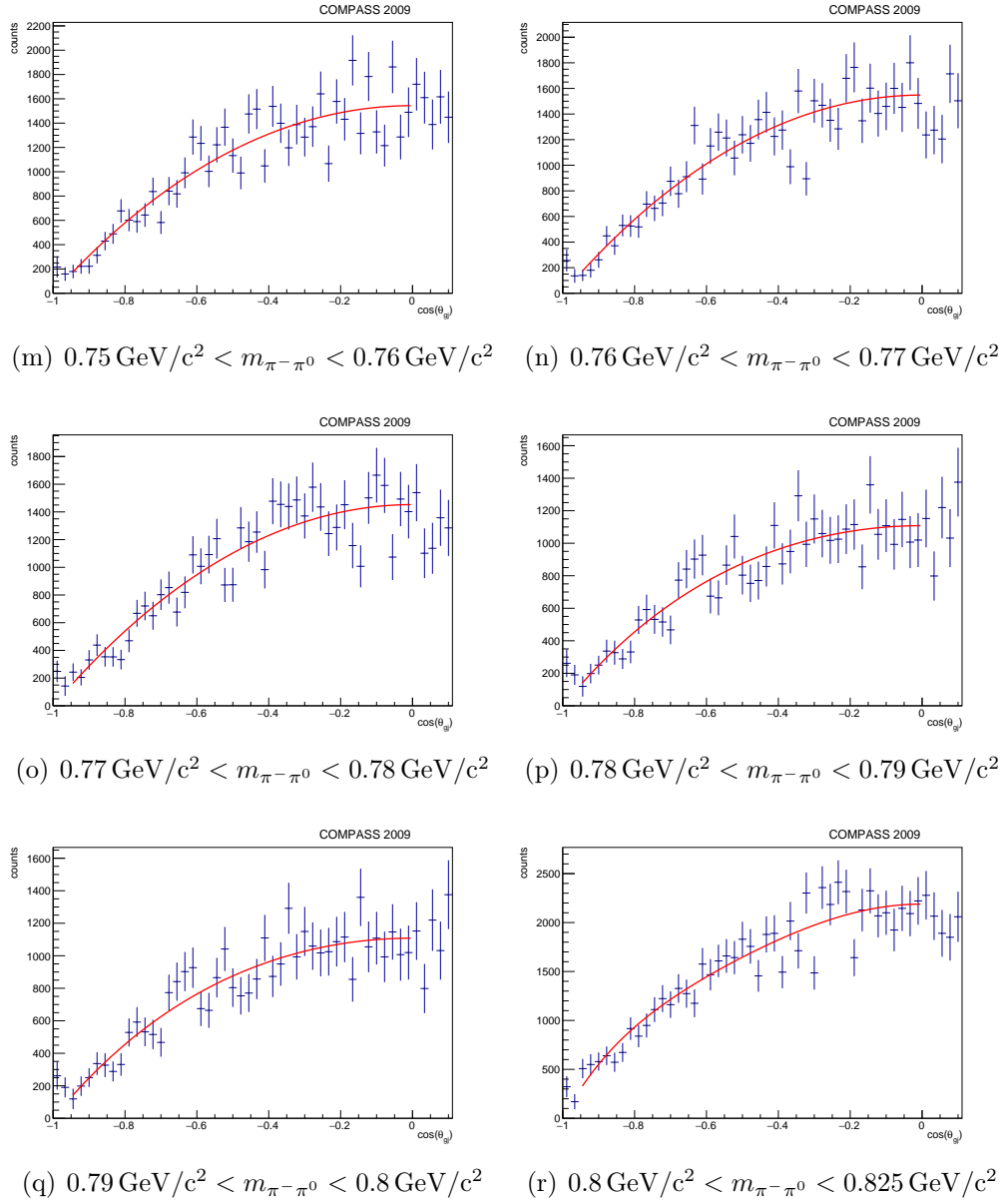
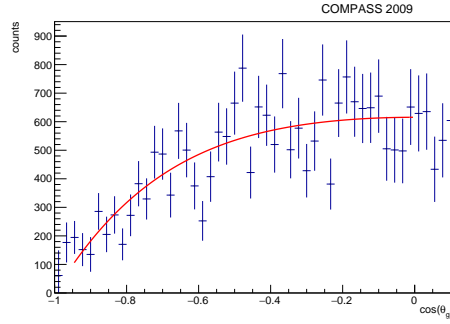Figure A.1: Fit of the partial waves to the angular distribution in the rest frame.
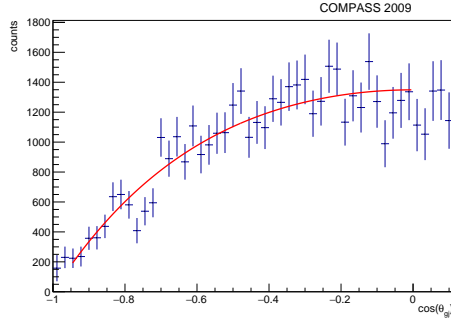
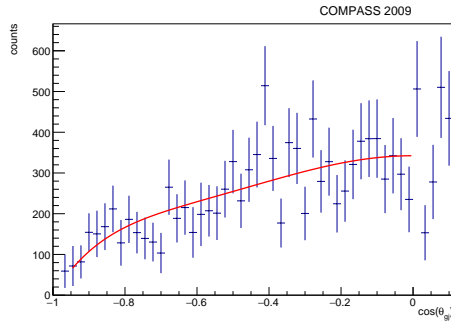(a) $0.825\,\mathrm{GeV/c^2} < m_{\pi^-\pi^0} < 0.85\,\mathrm{GeV/c^2}$ (b) $0.85\,\mathrm{GeV/c^2} < m_{\pi^-\pi^0} < 0.875\,\mathrm{GeV/c^2}$
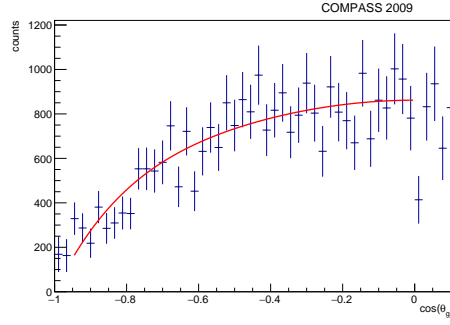
(c) $0.875\,\mathrm{GeV/c^2} < m_{\pi^-\pi^0} < 0.9\,\mathrm{GeV/c^2}$ (d) $0.9\,\mathrm{GeV/c^2} < m_{\pi^-\pi^0} < 0.95\,\mathrm{GeV/c^2}$

(e) $0.95\,\mathrm{GeV/c^2} < m_{\pi^-\pi^0} < 1.0\,\mathrm{GeV/c^2}$ (f) $1.0\,\mathrm{GeV/c^2} < m_{\pi^-\pi^0} < 1.1\,\mathrm{GeV/c^2}$
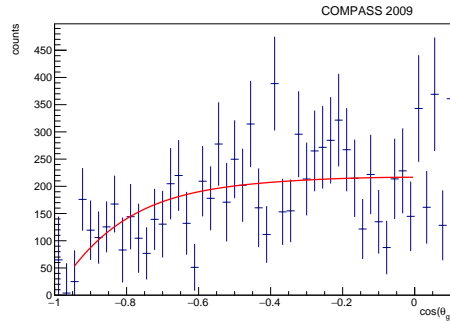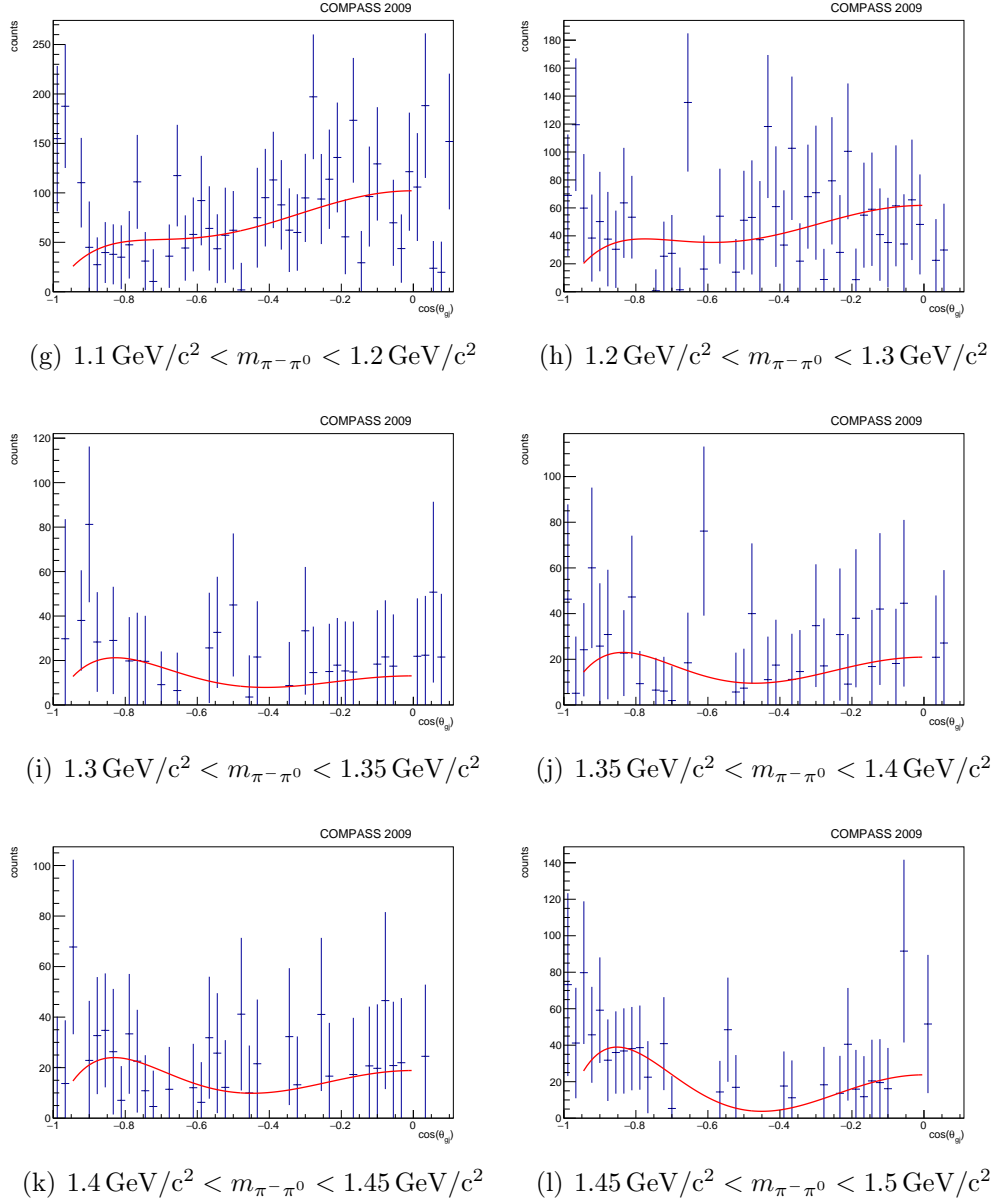
Figure A.1: Fit of the partial waves to the angular distribution in the rest frame.

(g) $1.1\,\mathrm{GeV/c^2} < m_{\pi^-\pi^0} < 1.2\,\mathrm{GeV/c^2}$

(h) $1.2\,\mathrm{GeV/c^2} < m_{\pi^-\pi^0} < 1.3\,\mathrm{GeV/c^2}$

(i) $1.3\,\mathrm{GeV/c^2} < m_{\pi^-\pi^0} < 1.35\,\mathrm{GeV/c^2}$

(j) $1.35\,\mathrm{GeV/c^2} < m_{\pi^-\pi^0} < 1.4\,\mathrm{GeV/c^2}$

(k) $1.4\,\mathrm{GeV/c^2} < m_{\pi^-\pi^0} < 1.45\,\mathrm{GeV/c^2}$

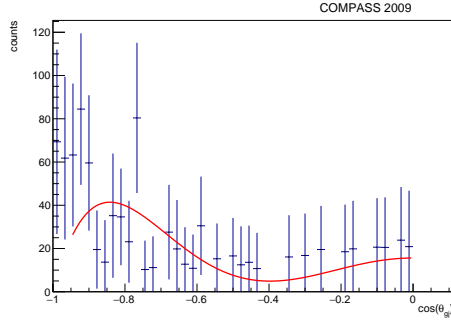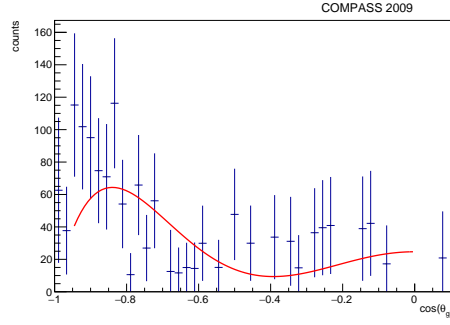(l) $1.45\,\mathrm{GeV/c^2} < m_{\pi^-\pi^0} < 1.5\,\mathrm{GeV/c^2}$

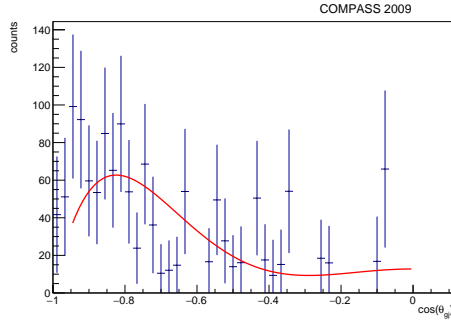Figure A.1: Fit of the partial waves to the angular distribution in the rest frame.

(m) $1.5\,\mathrm{GeV/c^2} < m_{\pi^-\pi^0} < 1.55\,\mathrm{GeV/c^2}$ (n) $1.55\,\mathrm{GeV/c^2} < m_{\pi^-\pi^0} < 1.6\,\mathrm{GeV/c^2}$

(o) $1.6\,\mathrm{GeV/c^2} < m_{\pi^-\pi^0} < 1.65\,\mathrm{GeV/c^2}$ (p) $1.65\,\mathrm{GeV/c^2} < m_{\pi^-\pi^0} < 1.7\,\mathrm{GeV/c^2}$

(q) $1.7\,\mathrm{GeV/c^2} < m_{\pi^-\pi^0} < 1.75\,\mathrm{GeV/c^2}$ (r) $1.75\,\mathrm{GeV/c^2} < m_{\pi^-\pi^0} < 1.8\,\mathrm{GeV/c^2}$
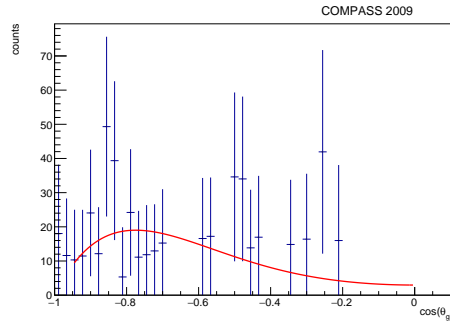
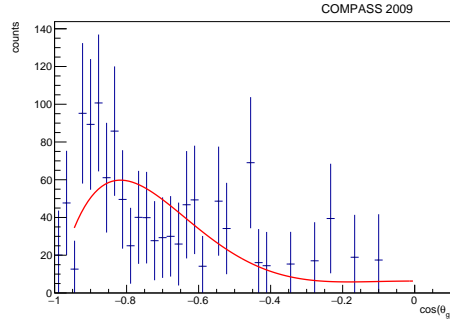Figure A.1: Fit of the partial waves to the angular distribution in the rest frame.

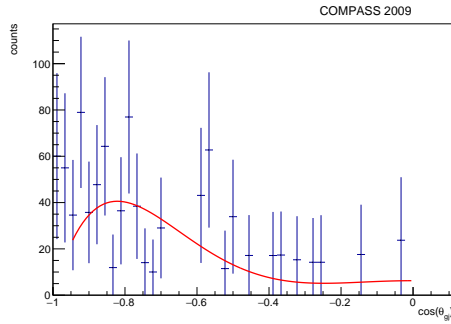(s) $1.8\,\mathrm{GeV/c^2} < m_{\pi^-\pi^0} < 1.9\,\mathrm{GeV/c^2}$ (t) $1.9\,\mathrm{GeV/c^2} < m_{\pi^-\pi^0} < 2.0\,\mathrm{GeV/c^2}$
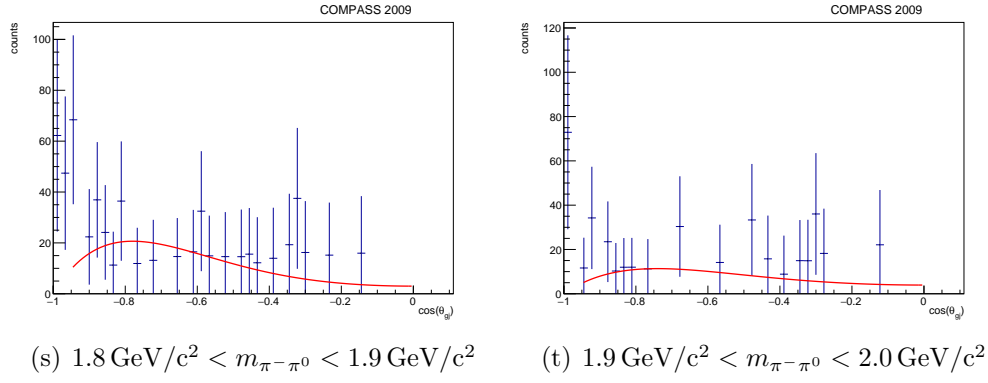
Figure A.1: Fit of the partial waves to the angular distribution in the rest frame.

Bibliography

[1] A. Pich. »Chiral Pertubation theory«. In: (1995). arXiv: `hep-ph/9502366`.

[2] *Official COMPASS website.* `http://wwwcompass.cern.ch/`. Accessed: 2017-06-04.

[3] CAST Collaboration. »New CAST limit on the axion-photon interaction«. In: (2017). Nature Physics 13: `584-590`.

[4] *Official PrimEx website at Jefferson Lab.* `https://www.jlab.org/primex/`. Accessed: 2017-06-12.

[5] V.L. Kashevarov L.V. Filkov. »Pion polarizabilities«. In: (2006). arXiv: `hep-ph/0610102v2`.

[6] S. Huber et al. (COMPASS collaboration). »Measurement of the Pion Polarizability at COMPASS«. In: (2014). arXiv: `1401.4760v2`.

[7] M. Sainio J. Gasser M. Ivanov. »Revisiting $\gamma\gamma \to \pi^+\pi^-$ at low energies«. In: (2006). Nucl. Phys. `B745:84-108`.

[8] Y.M. Antipov et al. In: (1987). Phys. Rev. `D36,21`.

[9] L. Ametller et al. »Electromagnetic corrections to $\gamma\pi^+ \to \pi^0\pi^+$«. In: (2001). arXiv: `hep-ph/0107127`.

[10] I. Giller et al. »A new determination of $\gamma\pi \to \pi\pi$ anomalous amplitude via the $\pi^-e^- \to \pi^-e^-\pi^0$ data«. In: (2005). arXiv: `hep-ph/0503207v2`.

[11] B. Povh. *Teilchen und Kerne.* ISBN: 978-3-642-37822-5.

[12] F. Hass. »Two dimensional Partial-Wave Analysis for Exclusive $190\,\text{GeV}$ π^-p Scattering into the $\pi^-\pi^-\pi^+$ Finale State at COMPASS (CERN)«. PhD thesis. TU München, 2013.

[13] H. Primakoff. »Photo-production of neutral mesons in nuclear electric fields and the mean life of the neutral meson«. In: (1951). Phys. Rev. `81:899-899`.

[14] J. D. Jackson and K. Müller. *Klassische Elektrodynamik.* de Gruyter, 2002.

[15] T. Fliessbach. *Elektrodynamik, Lehrbuch zur Theoretischen Physik II.* Springer Spektrum, 2012.

[16] C. Patrignani et al. (Particle Data Group). *Particle Physics Booklet*. Chin. Phys. C., 2016.

[17] V. A. Petrunking. »Scattering of low-energy photons on a zero-spin particle«. In: (1964). Nuclear Physics: `55:197-206`.

[18] D. Drechsel and L. V. Filkov. »Compton scattering on the pion and radiative pion photoproduction from the proton«. In: (1994). Z. Phys: `A349:177-184`.

[19] A. S. Galperin and Guenakh Mitselmakher. »Calculation of Ultrarelativistic Pion Bremsstrahlung Corss-section on Nuclei With the Allowance for Pion Polarization«. In: (1980).

[20] C. Adolph et al. »Measurement of Charged-Pion Polarizability«. In: (2015). Physical Review Letters 114: `062002(2015)`.

[21] M. R. Pennington. »What we can learn by measuring $\gamma\gamma \rightarrow \pi\pi$ at DAPHNE«. In: (1995), pp. 531–558.

[22] T. A. Aibergenov et al. »Radiative Photoproduction of Pions and Pion Compton Scattering«. In: (1986). Czech. J. Phys. `B36:948-951`.

[23] D. Drechsel. »Pion Polarizability: A Cornerstone of Hadronic Physics«. In: (2013).

[24] E. Witten. »Global aspects of current algebra«. In: (). Nuc. Phys. B: `223, 422(1983)`.

[25] D. Sakkas M. Hoferichter B. Kubis. »Extracting the chiral anomaly from $\gamma\pi \rightarrow \pi\pi$«. In: (2012). Phys. Rev. `D86(2012)116009`.

[26] P. Abbon et al. »The COMPASS Experiment at CERN«. In: (2007). Nucl. Instrum. Methods Phys. Res. `A,577:455-518`.

[27] K. Bicker et al. »Cryogenic Silicon Detectors for the COMPASS Experiment at CERN«. In: *Nuclear Physics B - Proceedings Supplements* 215.1 (2011), pp. 310 –312.

[28] B. Ketzer et al. »GEM detectors for COMPASS«. In: (2001). Nuclear Science IEEE Transactions on: `vol.49,pp.2403-2410,2002,ISSN0018-9499.`.

[29] D. Thers et al. »Micromegas as a large microstrip detector for the COMPASS experiment«. In: *Nuclear Instruments and Methods in Physics Research Section A: Accelerators, Spectrometers, Detectors and Associated Equipment* 469 (2001), pp. 133–146.

[30] M. Krämer. »Evaluation and optimization of a digital calorimetric trigger and analysis of pion-photon-interactions in $\pi Ni \rightarrow \pi^- \pi^0 \pi^0 Ni$ Reactions at COMPASS at CERN«. PhD thesis. TU München, 2016.

[31] Jan Friedrich and Markus Krämer. »Reconstruction of the pion beam energy from beam optics«. In: (2012).

[32] Ph. Abbon et al. »The COMPASS Setup for Physics with Hadron Beams«. In: (2014). eprint: `1410.1797`.

[33] Stefanie Grabmüller. »Cryogenic Silicon Detectors and Analysis of Primakoff Contribution to the Reaction $\pi^- Pb \to \pi^- \pi^+ \pi^- Pb$ at COMPASS«. PhD thesis. TU München, 2011.

[34] B. Gobb. *CORAL website.* `https://coral.web.cern.ch/coral/`. Accessed: 2017-06-04.

[35] S. Gerassimov. *Phast, physics analysis tools for compass.* `http://ges.home.cern.ch/ges/phast/index.html`. Accessed: 2017-06-05.

[36] Stefan Huber. »Upgrade of the COMPASS calorimetric trigger and determination of the charged pion polarizability«. PhD thesis. TU München, 2017.

[37] L. Urbán. »Multiple scattering model in GEANT4«. In: (2002). CERN Report: `CERN-OPEN-2002-070`.

[38] V. N. Ivanchenko. »Geant4 models for simulation of multiple scattering«. In: (2010).

[39] T. Nagel. »Measurement of Charged Pion Polarizability at COMPASS«. PhD thesis. TU München, 2012.

[40] Jan Friedrich. »CEDAR performance 2009«. In: (2009). URL: `http://wwwcompass.cern.ch/compass/notes/2010-15/2010-15.pdf`.

[41] J. Friedrich S.-U. Chung. »Covariant Helicity-Coupling Amplitudes: A New Formulation«. In: (2007). arXiv: `0711.3143`.

[42] B. Kubis M. Hoferichter. private communication.

[43] L. Capraro et al. »The ρ radiative decay width: A measurement at $200\,\mathrm{GeV}$«. In: (1987), pp. 959–680.